UNIVERSITÉ DE SHERBROOKE
Faculté de génie
Département de génie mécanique

Caractérisation d'échaffaudages explantés en β-TCP après résorption in-vivo en utilisant des techniques d'analyse d'images raffinées corrélées avec de la micro tomodensitométrie à rayons-X

Accurate characterization of in vivo bone deposition and β-TCP scaffold resorption using X-ray micro-computed tomography and image processing

Thèse de doctorat
Specialité : génie mécanique

Ahmed SWEEDY

Jury: Gamal BAROUD (directeur)
François GITZHOFER (rapporteur)
Marc BOHNER
Stephan BECKER
Peter JARZEM

Sherbrooke (Québec) Canada Septembre 2016

To my dear parents,
The reason of what I become today.

To my sons, Omar and Seif,
The source of joy and happiness in my life.

To my dear wife,
My home, my sanctuary and my heaven.

RÉSUMÉ

L'utilisation de substituts osseux synthétiques est de plus en plus courante dans les procédés de réparation osseuse. Les biomatériaux de phosphate de calcium (CaP) sont les substituts dont la composition chimique se rapproche le plus de celle des os. Outre leur composition chimique, les propriétés géométriques des substituts osseux et, partant, leur macro et microporosité, ont une incidence sur leur efficacité et leur performance in vivo. Un grand nombre d'études se sont penchées sur le rôle des macro et microstructures des substituts dans le processus de guérison des os. Cependant, le rôle que la structure des substituts joue dans le processus de guérison reste à démontrer et est encore nébuleux en raison, entre autres, de la quasi inexistence de méthodes de caractérisation précises des phases des biopsies d'explants.

La présente thèse comportait par conséquent deux objectifs généraux. Le premier consistait à élaborer, à appliquer et à valider des méthodes novatrices de traitement de l'image utilisant des ensembles de données de microtomographie par rayons X après implantation afin de réaliser avec précision la caractérisation des phases des biopsies d'explants de substituts osseux de modèles in vivo. Une importante difficulté de l'analyse des ensembles de données de microtomographie par rayons X après implantation provient du fait que les résidus osseux et céramiques des images microtomographiques présentent une densité similaire ; il devient par conséquent ardu de différencier les résidus céramiques du tissu osseux dans le matériel prélevé par biopsie. Le second objectif, tel que détaillé ci-dessous, concerne une méthode pour analyser avec précision le dépôt osseux microscopique dans les parois des substituts céramiques.

Ainsi, le premier objectif impliquait la combinaison d'algorithmes de traitement d'images pour procéder à une étude précise des phases relevées dans les biopsies d'explants, et ainsi mieux comprendre le lien qui existe entre le processus de guérison et la structure du substitut. Plus précisément, l'alignement géométrique en 3D du substitut avant implantation sur les résidus du substitut a fourni des données sur la densité des particules osseuses par rapport à celle des résidus céramiques ; cela a donc permis de différencier avec encore plus de précision les phases relevées de la biopsie. Les résultats algorithmiques ont été entièrement validés au moyen de la théorie des matrices similaires et de la comparaison des résultats algorithmiques de cinq images choisies au hasard comprenant au total 556 800 pixels avec ceux obtenus manuellement par un scientifique expert en traitement de l'image. La validation a fait ressortir une concordance à 94 pour cent. Les clichés histologiques ont en outre confirmé les résultats de validation. Le nouvel algorithme en 3D permet donc d'analyser globalement et localement des effets macroscopiques comme la néoformation osseuse et la résorption céramique du processus de guérison. Globalement, ces effets sont analysés pour tout le substitut ; localement, ces effets peuvent être analysés pour chacune des distributions de pores du substitut. Cette approche novatrice aide ainsi à intégrer la conception structurelle du substitut osseux au processus de guérison. Les méthodes et les résultats relatifs à cet objectif sont expliqués plus en détail au chapitre 3.

Le second objectif de la présente thèse impliquait l'élaboration d'une nouvelle catégorie d'algorithmes servant à analyser avec précision des effets microscopiques comme la néoformation osseuse dans les pores microscopiques du substitut céramique, permettant ainsi l'étude des effets

microscopiques du processus de guérison. Plus particulièrement, les structures matérielles observées dans les images à haute définition en 2 D de l'histologie et des techniques MEB étaient alignées géométriquement sur la structure en 3D de l'ensemble des données de microtomographie par rayons X du même substitut avant et après implantation. Par conséquent, les ensembles de données de microtomographie par rayons X en 3D avant implantation ont été utilisés pour définir la référence géométrique de la céramique qui se résorbe, ce qui par conséquent a permis d'effectuer une analyse précise des phases matérielles des clichés à haute résolution en 2D des coupes d'évaluation histologiques. Plus précisément, une fois que les images produites au moyen des techniques d'imagerie multimodale ont été combinées et alignées, l'information couleur provenant de l'histologie et la valeur de gris obtenue au moyen des images MEB ont été utilisées pour analyser les images histologiques ; celles-ci possédaient une résolution moyenne de 1,2 microns, ce qui a rendu possible l'étude des effets microscopiques à l'aide de clichés histologiques en 2D. Les méthodes et les résultats relatifs au second objectif sont au chapitre 4. Toujours au regard du second objectif, les nouveaux algorithmes ont servi à l'analyse des effets microscopiques et macroscopiques pour deux groupes de substituts β-TCP dont la taille des pores s'accroissait progressivement (diamètre de pore moyen = 510 et 1220 microns), implantés dans un modèle ovin pendant 6 semaines. Trois échantillons prélevés dans chaque groupe ont servi à étudier la néoformation osseuse et la résorption céramique. Des taux très élevés de néoformation osseuse et de résorption céramique ont été mesurés chez le groupe de substituts dont la taille des pores était la plus petite. Outre le taux plus élevé de néoformation osseuse, le groupe dont la taille des pores était plus petite présentait spécifiquement un important effet de surface ; en effet, le ratio de conversion de la surface de céramique résorbée en tissu osseux était beaucoup plus élevé que chez les deux autres groupes. Des études plus approfondies devront être menées afin d'analyser les effets de surface et les interactions entre le substitut osseux et le processus de guérison osseuse.

Les méthodes et les algorithmes connexes de la présente thèse ont fourni un moyen novateur et original d'évaluer les effets microscopiques et macroscopiques du processus de guérison. Tout comme d'autres méthodes, les nouvelles méthodes mises au point sont limitées. Celles-ci, exigeantes en termes de calculs, ont nécessité la présence d'un nombre suffisant d'éléments géométriques dans le substitut explanté afin d'aligner ces éléments sur ceux de la structure avant implantation.

Mots-clés : analyze multimodal, Dépôt osseux, enregistrement d'image, échafaudage résorption, greffe osseuse, microtomographie, phosphate tricalcique, segmentation d'image

ABSTRACT

Synthetic bone substitutes are being increasingly used in bone repair procedures. Calcium-phosphate (CaP) substitute biomaterials have the closest chemical composition to bone. Besides the chemical composition, the geometrical properties and hence the macro and micro-porosity of the bone substitutes affect their *in vivo* effectiveness and performance. A large number of studies have investigated the role of the substitute's macro- and micro-structure in the bone healing process. The role that the substitute's structure plays in the healing process, however, remains debatable and unclear because of, among other reasons, the lack of accurate characterization methods of the phases in the explanted biopsies.

This thesis accordingly had two overall objectives. The first was to develop, implement and validate novel image-processing methods for using the post-implantation mCT datasets to help accurately characterize the phases in bone substitute biopsies explanted from *in vivo* models. One important difficulty in analyzing the post-implantation mCT datasets is that bone and ceramic remnants in the mCT images appear to have similar density; differentiating between ceramic remnants and bone tissue in the biopsies therefore becomes difficult. The second objective, as detailed below, related to a method to accurately analyze the microscopic bone deposition into the bone substitute's ceramic wall.

Accordingly, undertaking the first objective involved developing image-based algorithms to accurately study the phases found in the explanted biopsies and thus better understand the relationship of the healing process and the substitute's structure. Specifically, the 3D geometric alignment of the pre-implantation substitute with the substitute's remnants provided access to data on the density characteristics of the bone versus the ceramic remnants; this accordingly allowed a more accurate differentiation of the phases found in the biopsy. The algorithmic results were thoroughly validated, using the similarity matrix theory and by comparing the algorithmic results of five randomly selected images — comprising a total of 556,800 pixels — with those obtained by a skilled image-processing scientist. The validation showed a 94-percent agreement. Histology photographs further confirmed the validation results. Accordingly, the new 3D algorithm helps to globally and locally analyze macroscopic effects such as bone deposition and ceramic resorption of the healing process. Globally, these effects are analyzed for the entire substitute, and locally, these effects can be studied for each pore of the substitute. The novel approach thus helps relate the bone substitute's structural design to the healing process. The methods and the results related to this objective are detailed in Chapter 3.

The second objective of the present thesis entailed developing a new class of algorithms to accurately analyze the microscopic effects such as the bone deposition in the microscopic porosity of the ceramic substitute, thereby allowing the study of microscopic effects of the healing process. Specifically, the material structures seen in the high-resolution 2D images of the histology and SEM techniques were geometrically aligned with the 3D structure in the mCT dataset of the same substitute before and after implantation. Accordingly, the 3D pre-implantation mCT datasets were used to define the geometric reference of the resorbing ceramic, and therefore allowed an accurate analysis to be made of the material phases in the high-resolution 2D pho-

tographs of the histology evaluation cuts. Specifically, once the images from the multimodal imaging techniques were combined and aligned, the color information from histology and the grey value information from SEM images were used to analyze the histology images; the latter had an average resolution of 1.2 microns and this made studying the microscopic effects using the 2D histology photographs possible. The methods and the results related to the second objective are in Chapter 4. Still in line with the second objective, the new algorithms were used to analyze the microscopic and macroscopic effects of two β-TCP substitute groups of incrementally increasing pore size (mean pore diameter = 510 and 1220 microns), implanted in an ovine model for 6 weeks. Three samples were selected per group to investigate the microscopic and macroscopic bone deposition and ceramic resorption. Significantly higher bone deposition and ceramic resorption were measured in the substitute group with the smaller pore size. In addition to the higher micro-bone deposition, the smaller pore-size group specifically featured an important surface effect; namely, the conversion ratio of resorbed surface ceramic into bone tissue was significantly higher compared to the two other groups. Further studies are still required to investigate the surface effects and the related interactions between the bone-substitute design and the bone-healing process.

The present thesis' methods and related algorithms provided novel and original means to evaluate microscopic and macroscopic effects of the healing process. Like other methods, the newly developed ones have limitations. The methods are computationally demanding, and required that a sufficient number of geometric features be present in the explanted substitute so as to align these features with those of the pre-implantation structure.

Keywords: Bone deposition, bone substitutes, image segmentation, image registration, micro-computed tomography, multimodal analysis, scaffold resorption, tricalcium phosphate

ACKNOWLEDGEMENTS

First of all, I would like to express my sincere gratitude and appreciation to Professor Gamal BAROUD, my Ph.D. supervising director, for his unconditional support throughout my Ph.D. studies and for his patience, motivation, enthusiasm, and his immense knowledge which he so generously made available to me. His guidance and openness were a guiding light throughout all of my research and article and thesis writing. I feel so fortunate to have had him as my Supervising Director. Not only was he a great supervisor, he was an inspiring mentor who enlightened me for my long-term career.

Beside my supervisor, I am deeply thankful and grateful to Professor Marc BOHNER for the many fruitful discussions we have had together and from which I benefited greatly because of his great knowledge in the field of bone augmentation and repair. It is an honor to have had the opportunity to work with him. He was available to discuss and provide me with very valuable and critical comments that helped bring me to a higher scientific level.

I very much want to thank Professor François GITZHOFER for his availability to discuss and his very useful comments. He was unconditionally supportive and encouraging when it was mostly needed. I appreciate him acting as reporter and jury member for my Ph.D. thesis. I would also like to thank Professor Stephan BECKER and Professor Peter JARZEM, who are pioneers in the field of bone substitute research, for accepting to be members of my Ph.D. Evaluation Committee. It is a great honor for me to have them act in this role.

I would like to thank the Natural Sciences and Engineering Research Council of Canada (NSERC) and the Canada Research Chair Program (CRC) for supporting my Ph.D. research. I am particularly very grateful to the Robert Mathys Foundation (RMS) for the support received for my thesis and for continuously providing me with the unique experimental data. I am also grateful for Professor Harry van LENTHE for helping provide essential datasets for my Ph.D. research. My gratitude extends to Brian DRISCOLL, Denis IMBEAULT and Jason GAUTHIER for providing technical support for my research. Many thanks also to all the administrative members of the Mechanical Engineering Department's office, especially Sylvie PERRON. I thank my former colleague in the Biomechanics Laboratory, Dr. Juan ZHANG, for the discussions and encouragement.

Last but not least, I want to express my heartfelt gratitude to my family for having lovingly and unconditionally supported me throughout my study years. I would like to thank my parents for the unconditional love, support and encouragement throughout my entire life. A special thank you goes to my in-laws for their support and encouragement. Thank you to my loving wife for supporting and encouraging me unconditionally throughout the length of my Ph.D. studies and to my sons Omar and Seifeldin for their patience.

TABLE OF CONTENTS

LIST OF FIGURES

LIST OF TABLES

LIST OF ACRONYMS

Acronym	Definition
BCP	Biphasic calcium phosphate
BMO	Bone marrow-derived osteoprogenitor cells
BMPs	Bone morphogenetic proteins
BMSC	Bone marrow stromal cells
BV	Bone volume
CaP	Calcium phosphate
DSC	Dice similarity coefficient
EED	Edge enhancing diffusion
FDT	Fuzzy distance transform
HA	Hydroxyapatite
mCT	Microcomputed tomography
MSC	mesenchymal stem cells
NBV	New bone volume fraction
PMMA	Polymethyl methacrylate
POF	Pore occupation fraction
SBS	Synthetic bone substitutes
SEM	Scanning electron microscopy
SIFT	scale invariant feature transform
SNR	Signal to noise ratio
SURF	speed-up robust features
SSD	Sum of squared differences
TBH	Toluidine blue stained histology
TCP	Tricalcium phosphate
THB	Threshold of bone
THC	Threshold of ceramic remnants
TV	Total volume

CHAPTER 1

INTRODUCTION

1.1 Background and significance

In non-critical size defect, the healing process takes place in three consecutive phases; phase of inflammation, phase of osteogenic repair tissue and phase of remodelling [Nather, 2005]. Despite the three phases are common in bone tissue repair, critical size defect requires orthopaedic intervention, such as bone grafting, to assist the bone to complete the healing process [Spicer *et al.*, 2012]. Such defects are commonly caused by trauma, degradation or diseases usually associated with aging. Since the Dutch surgeon Job van Meekren had made the first documented attempt at tissue engineering by filling bony defect in a soldier's cranium with a piece of dog skull in 1670 [Nather, 2005], skeletal defects have been replaced by bone grafts. Bone grafting became an accepted technique since the early 20th century. Despite autologous bone grafting remains the gold standard in bone transplantation, they are associated with long-term side effects including donor site numbness and pain [Schwartz *et al.*, 2009; Silber *et al.*, 2003]. This resulted in decreased ability to work in 10% of the patients, difficulty to walk in 16%, recreational activities limitation in 18% and 19% of these patients suffered pain that affected their ability to perform household chores [Schwartz *et al.*, 2009]. Another similar technique to autograft is allograft (graft harvested from another donor or subject). While allografting eliminates the problems associated with harvest site, it presents other complications associated with transplantation between different persons including increased risk of infection by disease transmission [Nather, 2005; Yaszemski *et al.*, 1996] and immunological reaction that may require the use of immunosuppressant drugs [LeGeros, 2008; Lemons *et al.*, 1988]. Therefore, the need of synthetic bone substitutes (SBS) emerged as a replacement of autografs and allografts.

By the development of better understanding of the immune system during the 1960s and 1970s, the first generation of synthetic materials for use inside the human body was developed [Hench and Polak, 2002; Nather, 2005]. In terms of bone substitutes, Hench and his colleagues discovered the bioactive glass by the end of 1960s and it was followed by two other generations reaching the third-generation bioactive glasses, composites, hybrid materials and macroporous foams that are designed to activate genes that stimulate regeneration of living tissues [Hench, 2006; Hench and Polak, 2002; Will *et al.*, 2011]. The calcium-phosphate (CaP) biomaterial, because of its similar chemical composition to bone, was also considered for treating bone defects as early as 1920, yet the CaP related research surged in the 1970s and CaP materials were used in dental and orthopedic applications [Habraken *et al.*, 2016]. CaP materials showed some attractive features as a bone substitute material including biocompatibility, bioactivity and osteoconductivity, in addition to resorbability in the case of β-tricalcium phosphate (β-TCP). Since then, many studies have been conducted to optimize the bone substitutes in terms of material composition and geometry to achieve the optimum scaffold design that promotes bone deposition

and scaffold resorption in an integrated pattern that allows the bone substitute to be completely replaced by bone while supports the load bearing functionality of the skeletal structure.

Due to ethical issues, the answer to the question of otimum scaffold design usually involves conducting *in vivo* experiments to investigate the influence of the substitutes design on their performance and the biological processes taking place inside the defect site. The importance of *in vivo* characterization of tissue regeneration in bioscaffolds arises from the importance of better understanding of the bone healing process [Gauthier *et al.*, 2005; Papadimitropoulos *et al.*, 2007; van Lenthe *et al.*, 2007; von Doernberg *et al.*, 2006]. Failure to achieve enough tissue regeneration for functional support leads to mechanical failure though scaffold properties are adequate for temporary load bearing [Feng *et al.*, 2012; Hollister *et al.*, 2005].

In vivo studies are always associated with large image data analysis to characterize different phases in the explanted samples or biopsies. Such data could be in the form of 2D images (i.e. histology and SEM) or 3D images (i.e. micro-computed tomography). The accurate evaluation of these data is a necessary step in the process of data analysis, leading to accurate conclusions and better understanding of the biological processes in bone repair using SBS.

1.2 Motivation

With annual estimation of two million patients are subjected to the bone grafting procedure for repairing critical size bone defects [Bohner, 2010], bone is ranked as the second transplanted and replaced material in human body [Zorzi, 2012]. Hence, scientific attention to bone grafts development arises to find the optimum scaffold for assisting the healing process of defects that are commonly caused by trauma, degradation or diseases which are usually associated with aging [Nather, 2005; Zorzi, 2012]. Bone graft substitutes market is not only one of the high demanding markets with over one billion dollars revenue but it has also one of the high annual market growth rate of about 15% [Bohner, 2010]. In addition to the demanding market, the socioeconomic impact of the critical size bone defects induces a high demand for research and development of better understanding of the properties of synthetic bone substitutes and their influence on bone regeneration as well as the healing process being exerted in order to find the optimum scaffold material and micro-structural design. The optimum bone scaffold is the scaffold which is resorbed completely and synchronously replaced by bone in a pattern that allows the scaffold of being replaced without affecting its mechanical support functions [Carlier *et al.*, 2011].

Next to the material composition, the geometrical design and structure of the bone substitutes was found to influence the bone deposition and the substitute resorption [Gauthier *et al.*, 2005;

Papadimitropoulos *et al.*, 2007; van Lenthe *et al.*, 2007; von Doernberg *et al.*, 2006]. For instance, there is an agreement in literature on introducing macro-porosity (pore size > 50 microns) to bone substitutes to help cellular migration and vascularization [LeGeros, 2008; Lemons *et al.*, 1988]. However, the optimum pore size that yields the best performance of bone substitutes is still under debate [von Doernberg *et al.*, 2006].

Furthermore, recent findings showed that introducing microporosity (pore size < 50 microns) to non-resorbable hydroxyapatite (HA) bone substitutes improves their performance and results in better osseointegration [Polak *et al.*, 2011; Scaglione *et al.*, 2012]. This was explained by Scaglione et al. [Scaglione *et al.*, 2012] as the microporosity in non-resorbable HA substitutes acts as the structure to which new deposited collagen fibers attaches. However, the role of microporosity in resorbable β-TCP bone substitutes is still unclear and not sufficiently understood.

The applied appraoch to understand the biological processes in the resorbable β-TCP substitutes is by characterizing the substitute structure before its implantation in terms of the morphometrical parameters (e.g. porosity, pore size, wall thickness, etc), then characterize the existing phases found after *in vivo* implantation, and relate these findings to the pre-implantation morphometrical parameters [Bashoor-Zadeh *et al.*, 2010; Lapczyna *et al.*, 2014; von Doernberg *et al.*, 2006]. This approach however did not allow to accurately characterize the ceramic resorption nor it allowed to study the 3D biological processes in reference to the pre-implantation geometric structure. Until now, a method that combines the pre-implantation substitute geometry to the post-implantation biopsy to localize resorbed material and links it to bone deposition to enable analysis of the interactions between bone deposition and substitute resorption at local level does not exist.

1.3 Problem statement

Several imaging techniques, providing different classes of images and leading to insight information about biological interactions taking place inside the resorbable implant, exist to better understand the bone repair process. These techniques has been used separately by the scientists to examine different hypotheses as shown in the detailed literature review presented in chapter 2. A systematic methodological integration of these classes of images is still required for an objective systematic evaluation of the scientific effects related to the osseointegration of the SBS. Specifically, this methodological integration can lead to more accurate segmentation and characterization of the phases in the SBS explanted biopsies and inherently to more accurate conclusions related to the bone repair process.

Microcomputed tomography, an image-based technique, allows examining the microstructure of radiopaque bone substitutes (i.e. bone substitutes that are opaque to the X-ray either because of their material composition or an added radiopaque agent) at the micro-scale and accordingly it has been recently deployed in examining the structure of porous substitutes used in the bone repair process. *In vivo* animal models, e.g. rabbits and sheep models, are used to examine the effectiveness of bone substitutes in the bone repair process. Specifically, these substitutes are implanted in critical-size bone defects and explanted systematically after predetermined implantation periods. The explanted biopsies are then cleaned from soft tissue and often embedded in polymeric resin and sectioned carefully for analysis such as histology, SEM and energy-dispersive X-ray spectroscopy (EDX). These techniques and methods have been very useful over the last century. However, they are labour intensive, often destructive and have limited accuracy in terms of characterizing the material phases and resorption in the biopsies.

This thesis attempts to introduce new methods and image based algorithms, combining images of different modalities and techniques including histology, SEM and mCT, to analyze post-implantation biopsies. Specifically, aligning the reference structure of the pre-implantation with the biopsy ceramic remnants structure provided access to accurate evaluation of the phases in the biopsy. Also, advanced multimodal analysis, combining histology, SEM and pre-implantation mCT data images provided access to a detailed description of the resorption process, micro- and macro-scales effects of the healing process.

1.4 Objectives of the PhD research project

The general objectives of this thesis is to formulate, develop, implement, verify and validate new imaging-based methods to study the phases found in biopsies explanted from experimental models used to study the effectiveness of porous bone substitutes for the repair of critical bone defects. Broadly, the thesis has two well-defined general objectives.

The first general objective of this thesis, related to developing a method to understand the biological processes at the 3D macroscale (i.e. structures and features of size larger than 50 microns), is subdivided into two sub-objectives. The first sub-objectives is to develop and implement a segmentation method to accurately isolate the three phases present of the explanted ceramic bone substitute scaffolds, i.e. bone, ceramic, and soft tissue. The second sub-objectives is to localize the resorption in the post-implantation mCT of the explanted biopsies of resorbing CaP bone substitutes.

The second general objective, related to developing a method to understand the microscopic effects at the microscale (i.e. structures and features of size less than 50 microns), is subdivided

into two sub-objectives. The first sub-objective is to introduce a new method to characterize the material phases found in toluidine blue histology (TBH) images of explanted biopsies of resorbable bone substitutes. The second sub-objective is to demonstrate the utility of the developed method by analyzing two groups of β-TCP substitutes of two different macropore sizes, explanted from an ovine model after implantation for six weeks.

These two general objectives are the subjects of two scientific papers included in the thesis and submitted for publication.

1.5 Organization of the PhD thesis

This thesis comprises five chapters, references, lists of acronyms, figures and tables. The contents of the chapters are described as follows.

Chapter 2 "literature review and methods", presents a review of the previous work related to the optimization of synthetic bone substitutes and the characterization of the bone substitute biopsies. In addition, this chapters reviews the methods used in the characterization of bone substitute biopsies, including imaging techniques (e.g. histology, SEM and mCT) as well as available image processing methods (e.g. denoising, segmentation, registration, etc). Further details of the selected methods (e.g. active contours) were reviewed and explained.

Chapter 3: This chapter presents the first article addressing the first general objective of this thesis. The article is entitled "A novel method for segmenting and aligning the pre- and post-implantation scaffolds of resorbable calcium-phosphate bone substitutes". A brief literature review, challenges, objectives and the novel method are described. In addition, an exemplary application of the method to one sample and the validation results of the methods are shown. The methods and results are discussed in the discussion section. Finally, the conclusions and references sections of this article are included in this chapter.

Chapter 4: This chapter presents the second article addressing the second general objective of this thesis. The article is entitled "Multimodal analysis of in vivo resorbable CaP bone substitute by combining histology, SEM and Microcomputed tomography data". The newly developed image-processing methods, including the segmentation and the alignment methods, are described in details in the materials and methods section. The utility of the novel method was demonstrated by characterizing quantitatively six samples of two different macropore sizes without pairing, explanted from an ovine model after implantation for six weeks. The novel method and the findings of the characterization process are discussed in light of the literature

and previous work. Finally, the conclusions and references of this article are included in this chapter.

Chapter 5: This chapter includes the summary of the results, contributions, and conclusions of the thesis.

References: In the references, the bibliography used in non-article chapters and sections are included.

CHAPTER 2

LITERATURE REVIEW AND METHODS

2.1 Bone defects and healing process

Bone in its two forms, cortical and trabecular, integrate together to satisfy several functions including reserve of minerals, blood production and mechanical functionalities [Weiner and Wagner, 1998; Zhao *et al.*, 2012; Zorzi, 2012]. Both types of blood cells, red and white, are produced by the hematopoietic marrow located in trabecular bone [Zhao *et al.*, 2012]. Mechanical functionalities of bone include protection of vital organs such as brain, providing body with rigid structure and movement. Therefore, the last function is the main promotion for bone grafting to assist the healing process to take place at the defect site [Bohner, 2010; LeGeros, 2008; Weiner and Wagner, 1998]. Based on cause, bone defects can be classified into traumatic or pathological which could be a result of osteoporosis, cyst or cancer [Nather, 2005; Spicer *et al.*, 2012]. Critical size defect is defined as the tissue defect that will not completely heal over the natural lifetime of human or animal [Spicer *et al.*, 2012].

2.2 Bone grafting and substitutes

Bone grafting could be defined as a surgical procedure for replacing missing bone in bone defects that can pose a significant health risk or fail to heal properly by itself [Habraken *et al.*, 2016]. Bone grafts may be used to fill critical-size defects [Bohner, 2010; LeGeros, 2008]. Bone grafting is classified into autograft, allograft, xenografting and synthetic bone grafting [Bohner, 2010].

Autograft procedures involves moving bone from one site to another site within the same patient [Bohner, 2010; Nather, 2005]. The need for bone into grafting procedures triggered the formulation of bone banking and resulted in technique involves implanting bone from other persons, which is allografting [Nather, 2005; Zorzi, 2012]. The high demanding and low availability of living bone donation triggered the searching for new source for grafting, the synthetic bone grafts [Bohner, 2010]. Moreover, autograft and allograft are associated with problems including pain and lack of donation sites in the case of autograft and disease transmission in the of allograft procedures [Bohner, 2010; Nather, 2005].

Due to the lack of bone resources required for allograft and problems resulting from autograft and allograft procedures, there is an increase in the use of synthetic substitutes including polymers synthetic ceramics such as bioactive glasses, calcium sulfates, calcium phosphates, calcium carbonate [Bohner, 2010; LeGeros, 2008]. Based on the ability to stimulate bone growth, synthetic substitutes could be classified into bioinert such as metal substitutes-the materials that do not stimulate bone and consequently do not bond with bone and results in weak interface

between bone and material, and bioactive such as natural polymers and calcium phosphate, the material that stimulate bone tissue formation and results in strong bone material bond and interface [LeGeros, 2008; Parikh, 2002].

2.3 Synthetic bone substitutes

Synthetic bone grafts includes polymers, bioactive glasses, ceramics and metals [Nather, 2005; Zorzi, 2012]. However, synthetic bone grafts should present biological properties that enable implant integration and healing of the defect as well as mechanical properties for structure support of bone at defect [Barrère *et al.*, 2006; LeGeros, 2008].

Synthetic polymers such as Polymethyl methacrylate (PMMA) have been widely used for treating bone defects, augmentation and coating of metal implants [Stańczyk and van Rietbergen, 2004; Zorzi, 2012]. Despite the long-term clinical experience and high immediate stability, PMMA is associated with polymerization heat which results in necrosis, pain and in some cases nerve injuries [Zorzi, 2012]. Hence, synthetic ceramics such as hydroxyapatite (HA) or tricalcium phosphate (TCP) are used for filling bone defects resulting from injuries [Gaasbeek *et al.*, 2005] or diseases such as cysts or cancer metastases [Wang *et al.*, 2013] as well as for oral implants pre-fixation augmentation [Zerbo *et al.*, 2005].

Synthetic ceramics such as calcium phosphates (CaP) biomaterials has similar composition to bone minerals which are calcium phosphate in the form of carbonate apatite [Barrère *et al.*, 2006; LeGeros, 2008; Nather, 2005]. It also exhibits other properties that enable bone growth including bioactivity, biodegradability, osteoconductivity and osteoinductivity [LeGeros, 2008; Podaropoulos *et al.*, 2009; Scaglione *et al.*, 2012; van der Pol *et al.*, 2010].

Addition of osteoinductive properties to CaP materials enhancing their application to bone repair and regeneration; could be done by the incorporation of calcium scaffolds with growth factors such as bone morphogenetic proteins (BMPs) [LeGeros, 2008; Polak *et al.*, 2011; Warren *et al.*, 2004]. For the limitations of BMPs in clinical use, other methods for osteoinductivity addition are used such incorporation of bone marrow stromal cells (BMSC) [Komlev *et al.*, 2006; Papadimitropoulos *et al.*, 2007], mesenchymal stem cells (MSC) [Warren *et al.*, 2004], platelet rich plasma (PRP) [Becker *et al.*, 2008] and the design of material with the appropriate geometrical properties including microporosity, macroporosity and concavities that favours entrapment of circulating growth factors and osteoprogenitor cells inducing neo-bone formation [LeGeros, 2008; Polak *et al.*, 2011].

Due to the clinical limitations of the BMPs including their carcinogenic effect and the high price [Becker *et al.*, 2008; Laine *et al.*, 2013], alternative solutions such as the PRP [Becker *et al.*, 2008], BMSC [Komlev *et al.*, 2006; Papadimitropoulos *et al.*, 2007], MSC [Warren *et al.*, 2004] emerged. Furthemore, the microporosity and the microstructuring of the ceramic stubtitute [Polak *et al.*, 2011] were demonstrated to improve the bone deposition and to accerlate the healing process. The type, density and pattern of the neo-bone formation could be controlled by the geometrical properties of the synthetic bone substitutes on macroscale [Feng *et al.*, 2012; Scaglione *et al.*, 2012] and on microscale [Barrère *et al.*, 2006; Hing *et al.*, 2005; Polak *et al.*, 2011].

2.4 Bone deposition in calcium phosphate ceramics

2.4.1 Kinetics of bone deposition inside scaffolds

Many experiments has been executed in order to measure the rate of bone growth but most of them were done in animal model ranging from mice [Komlev *et al.*, 2010, 2006; Mastrogiacomo *et al.*, 2006; Papadimitropoulos *et al.*, 2007; Scaglione *et al.*, 2012] rabbit [Feng *et al.*, 2012; Gauthier *et al.*, 2005; Lu *et al.*, 2002, 1998; van Lenthe *et al.*, 2007], sheep [van der Pol *et al.*, 2010; von Doernberg *et al.*, 2006] and dog models [Draenert *et al.*, 2013]. It has been observed that rate of bone growth could be affected by some parameters including material type, implantation site, animal models and geometrical properties of the implant.

One of the parameters that influence the bone deposition rate is the animal model in which the experiment is executed. As it is well-known that the metabolism in small animals is much higher than in large animals, it can be noticed that the larger the animal the slower the bone deposition rate. For example, in sheep model β-TCP scaffolds experienced lower bone deposition rate ($31.9 \pm 8.0\%, 38.5 \pm 9.8\%$ and 40.5 $\pm 12.3\%$ at 2, 4 and 12 months respectively) [van der Pol *et al.*, 2010]; in comparison with the higher bone regeneration observed in rabbit model (NBV = $35.00 \pm 6.64\%$ and $52.07 \pm 7.53\%$ at 12 and 24 weeks respectively in β-TCP) [Lu *et al.*, 1998]. It is shown in the following a review of some studies made to evaluate the bone deposition in different animal models.

After implantation in immunodeficient mice model with scaffolds seeded with bone marrow-derived mesenchymal stem cells (MSC), newly formed bone volume was maximum in Bio-Oss ones, natural bone mineral derived scaffolds, (8.4 $\pm$ 0.5 %) followed by the biphasic Skelite scaffolds (synthetic calcium phosphate multiphase biomaterial containing 67% silicon stabilized tricalcium phosphate) after 8 weeks implantation in mice (NBV=7.1 $\pm$ 0.5 %), and the lowest

bone volume were observed in the pure HA Engipore scaffolds (NBV=5.2$\pm$ 0.5 %) [Komlev *et al.*, 2010]. In similar study in mice [Papadimitropoulos *et al.*, 2007], mCT analysis of the postimplantation Si-TCP scaffolds seeded with MSC showed bone deposition increases from 2 (BV/TV = 5.5 $\pm$ 0.3%) to 4 months (BV/TV = 10.3 $\pm$ 0.5%) and remained constant in quantity but higher mineralization from 4 to 6 months (BV/TV = 10.2 $\pm$ 0.5%). Mineralization increase was observed by the shift in the new bone peak toward higher absorption rate in the mCT histogram. Once more, the stoppage of bone deposition was explained by the author according to two hypotheses; poor vascularization and lack of mechanical load which is peculiar in immunodeficient mice model. Therefore, they conducted new studies using ovine larger animal model to test the second hypothesis [Papadimitropoulos *et al.*, 2007].

The MSC seeded HA and β-TCP scaffolds exhibited increase in the osteocalcin (OCN), which is main indicator to the osteoblastic activity, from first to eighth week postimplantation in the back of male Fischer rats; accompanied with increase in bone formation which was observed as early as first week in close contact with the vasculature [Warren *et al.*, 2004]. Similar results were obtained in β-TCP seeded with bone marrow osteoprogenitor cells implanted in Fischer rats [Dong *et al.*, 2002], osteocalcin was observed to increase from 10ng/ml at second weeks postimplantation to 70ng/ml at week 24 postimplantation. In agreement, bone formation was observed at 2 weeks postimplantation inβ-TCP/BMO scaffolds with osteogenic medium and amount of mature bone increase until 24 weeks [Dong *et al.*, 2002]. Bone formation was close to the surface of the scaffolds without soft tissue formation. Moreover, roughness of the surface increased from week 2 to week 8, with existence of extracellular collagenous matrix as well as rough round osteoblastic cells at the surface. Blood vessels and multinucleated cells, which may contribute to the degradation, existed near the surface of the scaffold at week 24. Bone formed not only inside the scaffolds but also could be found at the outer surface of the scaffold.

In sake of understanding the orientation and pattern of deposited bone inside scaffolds [Scaglione *et al.*, 2012], both HA and HA-Col with 80% porosity seeded with bone marrow cells was implanted in mice. At one month postimplantation, almost all pores of the scaffolds were colonized with osteoprogenitor cells that had layered new tissue over the pores surface. Moreover, mature osteoblasts were lining the deposited bone matrix within pores of HA while cells were completely embedded in the woven bone matrix in HA-Col. At two-month postimplantation time point, the amount of the newly formed bone increased significantly inside the pores with elongated lining cells found covering the bone matrix. Moreover blood vessels were well represented within the interconnected pores. At six months after implantation, bone inside HA scaffolds showed the typical structure of an ossicle with a marrow cavity filled with hematopoi-

etic cells, adipocytes and formation of functionally active vascular structures, surrounded by concentric lamellae of bone matrix.

Postimplantation in immunodefficient mice of two different geometry HA scaffolds [Mastrogiacomo *et al.*, 2006]; spongy matrix and foaming, histological analysis exhibited neo-bone formation 2 weeks postimplantation in foaming scaffold whereas bone tissue did not exist in scaffold A at the same period despite BMSC density was higher in spongy matrix scaffold than in foaming ones. At 4 weeks postimplantation, neo-bone formation approached 35% of the total new tissue formed in scaffold B which is close to the value of 36% found at 8 weeks. On the other hand, neo-bone formation exhibited value of 22% of total new tissue formation in spongy matrix scaffold at 4 weeks and this value increase at 8 weeks postimplantation *in vivo* to be 37%. The faster bone formation rate in foaming scaffold proposes that neo-bone formation is affected by factors related to the implant (e.g. surface area available for bone growth and resorbability of the material) and others related to physiological equilibrium. The authors suggest that the coexistence of bone matrix, blood vessels, marrow and undifferentiated mesenchymal cells in steric but dynamic equilibrium would result in reaching neo-bone formation saturation level. This saturation level could be exceeded using resorbable material, i.e. β-TCP, which allows bone to grow in a manner proportional to resorption of the material [Mastrogiacomo *et al.*, 2006].

New bone formation was higher in β-TCP than HA scaffolds with better integration into host bone and higher penetration levels [Lu *et al.*, 1998]. Moreover, they have observed higher bone deposition at cortical site than in trabecular site. Postimplantation in rabbits, Higher bone regeneration was observed in cortical site (i.e. NBV = 35.00 $\pm$ 6.64% and 52.07 $\pm$ 7.53% at 12 and 24 weeks respectively in β-TCP) than in trabecular site (i.e. NBV = 22.39 $\pm$ 3.10% and 31.97 $\pm$ 9.34% at 12 and 24 weeks respectively in β-TCP) which is higher than medullar site (i.e. NBV = 14.64 $\pm$ 1.51% and 4.86 $\pm$ 4.84% at 12 and 24 weeks respectively in β-TCP) [Lu *et al.*, 1998]. Similar results were obtained by Feng and colleagues after 12 weeks implantation of β-TCP scaffolds of different geometry in large segmental defect of rabbit model, new bone volume was measured in the porous orthogonal rods (BV/TV=37$\pm$3) and spoke-like implant structures (i.e. cylindrical substitute with void space formed by orthogonally intersecting hollow tubes (BV/TV=34.8$\pm$3) [Feng *et al.*, 2012]. Comparable results obtained when two different granule size biphasic calcium phosphate (BCP); the fist material with 80-200 μm granules size and 200-500 μm granules size for the second one, were implanted for 6 weeks in 10 mature rabbit femur [Gauthier *et al.*, 2005]. According to the SEM histological analysis, neo-bone developed in close contact with BCP particles without any fibrous interface. According to quantitative mCT, The volume fraction of neo-bone formed inside defects with smaller granules was 38.5$\pm$5.5% whilst in the one with larger granules it was 24.8$\pm$3.6% [Gauthier *et al.*, 2005].

Once more in rabbit model for both HA and β-TCP exhibiting the same porosity of 50%, macropore size of 100-300 μm and interconnection size of 30-100 μm, histomorphometric analysis showed that both HA and β-TCP scaffolds exhibited neo-bone formation with few lacunae and many osteoblasts and a few osteoclasts at 3 weeks after implantation. At the period 8-24 weeks, β-TCP scaffolds exhibited more bone ingrowth in the whole scaffold from peripheries to the center accompanied with numerous osteoblasts and many osteoid tissues whereas HA scaffolds exhibited bone growth limited at the peripheries of the scaffold [Lu *et al.*, 2002].

After implantation of two HA scaffolds of different porosity; one has a cellular porosity of 55%, whilst the other one has a strut-like porosity of 32.2%, in sheep animal model for 33 days [Jones *et al.*, 2007]. The percentage of the porosity occupied by bone ingrowth is 27.8% for first and 39.8% for second; the overall volumetric bone growth is similar for the two scaffolds. In both specimens, the bone ingrowth appears to be predominately on the periphery of the scaffold with ingrowth concentrated along the pore surfaces. At 12 weeks postimplantation, average pore occupancy fraction of 68% for cellular and 61.5% for strut-like porous HA scaffolds [Jones *et al.*, 2007]. Comparable results observed in HA scaffolds implanted in mini pig mandible model, pore occupancy fraction of 40-50% was observed at 6 weeks and 70-80% at 18 weeks [Hollister *et al.*, 2005].

In another study in sheep model β-TCP has shown better osteoconductive properties than biocomposite scaffolds (i.e. poly lactic acid scaffolds) that has exhibited inflammatory reaction [van der Pol *et al.*, 2010]. Micro-CT evaluation of newly formed bone in the defects showed that bone ingrowth was minimum inside the biocomposite scaffolds at 2 (BV/TV = 1.8$\pm$1.1 %) and 4 months (BV/TV = 3.0$\pm$1.6 %) while it was intermediate at 12 months (BV/TV = 22.4$\pm$12.3 %). Bone concentrated at the peripheries of the scaffolds at two and four months time point in both biocomposite and empty defects while it was observed at the center of the β-TCP scaffolds at 4 months. Histomorphometrical evaluation of the explanted samples showed a fibrous tissue separating newly formed bone from the scaffold surface in biocomposite scaffolds with bone densities of 10.2 $\pm$ 3.7%, 12.6 $\pm$ 3.4% and 29.4 $\pm$ 4.8% at two, four and eight months respectively. Macrophages and foreign body cells were observed at 2 and 4 months and disappeared at 12 months. The soft tissue existence was a result of the inflammatory reaction which accompanies the release of lactic acid from the polymeric scaffold. This inflammatory reaction was not observed in β-TCP scaffolds which experienced higher bone deposition (31.9 $\pm$ 8.0%, 38.5 $\pm$ 9.8% and 40.5 $\pm$ 12.3% at 2, 4 and 12 months respectively) with osteoclastic activity observed till 4 months point [van der Pol *et al.*, 2010].

Adding microporosity to the scaffolds could result in better osteoconductive properties, bone growth and fast healing time similar to the use of BMPs which has many clinical restrictions

[Polak *et al.*, 2011]. In scaffolds with microporosity (MP) implanted in pigs, bone was uniformly distributed with respect to radial distance from the centers whilst in scaffold with no microporosity (NMP) bone concentrated near the perimeter of the scaffolds. In addition, microporosity had a significant influence on bone fraction while BMP did not, i.e., the BF was greater for samples with microporosity in comparison to the ones with NMP with BFs of 38.5$\pm$1.6% and 33.7$\pm$1.6, respectively. On the other hand, the BMP and no-BMP had statistically similar BFs of 34.8 $\pm$ 1.3% and 37.5 $\pm$ 1.6%, respectively. With respect to time, both MP and BMP samples reached stability in terms of BF by 3 weeks, and accordingly healing time of 6 weeks which is two times faster than the ones with neither MP nor BMP. Furthermore, scaffolds with BMP as well as the ones with microporosity experienced uniform radial bone distribution [Polak *et al.*, 2011].

Dog animal model was also used for testing the effectiveness of the bone substitutes. Hydroxyapatite and β-TCP scaffolds of 600-μm pore size were implanted in tibial defects of German Sheppard dogs [Draenert *et al.*, 2013]. In this study, complete healing was exhibited in β-TCP after 6 weeks with bone deposition covering completely the scaffold surface and in direct contact pattern with it, revealing osseointegration with scaffold. The cancellous bone was completely reconstructed after 4 months in β-TCP scaffolds. On the other hand, HA implants exhibited fully mineralized woven bone growth at depth limited to two pores from the scaffold peripheries at 6 weeks postimplantation. Osseo-integration in HA scaffolds continued at 2 months postimplantation, exhibiting ordered lamellar bone growth in scaffold pores and ceramic integration in the hosting bone as building block in the hosting cancellous structure. Noteworthy, micropores (even smaller than 5 μm) exhibited bone ingrowth. At 4 months postimplantation, HA scaffolds showed strong bone support using compact bone near cortical bone and in the outer pores of the scaffold in addition to fully mineralized mature lamellar covering the surface of the scaffold bordering pores and acting as bone reinforcement of the scaffolds. At 15 months postimplantation, ceramic was further reinforced with lamellar bone with normal bone marrow appearance. Moreover phagocytised ceramic particles were observed at this period [Draenert *et al.*, 2013]. In another study, β-TCP granules of size 250-500 μm, were implanted in iliac dog defect of 10 mm and resulted in bone surface fraction of 40.31$\pm$5.42% in β-TCP group after 4-month implantation [Podaropoulos *et al.*, 2009].

Unlike animal models, biopsies in human cannot be taken unless it does not affect the healing process which means it can be taken after the osteotomy at 6-24 months postimplantation [Gaasbeek *et al.*, 2005] or at reoperation for disease recurrence at 7 and 10 months postimplantation [Wang *et al.*, 2013]. Several facts could influence bone deposition and healing process in human

which do not exist in animal models such as smoking which result in poorer bone deposition [Vandeweghe and De Bruyn, 2011].

2.4.2 Bone deposition penetration level

For porous scaffolds, neo-bone deposition started and concentrated near the periphery of the scaffold at early time of implantation [Feng *et al.*, 2012; Hollister *et al.*, 2005; Jones *et al.*, 2007; Lu *et al.*, 2002; Polak *et al.*, 2011; Scaglione *et al.*, 2012; von Doernberg *et al.*, 2006]. In some studies, bone continued to concentrate at the peripheries while bone fraction at the center of the scaffold was very low even long time post implantation. In HA scaffolds, at 63 days pore occupancy fraction at the center was 10% while it reached 45% at the peripheries while at 84 days values over 60% pore occupation fraction (POF) was observed at the center [Jones *et al.*, 2007]. In another study [Hollister *et al.*, 2005], average pore occupancy fraction of 40-50% was observed with POF (10-16%) at innermost in pore sizes greater than 600 μm and (4-8%) innermost pores of 400 μm pore size scaffolds. Bone ingrowth concentrated at the peripheries of porous HA scaffolds at 8-24 weeks of implantation [Lu *et al.*, 2002]. Conversely, in highly resorbable scaffolds β-TCP scaffolds bone deposition extended to the center area of the scaffolds at 8 weeks [Lu *et al.*, 1998], 12 weeks [von Doernberg *et al.*, 2006] and only tubular scaffolds [Feng *et al.*, 2012]. For better bone penetration and uniform distribution with respect to the distance from peripheries, addition of microporosity exhibited perfectly uniform radial bone distribution (RBD=0.51) in porous HA scaffolds [Polak *et al.*, 2011].

2.4.3 Influence of scaffold geometrical properties on bone deposition at macroporous level

Bone deposition inside scaffolds could be characterized using geometrical parameters of the scaffold that could control the type, density and pattern of the neo-bone formation [Feng *et al.*, 2012; Scaglione *et al.*, 2012]. As bone deposition takes place at the surface of the implanted scaffold [Dong *et al.*, 2002; Jones *et al.*, 2007; Komlev *et al.*, 2010; LeGeros, 2008; Lu *et al.*, 2002; Scaglione *et al.*, 2012], targeted bone regeneration was controlled by driving collagen fibers assembly via the specific biomaterial design [Scaglione *et al.*, 2012]. The use of an ordered and confined geometry of hydroxyapatite (HA) foams resulted in collagen fibers concentration within pores and formed compact lamellar bone [Lu *et al.*, 2002; Scaglione *et al.*, 2012]. Conversely, the use of nanofibrous collagen-based sponges (HA-Col) resulted in a nematic phase distribution of new collagen fibers and formed woven isotropic bone [Scaglione *et al.*, 2012].

The interpretation of the trabecular patterns of bone was observed inside β-TCP scaffolds using radiological [van der Pol *et al.*, 2010; von Doernberg *et al.*, 2006] and histological [Feng *et al.*, 2012] analyses. Likewise biocomposite (PLA/β-TCP) [van der Pol *et al.*, 2010], in CaP bone cement (CPC) [Lu *et al.*, 2002] and in injectable calcium phosphate bone substitute [Gauthier *et al.*, 1999, 2005], trabecular bone growth was observed in direct contact with the substitute granules. However, woven bone was observed at the implant peripheries in early stage, 2 weeks in CPC [Lu *et al.*, 2002] and 3 weeks in HA and β-TCP scaffolds [Lu *et al.*, 1998], of bone formation. In large segmental defects, porous β-TCP scaffolds experienced bone deposition at the peripheries with soft tissues at the center of the scaffolds while bone deposition in tubular scaffolds approached the center of scaffold with restoration of the marrow cavity achieving recanalization [Feng *et al.*, 2012].

Pore size could affect the volume [Hollister *et al.*, 2005] and pattern [Hing *et al.*, 2005] of deposited bone inside the scaffold. In larger pore size HA scaffolds bone exhibited deposition in the form of islands in the middle of pores while in smaller pore HA scaffolds bone was deposited on the surface of the material [Hing *et al.*, 2005]. Moreover significantly higher bone deposition volume was observed in the first 3 weeks in larger pores size scaffolds [Hing *et al.*, 2005]. In addition mineral apposition rate was higher in larger pore size scaffolds [Hing *et al.*, 2005]. Despite no statistical significant difference was noted in total bone fill based on either pore size or pore geometry, larger pores tends to favour bone ingrowth [Hollister *et al.*, 2005]. Higher POF (10-16%) at innermost in pore sizes greater than 600 μm at 6 weeks was observed, whereas in pore size of 400 μm innermost pores POF was 4-8% [Hollister *et al.*, 2005].

In addition to influencing the pattern of deposited bone inside the scaffolds as shown previously, pore shape could influence bone deposition volume inside scaffolds [Jones *et al.*, 2007; Mastrogiacomo *et al.*, 2006]. While both scaffolds exhibited similar overall bone volume deposition at early time point, cellular HA scaffolds exhibited higher bone volume than strut-like porous HA ones at late time point. An early time point (33 days) and for two scaffolds of different geometrical porosity, one has a cellular porosity of 55% and mean pore radius of 136 μm, whilst the other one has a strut-like porosity of 32.2% and mean pore radius of 126 μm. The percentage of the porosity occupied by bone ingrowth is 27.8% for first and 39.8% for second; the overall volumetric bone growth is similar for the two scaffolds. In both specimens, the bone ingrowth appears to be predominately on the periphery of the scaffold with ingrowth concentrated along the pore surfaces. At late time point (84 days) cellular scaffolds exhibited average pore occupancy fraction (POF) of 68% while strut-like porous scaffolds exhibited POF of 61.5% [Jones *et al.*, 2007]. Histological analysis exhibited neo-bone formation 2 weeks postimplantation in foaming HA scaffolds whereas bone tissue did not exist in spongy matrix scaffold at the same period de-

spite BMSC density was higher in the spongy matrix than in foaming scaffolds [Mastrogiacomo *et al.*, 2006]. According to author [Mastrogiacomo *et al.*, 2006], the faster and more efficient bone formation in foaming scaffolds (i.e. scaffolds in the form of interconnected spheres) could be a result of the *"filter effect"* of the scaffold (i.e. scaffolds of small pore and interconnection sizes could result in higher cell density closer to the peripheries of the scaffold). Also, the appropriate choice of granule size could result in better bone deposition and healing process [Gauthier *et al.*, 2005]. According to the SEM histological analysis, neo-bone developed in close contact with BCP particles without any fibrous interface. According to quantitative mCT, The volume fraction of neo-bone formed inside defects with smaller granules (80-200 μm) was 38.5$\pm$5.5% whilst in the one with larger granules (200-500 μm) it was 24.8$\pm$3.6% [Gauthier *et al.*, 2005].

Not only deposited bone volume is influenced by scaffold geometry but also vascularization inside the scaffolds is affected by the geometrical properties such as pore interconnection size [Mastrogiacomo *et al.*, 2006] and scaffolds structure [Feng *et al.*, 2012]. Vascularization was related to the interconnection size in both scaffolds [Mastrogiacomo *et al.*, 2006]. In spongy matrix scaffolds, which exhibited higher inter connection size, higher number of large blood vessels was found (mean diameter: 91$\pm$38 μm) whilst large blood vessels were never observed running through several consecutive pores in foaming scaffolds (mean diameter: 61$\pm$18 μm), the one with lower interconnection size, yet the vascularization was well represented [Mastrogiacomo *et al.*, 2006].

Scaffolds geometry can affect the vascularization inside the scaffolds and consequently the bone deposition [Feng *et al.*, 2012]. Vascularization in TCP was analyzed using ECT at 2, 4, 8 and 12 weeks after surgery [Feng *et al.*, 2012]. The uptake ratio in defect region increased with time achieving steady state gradually 4 weeks after surgery. Both tubular and porous scaffolds showed comparable uptake ratio (i.e.The uptake ratio of $^{99m}T_c - MDP(T/NT)$ between the implant site and the contralateral radius) at week 2 while tubular scaffolds showed higher perfusion at week 4 than porous ones. Twelve weeks post surgery, tubular scaffolds reached uptake ratio of 4.0$\pm$0.3 which is higher than porous groups (2.77$\pm$0.32) [Feng *et al.*, 2012]. A proposed explanation for this phenomenon could be porous scaffolds with its structure are exposed to the surrounding environment which sustains inflammatory reaction accompanied with traumatic condition of segmental bone. This inflammatory reaction is acknowledged for possibility of inhibiting the process of vascularization [Feng *et al.*, 2012; Rücker *et al.*, 2006; Sung *et al.*, 2004].

2.4.4 Influence of scaffold geometrical properties on bone deposition at microporous level

Addition of osteoinductive properties could increase the bone deposition, decreases healing time and extends bone deposition toward the center of implant resulting in uniform bone distribution inside the scaffold, at early time and (6 weeks) in HA scaffolds [Polak *et al.*, 2011]. There are two methods that can be used to add osteoinductive properties to the CaP materials to further enahnce their application in the bone repair: (1) incorporating the CaP scaffolds with growth factors such as BMPs; and (2) designing the CaP scaffolds with the appropriate geometrical properties including microporosity, macroporosity and concavities that favour entrapment of circulating growth factors and osteoprogenitor cells inducing neo-bone formation [LeGeros, 2008; Polak *et al.*, 2011]. Surface characteristics of the scaffolds affect bone deposition pattern as well as healing time of the defect [Polak *et al.*, 2011; Scaglione *et al.*, 2012]. Microporosity is one of the properties that have been proven to play crucial role in bone deposition. It has been shown that scaffolds with microporosity have faster healing time (6 weeks) than ones without microporosity (12-24 weeks) [Polak *et al.*, 2011]. Also, According to the analysis of bone fraction and radial bone distribution, the microporosity appeared to ensure that a given bone volume was distributed more uniformly. Concluding that the effect of including microporosity in a scaffold could be increasing bone fraction as compared to a scaffold without microporosity and promoting a more uniform bone distribution [Polak *et al.*, 2011]. osteoblasts recognize and attach to the surface of the scaffolds depositing collagen fibers infiltrating its micropores [Scaglione *et al.*, 2012].

Another method to add osteoinductive properties is the use of osteoprogenitor stem cells [Dong *et al.*, 2002; Warren *et al.*, 2004] or bone marrow stromal cells [Komlev *et al.*, 2006; Papadimitropoulos *et al.*, 2007]. Bone deposition was observed in HA and β-TCP scaffolds seeded with mesenchymal stem cells as early as 1 week in one study [Warren *et al.*, 2004] and 2 weeks in another study [Dong *et al.*, 2002]. In the control group with non-osteogenic medium, many blood vessels were observed at 2 weeks postimplantation [Dong *et al.*, 2002]. However, soft tissue formed inside the scaffolds without bone formation even at 8 weeks postimplantation. Conversely, bone formation was observed at 2 weeks postimplantation in β-TCP/BMO scaffolds with osteogenic medium and amount of mature bone increase until 24 weeks. Bone formation was close to the surface of the scaffolds without soft tissue formation. Moreover, roughness of the surface increased from week 2 to week 8, with existence of extracellular collagenous matrix as well as rough round osteoblastic cells at the surface. Blood vessels and multinucleated cells, which may contribute to the degradation, existed near the surface of the scaffold at week 24.

Bone formed not only inside the scaffolds but also could be found at the outer surface of the block [Dong *et al.*, 2002].

The clinical use of the BMPs is limited because of their potential complications (Laine et al., 2013). In addition, the BMPs have high price compared to PRP [Becker *et al.*, 2008]. Also, MSCs and BMSCs could result in post-operative complication in addition to the difficulty of extracting them in sufficient numbers [Zorzi, 2012]. Therefore, microporosity seems to be an efficient and safe method to add osteoinductive properties to CaP bone substitutes. Yet, the mechanisms, by which microporosity results in better osseointegration, are still not sufficiently understood.

2.4.5 Tissue reaction to bone scaffold

Tissue reacts differently to implants depending on the implantation site; highest bone deposition was observed at cortical bone followed by cancellous bone and lowest at medullar cavity. Biodegradation of the scaffolds was in reverse to the bone deposition; highest in medullar cavity, higher in cancellous and lowest in cortical bone. Furthermore, correlation between bone deposition rate and degradation rate of the material was observed in β-TCP scaffolds [Lu *et al.*, 1998]. Higher bone regeneration was observed in cortical site (i.e. NBV = 35.00 $\pm$ 6.64% and 52.07 $\pm$ 7.53% at 12 and 24 weeks respectively in β-TCP) than in trabecular site (i.e. NBV = 22.39 $\pm$ 3.10% and 31.97 $\pm$ 9.34% at 12 and 24 weeks respectively in β-TCP) which is higher than medullar site (i.e. NBV = 14.64 $\pm$ 1.51% and 4.86 $\pm$ 4.84% at 12 and 24 weeks respectively in β-TCP) [Lu *et al.*, 1998].

2.4.6 Biomechanical evaluation of bone scaffold postimplantation

One of the main functions of the implants is to bear mechanical loading resulting from daily life. Measurement of the mechanical strength of scaffolds before and postimplantation is crucial for evaluation of implant success [Dong *et al.*, 2002; Feng *et al.*, 2012; Gauthier *et al.*, 2005]. Tubular scaffolds exhibited higher compressive strength in both pre and post implantation in rabbit (8.1$\pm$0.44 MPa native and 49.89$\pm$2.62 MPa harvested) compared to porous ones (3.24$\pm$0.48 MPa native and 37.12$\pm$2.13 MPa harvested) [Feng *et al.*, 2012]. Furthermore, bony callus formation in the interspace between scaffolds and hosting bone was very important to support the scaffold and lack of it resulted in failure of scaffolds at the compressive strength test [Feng *et al.*, 2012]. Yield strength of the sample with smaller ceramic granules (80-200 μm) was 26.8$\pm$4.5MPa versus 18$\pm$5.4MPa for the one with larger ceramic granules (200-500 μm) which are higher than non-implanted rabbit femur (2.8$\pm$1.6MPa) [Gauthier *et al.*, 2005].

Compressive strength of the beta-TCP scaffolds of 75% and average pore size of 200-400 μm at 24 weeks postimplantation in Fischer rats was observed to be similar to the cancellous bone which is 1-12 MPa whereas the elastic compressive modulus was higher than cancellous bone (50-400 MPa) [Dong *et al.*, 2002].

2.5 Resorption of calcium phosphate ceramic substitutes in bone

One of the main targets for tissue engineering is to restore tissues at defect site to the previous healthy status [Zorzi, 2012]. For the similar mineral composition to bone and being osteoconductive and osteoinductive [Draenert *et al.*, 2013; LeGeros, 2008; Mastrogiacomo *et al.*, 2006; Scaglione *et al.*, 2012], the use of calcium phosphate scaffolds for tissue engineering applications is very promising. However, the manufacturing process of CaP scaffolds controls the properties of the scaffold including crystallization, surface roughness and solubility [LeGeros, 2008; Lu *et al.*, 2002] which affects directly the ability of the hosting body to resorbe the material [LeGeros, 2008; Lu *et al.*, 2002]. The use of non-resorbable material such as hydroxyapatite could result in limitation of bone ingrowth [Komlev *et al.*, 2010; Lu *et al.*, 1998; Mastrogiacomo *et al.*, 2006]. Therefore, the utilization of resorbable scaffolds arises as a solution to enable bone growth and replacement of the scaffold by normal bone tissues. Yet, the resorption rate of material should be controlled to ensure the adequate replacement of the scaffold by bone growth in the defect site to ensure the functionalities of the implant such as weight bearing. Hence, the need of developing better understanding of the resorption process and the effective factors in such a process attracts the attention of scientists.

Biodegradation or resorption of calcium phosphate takes place not only through single mechanism but trough multiple ones depending on the composition of the material and cellular activity, i.e. osteoclastic activity and dissolution phenomena. It has been shown that osteoclastic activity participate partially in degradation of calcium phosphate ceramics [Gauthier *et al.*, 1999, 2005; Lu *et al.*, 2002; Zerbo *et al.*, 2005]. Other cellular activities, such as foreign body reaction and inflammatory reaction, have been shown to contribute in degradation of ceramic [Becker *et al.*, 2006; Draenert *et al.*, 2013; LeGeros, 2008; Lu *et al.*, 2002] and polymeric implants [van der Pol *et al.*, 2010]. However in other cases, ceramic degradation was observed despite the rare observation of osteoclasts and phagocytes and consequently this has led the author to propose that the main biodegradation mechanism is through biological dissolution of the material [Lu *et al.*, 2002, 1998]. Another explanation of this phenomenon was the low pH level achieved by metabolic activity of these cell masses, which could produce acidic by-products, and poorly

developed vascularization, could result in chemical dissolution of TCP [Zerbo *et al.*, 2005]. Degradation of β-TCP scaffolds continued from week 12 (34% degradation rate) to week 24 (55% degradation rate) despite the rare existence of osteoclasts and macrophages [Lu *et al.*, 2002].

Biodegradation rate is highly influenced by the material composition while the mechanism of biodegradation depends on the material crystallization process, i.e. materials made using physicochemical process (e.g. CaP bone cement) favors degradation based on both dissolution and cellular activities while sintered material showing good crystallization (e.g. β-TCP) is primarily degraded via extracellular dissolution [Lu *et al.*, 2002]. CaP biodegradability is controlled by its properties including composition, particle size, cystallinity, porosity, and preparation conditions [LeGeros, 2008]. These experiments showed that the degradation rate can be ordered as following; β-TCP $\gg$ bovine bone Ap (unsintered)$\gg$ bovine bone Ap (sintered)>coralline HA>HA. BCP degradation rate depends on the ratio of HA/ β-TCP; the higher the ratio the lower the degradation rate [Barrère *et al.*, 2006; LeGeros, 2008]. Furthermore, incorporation of different ion to the apatite can increase or decrease the degradation rate; e.g. β-TCP solubility was decreased by incorporation of either Zn2+ or Mg2+ ions [Barrère *et al.*, 2006; LeGeros, 2008].

The geometry of scaffold affects the degradation rate of the scaffold. Porous β-TCP scaffolds exhibited higher degradation in segmental defect compared to tubular or solid β-TCP scaffolds [Feng *et al.*, 2012]. However, this rapid degradation porous β-TCP scaffolds could result in the early disintegration of overall structure, eliminating the space for the bone tissue formation, and the TCP degradation debris may block the porous channel for the ingrowth of vessel and bone tissues [Detsch *et al.*, 2008]. Osteoclasts, macrophages and osteoblasts have exhibited the ability of infiltration of material through its microporosity at level down to 5 μm [Gaasbeek *et al.*, 2005; Zerbo *et al.*, 2005]. Moreover, Cellular interaction to calcium phosphate implants, through the controlling protein adsorption into surface and ionic release, influences the bone regeneration and resorption of the implant hence surface properties of the implant should be considered at scaffold design [Barrère *et al.*, 2006].

There is more than one pattern for implant degradation including resorption pockets, wall thinning and fragmentation to smaller granules. All three patterns were shown to take place simultaneously in Si-TCP scaffolds where resorption took place mainly at the bone deposition pockets accompanied with uniform wall thinning and fragmentation with thickness mean decreased from 215$\pm$175 to 134$\pm$123 at 8 weeks postimplantation [Komlev *et al.*, 2010; Papadimitropoulos *et al.*, 2007]. Despite the resorption was generally unnoticeable in HA scaffolds, high resolution image showed many small resorption pockets and phagocytised ceramic particles [Draenert *et al.*, 2013]. Segmentation of scaffold into smaller particles which was invaded and infiltrated

by both osteoblasts and osteoclasts was observed in b-TCP scaffold postimplantation in human tibia for 6-25 months [Gaasbeek *et al.*, 2005]. Fragmentation was also observed accompanied with phagocytosis in calcium phosphate cement implant at 2, 4 and even 24 weeks postimplantation [Lu *et al.*, 2002]. Resorption was shown to take place in direct contact with neo-bone formation [Podaropoulos *et al.*, 2009] and parallel to it starting from peripheries toward the center of implant [Lu *et al.*, 2002]. β-TCP scaffold dissolution by osteoclastic activity via surface erosion pattern was observed in human biopsies [Gaasbeek *et al.*, 2005].

As fast resorption in porous β-TCP scaffolds could result in the early disintegration of overall structure [Detsch *et al.*, 2008], control of scaffold degradation rate to be in agreement with bone deposition and overall mechanical loading is critical for implant success. One of the methods used to control degradation of β-TCP scaffolds is through early bone deposition over the surface of the scaffold decreases the degradation of β-TCP through the extracellular dissolution and favors degradation by cellular activities such as multinuclear cells which was observed at late time (12 and 24 weeks) postimplantation at the surface of the scaffold near blood vessels [Dong *et al.*, 2002]. Bone formation started as early as two weeks in the scaffolds with BMO and continued two 24 weeks postimplantation with maturation approached at 4 weeks with mature osteocytes embedded in bone matrix. Newly deposited bone was formed at the surface of the scaffold without soft tissue in between. Another method to control scaffold resorption is by the use of biphasic calcium phosphate cement which could be generated by mixing hydroxyapatite (HA) and β-TCP at different ratios [Barrère *et al.*, 2006]; the higher the ratio the lower the degradation rate [LeGeros, 2008].

2.6 Characterization of calcium phosphate bone substitutes

Bone scaffolds are intended to be used for treatment and filling of critical size bone defects [Gauthier *et al.*, 2005; Hollister *et al.*, 2005]. Therefore, optimum bone scaffold should sustain the mechanical loading at the defect place, promote bone growth and degrade in controlled rate to be replaced finally by bone [Carlier *et al.*, 2011]. However, the main difficulties associated with optimal design of bone scaffold include the tradeoffs between the several functions that should be adjusted, such as mechanical loading support and resorption [Bohner *et al.*, 2011]. Enormous research efforts were conducted in the sake of optimizing ceramic CaP bone scaffold, yet the complete answer is still undisclosed [Bohner *et al.*, 2011; Carlier *et al.*, 2011].

Development of better understanding of the factors that affect bone growth, scaffold degradation and relation between them can help optimizing the scaffold design. Hence, assessment of

bone growth characteristics (patterns, thickens, volume, paths, deposition rate and locations, integration with host bone...etc), scaffold degradation and scaffold geometrical properties on both macro and micro scale is required not only post-implantation but also in comparison to scaffold pre-implantation characterization [Jones *et al.*, 2007; Komlev *et al.*, 2010; Polak *et al.*, 2011; Scaglione *et al.*, 2012; von Doernberg *et al.*, 2006]. These measurements should be three dimensional (3D), non-destructive and non-invasive because the characterization of the scaffold should be done pre-implantation [van Lenthe *et al.*, 2007]. The characterization of biological processes in post-implantation CaP substitutes should be done at two levels macro and microprous levels. Whereas mCT provides a tool for 3D morphometrical characterization of phases in bone substitutes, histology and SEM provides accessibility to morphometrical characterization at the micro-porous level [Bashoor-Zadeh *et al.*, 2010; Jones *et al.*, 2007; Komlev *et al.*, 2010; Polak *et al.*, 2011; Scaglione *et al.*, 2012; van Lenthe *et al.*, 2007; von Doernberg *et al.*, 2006].

2.6.1 Microcomputed tomography

Microcomputed tomography (mCT) is a technique that is used for 3D quantification, modeling and analysis of internal structure of objects using X-ray imaging [van Lenthe *et al.*, 2007]. This technique provides 3D imaging capabilities with wide range of isometric resolution starting from few millimetres in clinical CT to 100nm in the case of synchrotron radiation nano-CT [van Lenthe *et al.*, 2007]. The practical aspects of mCT , which have become commercially available for clinical and research purposes, have been highlighted recently [Jones *et al.*, 2007; Müller and Rüegsegger, 1997; Parkinson *et al.*, 2008; Polak *et al.*, 2012; van Lenthe *et al.*, 2007]. As an accurate and validated techniques, mCT has been used in research related to characterization bone architecture [Buie *et al.*, 2007; Demenegas *et al.*, 2011; Elmoutaouakkil *et al.*, 2002; Parkinson *et al.*, 2008] as well as porous bio-scaffolds [Bashoor-Zadeh *et al.*, 2010, 2011; Hollister *et al.*, 2005]. In addition, mCT has been used for characterization of bone ingrowth inside bio-scaffolds *in vitro* [Cartmell *et al.*, 2004; van Lenthe *et al.*, 2007] and explanted *in vivo* samples [Feng *et al.*, 2012; Jones *et al.*, 2009; Komlev *et al.*, 2006; Papadimitropoulos *et al.*, 2007; von Doernberg *et al.*, 2006].

The three dimensional (3D) nature of the scaffolds and bone favors the mCT over other 2D characterization techniques such as histological and histomorphometrical analysis [Bashoor-Zadeh *et al.*, 2010; van Lenthe *et al.*, 2007]. In addition, the characterization should be done pre and post-implantation, hence the characterization should be non-destructive and non-invasive [Komlev *et al.*, 2006; Podaropoulos *et al.*, 2009]. Microcomputed tomography (mCT) seems to be the best solution for the 3D requirements of the analysis and characterization [Bashoor-Zadeh *et al.*, 2010; Komlev *et al.*, 2010; Papadimitropoulos *et al.*, 2007; van der Pol *et al.*, 2010;

van Lenthe *et al.*, 2007]. Gray level in mCT images represents the X-ray attenuation of the material through which the beam penetrates, therefore similar materials results in similar X-ray attenuation and consequently similar gray level. Mineral crystals are largely responsible for the X-ray attenuation in both bone and ceramic bio-scaffolds. This similarity arises as a major problem for the *in vivo* characterization of bone growth in β-TCP scaffolds [van der Pol *et al.*, 2010], biphasic calcium phosphate (BCP) [Gauthier *et al.*, 2005] and HA [Hilldore *et al.*, 2009].

Despite the advantages of mCT, its utilization encounters the challenge of finding the appropriate segmentation algorithm especially for the β-TCP scaffolds which have similar X-ray absorption results from their high resorption rate. This problem resulted in overestimation of bone in comparison to histomorphometrical analysis due to the difficulty to establish threshold between bone and scaffold remains for β-TCP material [van der Pol *et al.*, 2010], biphasic calcium phosphate (BCP) [Gauthier *et al.*, 2005] and HA [Hilldore *et al.*, 2009]. The degradation rate of ceramic scaffolds could be classified as following; $\beta - \text{TCP} \gg$ bovine bone Ap (unsintered) $\gg$ bovine bone Ap (sintered)> coralline HA > HA while BCP degradation rate depends on the ratio of HA / β-TCP; the higher the ratio the lower the degradation rate ([LeGeros, 2008]. Hence, the difficulty of finding the suitable segmentation algorithm of mCT is higher for β-TCP than other ceramics and this will be shown in further details in the following literature. Moreover, the alignment and volume registration of scaffold pre-implantation and the explanted scaffold remains arise as another challenge associated with assessment of *in vivo* β-TCP scaffolds for the high resorption rate of β-TCP material. To the author's knowledge, there is no approach for 3D volume registration (i.e. aligning the structures in the images acquired from different modalities such as histology, SEM, pre- and post-implantation mCT dataset) for β-TCP scaffolds because of their high resorption rate and the geometrical changes.

2.6.2 Histology evaluation

Histology has been used for characterizing bone tissues inside bone substitutes in many studies [Feng *et al.*, 2012; Lapczyna *et al.*, 2014; Mastrogiacomo *et al.*, 2006; Papadimitropoulos *et al.*, 2007; Scaglione *et al.*, 2012; Stalder *et al.*, 2014; Theiss *et al.*, 2005; van der Pol *et al.*, 2010; von Doernberg *et al.*, 2006]. Different stains including Van Gieson [Feng *et al.*, 2012], hematoxylin/eosin [Mastrogiacomo *et al.*, 2006; Papadimitropoulos *et al.*, 2007; Scaglione *et al.*, 2012] and toluidine blue stained histology (TBH) stains [Lapczyna *et al.*, 2014; Stalder *et al.*, 2014; Theiss *et al.*, 2005; von Doernberg *et al.*, 2006] were commonly used to characterize the bone tissue inside the explanted bone substitutes. In particular, toluidine blue stained histology (TBH) was used to characterize bone deposition and substitute resorption in β-TCP bone substitutes [Feng *et al.*, 2012; Lapczyna *et al.*, 2014; Stalder *et al.*, 2014; Theiss *et al.*, 2005;

van der Pol *et al.*, 2010; von Doernberg *et al.*, 2006]. In brief, the cut sections were stained using toluidine blue staining, to which bony tissues react by absorbing the staining and exhibit blue color. Afterwards, the sections are magnified and imaged using light macroscope equipped with high resolution digital camera. Finally, the captured digital images are stored for processing. Histology images provide access to information at submicron level. However, the segmentation of TBH encountered a challenge to segment phases accurately in addition to determining the boundaries of the substitute at the implantation time.

2.7 Image processing methods for characterizing calcium phosphate bone substitutes

2.7.1 Image enhancement

Noise suppression using image filtering was used in mCT image enhancement for *in vivo* samples [Buie *et al.*, 2007; Papadimitropoulos *et al.*, 2007; Polak *et al.*, 2012; Sebastian *et al.*, 2003; van der Pol *et al.*, 2010; Waarsing *et al.*, 2004]. Image filtering could be classified into isotropic, such as Gaussian filtering, and anisotropic filtering methods [Perona and Malik, 1990].

Gaussian filtering was used for noise reduction in images of mCT of *in vivo* bone CaP ceramic implants [Gauthier *et al.*, 2005; Landrigan, 2009; van der Pol *et al.*, 2010; van Lenthe *et al.*, 2007]. However, the blurring nature of Gaussian filtering technique resulted in fading the edges of bone and scaffolds in the reconstructed mCT projections. Hence, bone volume fraction resulted from mCT analysis disagreed with the one resulted from histomorphometrical [van der Pol *et al.*, 2010]. In another study, Overestimation of newly deposited bone calculated using mCT in comparison to SEM was measured [Gauthier *et al.*, 2005]. Therefore, the need of the combination of noise reduction without affecting the accuracy of segmentation steered the researchers to the edge-preserving filtering methods such as anisotropic diffusion [Jones *et al.*, 2004; Papadimitropoulos *et al.*, 2007; Sheppard *et al.*, 2004].

Among the techniques that have been shown to be effective in noise reduction is the edge-preserving noise reduction method which was proven to improve signal to noise ratio (SNR) in tomographic images [Gonzalez and Woods, 2008]. There are two emerging edge-preserving noise reduction alternatives, nonlinear anisotropic diffusion [Catté *et al.*, 1992; Weickert, 1998] and wavelet transform filtering [Mallat, 1989]. Both techniques are considered the most effective alternatives for noise reduction in image processing [Sheppard *et al.*, 2004]. However, nonlinear anisotropic diffusion has been proven to more effective than wavelet transform filtering in images which has signal frequencies below half the Nyquist limit [Frangakis and Hegerl, 2001]

such as tomographic reconstructions [Sheppard *et al.*, 2004]. Therefore, nonlinear anisotropic diffusion was selected to reduce the noise in mCT images.

In the present thesis, anisotropic diffusion was used for noise suppression in mCT images which in addition to noise reduction enhances the edges in the image [Perona and Malik, 1990]. Edge enhancement while removing noise is very crucial in images which contains phases of comparable gray values such as bone and β-TCP [Jones *et al.*, 2007; Papadimitropoulos *et al.*, 2007; Sheppard *et al.*, 2004].

Noise reduction using anisotropic diffusion filtering

We propose to use the anisotropic diffusion filtering method for the abovementioned reasons. In sum, blurry edges is the price being paid for noise elimination using conventional low pass filtering techniques such as Gaussian filtering. On contrary, anisotropic diffusion provides efficient noise reduction along with edge enhancement which improves the image segmentation and establishment of boundaries between bone and scaffold remains. The following equation can be used to describe the temporal evolution of an image $I = I(x,t)$ that is subjected to anisotropic diffusion:

$$I_t = \mathrm{div}(G \cdot \nabla I) \tag{2.1}$$

Where I_t denotes the derivative of the image I with respect to the processing time $t, \nabla$is the gradient related to the coordinate vector x(dim(N, 1), N equals the dimension of the image space which could be 2 or 3) , and G is a square matrix (dim(N, N)) called diffusivity. Substituting for constant $G = g$, the equation can be rewritten as follows:

$$I_t = g \triangle I \tag{2.2}$$

The solution of the previous equation is a Gaussian function of standard deviation equals $\sigma = \sqrt{2gt}$. The solution of this equation results in Gaussian filtering of the image and blurring both noise and edges [Frangakis and Hegerl, 2001; Perona and Malik, 1990].

Replacing the constant g with monotonically decreasing function $g(|\nabla I|)$ was proposed by Perona and Malik [Frangakis and Hegerl, 2001; Perona and Malik, 1990], in order to achieve noise reduction with edge enhancement.

$$I_t = div(g(|\nabla I|)\nabla I) \quad \text{where} \quad g(|\nabla I|) = \frac{1}{1+\frac{|\nabla I|^2}{k^2}} \tag{2.3}$$

The diffusivity matrix can be structured as follows

$$G = \begin{bmatrix} v_1 & v_1 & v_3 \end{bmatrix} \cdot \begin{bmatrix} \lambda_1 & 0 & 0 \\ 0 & \lambda_2 & 0 \\ 0 & 0 & \lambda_3 \end{bmatrix} \cdot \begin{bmatrix} v_1 & v_1 & v_3 \end{bmatrix}^T \tag{2.4}$$

Where vi are the eigenvectors of the structure tensor $J_0 = \nabla I \cdot |\nabla I|^T$. It can also be the eigenvectors of the average version of the structured tensor $J_\sigma = J_0 \cdot K_\sigma$ where K_σ is a Gaussian function of width σ. The local structural features of the image I within a neighborhood of size $O(\sigma)$, can be characterized with the above equation along with the eigenvalues μ_i which reflects the gray level variance of in the direction of the eigenvector.

Edge enhancing diffusion (EED) version of anisotropic diffusion filtering is based on the directional information of the eigenvectors of the nonaveraged structure tensor J_0 where $(\sigma = 0)$ and the relations $v_1 = \nabla I/|\nabla I|$ *and* $\mu_1 = |\nabla I|^2$ with all other eigenvalues held to zero. Consequently the parameters λ_i are chosen according to Perona and Malik model [Frangakis and Hegerl, 2001; Perona and Malik, 1990] where

$$\lambda_1 = \lambda_2 = g(\mu_1) \; and \; \lambda_3 = 1 \tag{2.5}$$

Perona and Malik also proposed a discrete model for the continuous one [Perona and Malik, 1990]. The structure of the discrete model is shown in figure 2.1.

$$I_{(i,j)}^{t+1} = I_{(i,j)}^t + \lambda [c_N \cdot D_N I + c_S \cdot D_S I + c_E \cdot D_E I + c_W \cdot D_W I]_{(i,j)}^t \tag{2.6}$$

$$D_N I_{(i,j)} = I_{(i-1,j)} - I_{(i,j)} \tag{2.7}$$

$$D_E I_{(i,j)} = I_{(i,j+1)} - I_{(i,j)} \tag{2.8}$$

$$D_W I_{(i,j)} = I_{(i,j-1)} - I_{(i,j)} \tag{2.9}$$

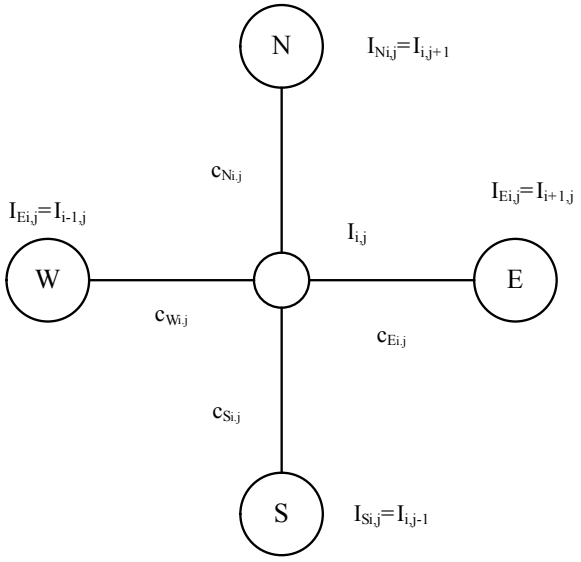

Figure 2.1 Structure of the discrete computational scheme [Perona and Malik, 1990]

With updating the conduction coefficients every iteration as follows

$$c^t_{N_{i,j}} = g(\|(\nabla I)^t_{(i+1/2,j)}\|) \tag{2.10}$$
$$c^t_{S_{i,j}} = g(\|(\nabla I)^t_{(i-1/2,j)}\|) \tag{2.11}$$
$$c^t_{E_{i,j}} = g(\|(\nabla I)^t_{(i,j+1/2)}\|) \tag{2.12}$$
$$c^t_{W_{i,j}} = g(\|(\nabla I)^t_{(i,j-1/2)}\|) \tag{2.13}$$

Where N, S, E and W represents the north, south, east and west pixels of the pixel (i,j) considering that $0 \leq \lambda \leq 0.25$ for the stability of the numerical scheme.

The norm gradient can be approximated.

$$c^t_{N_{i,j}} = g(|D_N I^t_{i,j}|) \tag{2.14}$$
$$c^t_{S_{i,j}} = g(|D_S I^t_{i,j}|) \tag{2.15}$$
$$c^t_{E_{i,j}} = g(|D_E I^t_{i,j}|) \tag{2.16}$$
$$c^t_{W_{i,j}} = g(|D_W I^t_{i,j}|) \tag{2.17}$$

Function $g(\cdot)$can be chosen from different functions of similar results such as $g_1(|\nabla I|) = 1/\left(1+\frac{|\nabla I|^2}{k^2}\right)$ or $g_2(|\nabla I|) = e^{-(\|\nabla I/K\|)^2}$. Both functions are plotted versus the gradient value with K=50 in figure 2.2. The function $g_2(|\nabla I|)$is more sensitive to gradient values and results in more enhanced edges.

2.7.2 Image segmentation methods

The accurate segmentation of the phases in the mCT scans of the explanted bone substitute biopsies is crucial for the accuracy of the characterization of the biological processes. Many studies have been conducted to develop and validate segmentation techniques for mCT. Some of these techniques were based on statistical methods, region-based segmentation and deformable models. The following two subsections include review of the common methods for image segmentation and techniques that were applied for *in vivo* mCT analysis.

Common methods for image segmentation

Image segmentation is defined as the partitioning of an image into nonoverlapping, constituent regions which are homogeneous with respect to some characteristic (such as intensity or texture) [Keller, 2008]. Specifically, the segmentation of the image dataset of an explanted biopsy of bone substitute could be defined as isolating and identifying the subset of pixels or voxels that belongs to each of the phases existing in the image dataset (e.g. histology, SEM or mCT). Image segmentation comprises multiple techniques that can be combined to together to optimize segmentation results. These techniques can be classified into the following groups: statistical methods (thresholding), region growing, morphological, Markov random field and active contours [Keller, 2008].

Thresholding is a technique using automatic method for dividing pixels into two or more groups based on the graylevel values to iteratively find the suitable value (threshold) that eventually maximizes between group variance or minimizes the within group variance [Gonzalez and Woods, 2008]. Thresholding could be classified spatially into global and adaptive [Gonzalez and Woods, 2008]. Global thresholding is used for the complete image which comprises homogenous illumination while adaptive thresholding is used for solving the problem which requires more than one threshold for separation of two phases based on the image region [Gonzalez and Woods, 2008].

Region growing comprises the utilization of manually selected seed points to identify similar intensity region based on location connectivity; such a technique is commonly used for iden-

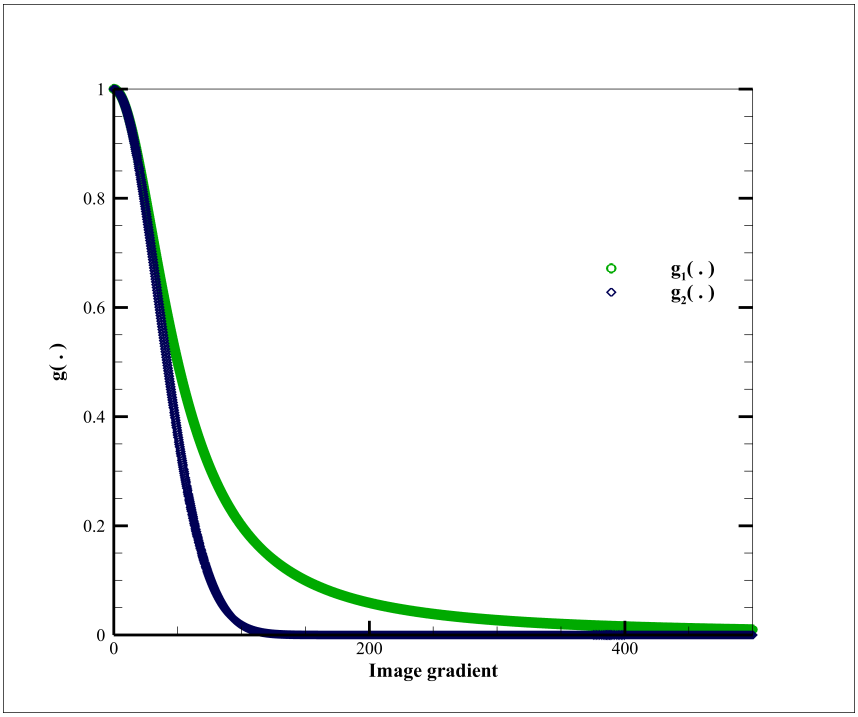

Figure 2.2 $g(\cdot)$functions versus image gradient

tifying tumors or lesions in bio-imaging applications [Keller, 2008]. This technique could be extended by region splitting and merging method [Gonzalez and Woods, 2008].

Morphological image processing visualizes image in three dimensions, two spatial dimensions x and y while the third one is the image intensity in a topographic interpretation [Gonzalez and Woods, 2008]. One of the examples of these algorithms is the Watershed algorithm which utilizes grayscale maxima and minima values to segment images [Gonzalez and Woods, 2008]. Appling watershed segmentation to bio-imaging usually requires a consecutive, often manual, stage connection regions belonging to the same structure [Keller, 2008]. Therefore, watershed segmentation algorithm is not completely automatic segmentation algorithm.

Markov random field models utilize neighbouring pixels interaction deploying Bayesian methods into image processing by treating all involved quantities as random variables [Wirjadi, 2007]. This technique often results in excessive smoothing; hence borders between different materials are blurred affecting the segmentation accuracy [Pavlovic and Metaxas, 2004]. Therefore, this technique is not suitable for segmenting *in vivo* bone scaffold because of the similarity of the graylevel values of bone and scaffold.

In conjunction with the development of computers capable of executing complex calculations, direction toward application of continuous as a replacement of discrete concepts in image processing has emerged and developed in the past two decades. The use of continuous systems like

partial differential equations systems solves the problems of algorithm accuracy and shifts this problem to the computation system capabilities of conducting numerical analysis and solution of the continuous equations i.e. the higher the computer precision the more accurate the solution results regardless of the algorithm. Deformable models or active contours have been introduced for solving image segmentation problem in 1988 [Kass *et al.*, 1988].

Deformable models or deformable contours use relaxing curves to define the closed edges of object or region [Chan and Vese, 2001; Sheppard *et al.*, 2004]. The deformable models also named active contours use converging contours that stop at the edges of the objects based on stopping criteria. The stopping criteria could be maximizing the homogenity of grey levels inside the contours or gradient based criteria [Caselles *et al.*, 2001; Chan and Vese, 2001; Kass *et al.*, 1988].

Image segmentation methods for mCT of CaP bone substitutes

One of the challenges that encounter the characterization process of the *in vivo* samples is the segmentation of soft tissue, bone and scaffolds. Several attempts have been made to segment CaP scaffolds images encountering the problem of similarity of bone and scaffold due to their attenuation similarity [Gauthier *et al.*, 2005; Hollister *et al.*, 2005; Polak *et al.*, 2012; van Lenthe *et al.*, 2007].

In biomechanics laboratory of université de Sherbrooke, a segmentation algorithm based on fuzzy distance transform (FDT) was developed and applied in characterization of β-TCP scaffolds [Bashoor-Zadeh *et al.*, 2010; Darabi *et al.*, 2007, 2009]. This method has exhibited a success in treatment of mCT images with fuzzy edges scaffolds. An improvement to the FDT segmentation algorithm was added using subvoxel processing of the mCT images [Bashoor-Zadeh *et al.*, 2011]. However, FDT segmentation is suitable for segmenting images of only two phases. Moreover, FDT segmentation requires selection of initial thresholds of the two phases being segmented based on the histogram of the images.

Segmentation of bone and CaP scaffold was done using thresholding technique in many *in vivo* studies [Gauthier *et al.*, 2005; van Lenthe *et al.*, 2007]. Global thresholding was used by Gauthier et al to segment the three phases; soft tissue, bone and ceramic [Gauthier *et al.*, 2005]. They used two thresholds to segment the three phases; soft tissue was identified to be of gray level less than 50% of the maximum gray level while gray level values of bone lie between 50 to 68% which is the minimum values of ceramic gray level. However, this method resulted in disagreement between volume fractions (soft tissue, bone and ceramic) resulted from mCT and SEM [Gauthier *et al.*, 2005]. This could be explained by the change in attenuation in both bone and material due to the mineralization and resorption process that takes place through the

healing process [von Doernberg *et al.*, 2006]. Consequently, the thresholds could not be fixed at certain values and changed over time (i.e. thresholds of two weeks explanted samples are different from ones of 4 months). In another study plain thresholding was used to segment *in vivo* explanted samples [van Lenthe *et al.*, 2007]. However, it resulted in errors especially in bone that is in direct contact to the scaffold remains and high calcified host bone and required manual refinement.

Global thresholding using Otsu's method was applied for segmentation of *in vivo* mCT of three types of scaffolds (HA, silicon stabilized tricalcium phosphate (Si-TCP) and natural bone mineral derived scaffolds) [Komlev *et al.*, 2010]. Due to the statistical nature of the method in addition to its globalization, the analysis lacked the certainty in segmenting bone and scaffold; hence the authors had to classify the image into four phases instead of three (soft tissue, bone, scaffold and uncertain regions which could be highly mineralized bone or partially resorbed ceramic).

Van der Pol et al applied the global thresholding method to *in vivo* mCT of explanted scaffolds [van der Pol *et al.*, 2010]. Micro-CT evaluation of newly formed bone in the defects showed that bone ingrowth inside the biocomposite scaffolds at 2 (BV/TV = 1.8$\pm$1.1 %), 4 months (BV/TV = 3.0$\pm$1.6 %) and 12 months (BV/TV = 22.4$\pm$12.3 %). In comparison to histomorphometrical which exhibited bone densities of 10.2 $\pm$ 3.7%, 12.6 $\pm$ 3.4% and 29.4 $\pm$ 4.8% at two, four and eight months respectively. Therefore, segmentation of mCT using global thresholding resulted in underestimation of bone volume due to the difficulty of establishing threshold between bone and scaffold [van der Pol *et al.*, 2010].

Thresholding segmentation technique of mCT was proven to lack the high accuracy in comparison to histomorphometrical analysis methods [van der Pol *et al.*, 2010]. In addition, region-based segmentation and watershed requires manual of the seed points in the case of region-based and similar regions connection in both techniques. Complete automatic segmentation algorithm was proposed by Polak et al [Polak *et al.*, 2012] for *in vivo* HA mCT images segmentation based on combination of statistical segmentation and atlas registration techniques. Despite the reasonable accuracy of this algorithm, it is adapted only for specific scaffold geometry, orthogonal rod geometry.

Active contour segmentation is regarded to be a very accurate method for porous media segmentation [Sheppard *et al.*, 2004]. They used active contours combined with watershed to segment tomographic images of porous sandstones. Their accurate results encouraged Jones and his research group to use the same method for mCT three-phase segmentation approach [Jones *et al.*, 2007]. Active contours has been demonstrated to possess high accuracy and reliability in mCT

data segmentation of bone [Demenegas *et al.*, 2011; Jones *et al.*, 2007] and soft tissues such as spleen [Aykac *et al.*, 2005].

In conclusion, active contours arise as an iterative technique that segment images based on the physical boundaries contrary to statistical-based approaches (histogram-based techniques) which does not provide the required accuracy. In addition, active contour exhibits low noise sensitivity which is an important feature for the segmentation algorithm to be used for mCT segmentation [Chan and Vese, 2001]. Moreover, Chan-Vese active contour has been shown to solve the problem of faded edges [Chan and Vese, 2001]. Therefore, we propose to use Chan-Vese active contour segmentation since it provides local segmentation as well as a solution to the problem of fuzzy edges identification of soft tissue-bone-scaffold interfaces.

Table 2.1 Summarized comparison between common segmentation methods applied to mCT images

Segmentation method	**Advantages**	**Limitations**
Statistical segmentation methods (i.e. Otsu's global segmentation)	• Easy • Fast	• Global segmentation • Sensitive to image histogram (required valleys between materials in histogram)
Edge detection segmentation (Sobel, Canny … etc.)	• Local segmentation • Fast	• Sensitive to noise • Failure with fuzzy edges
Region growing segmentation	• Local segmentation • Choice of different criteria	• Initial seeds required • Post-segmentation region merging is required • Sensitive to image gradient
FDT methods	• Fuzzy edges treatment • Accurate • Combines spatial and statistical methods	• Not suitable for more than two phases • Requires manual selection of thresholds. • Computationally invasive
Classical active contours	• Low sensitivity to noise • Object based segmentation	• Gradient based stopping criterion. • Failure with fuzzy edges.
Energy-based active contours	• Very low sensitivity to noise • Local segmentation • Insensitive to image gradient • Insensitive to image histogram	• Accuracy is dependent of computational effort

2.7.3 Active contours

The requirement of local segmentation algorithm such as active contours arises from the difficulty to use methods based on histogram such as fuzzy distance transform (FDT). The FDT requirement of choice of two thresholds cannot be fulfilled because of the overlap between bone and scaffold gray levels.

In conjunction with the development of computers capable of executing complex calculations, direction toward application of continuous as a replacement of discrete concepts in Image pro-

cessing has emerged and developed in the past two decades. The use of continuous systems like partial differential equations systems solves the problems of algorithm accuracy and shifts this problem to the computation system capabilities of conducting numerical analysis and solution of the continuous equations i.e. the higher the computer precision the more accurate the solution results regardless of the algorithm. Active contours has been introduced for solving image segmentation problem in 1988 [Kass *et al.*, 1988].

Active contour segmentation is regarded to be a very accurate method for porous media segmentation [Sheppard *et al.*, 2004]. Sheppard et al [Sheppard *et al.*, 2004], used active contours combined with watershed to segment tomographic images of porous sandstones. Their accurate results encouraged Jones and his research group to use the same method for μCT three-phase segmentation approach [Jones *et al.*, 2007]. Active contours has been demonstrated to posses high accuracy and reliability in mCT data segmentation of bone [Demenegas *et al.*, 2011; Jones *et al.*, 2007] and soft tissues such as spleen [Aykac *et al.*, 2005]. Also, active contour has been shown to have low noise sensitivity which is an important feature for the segmentation algorithm to be used for mCT segmentation [Chan and Vese, 2001; Jones *et al.*, 2007; Sheppard *et al.*, 2004]. Moreover, Chan-Vese active contour has been shown to solve the problem of faded edges [Chan and Vese, 2001]. Therefore, I used Chan-Vese active contour segmentation which provides local segmentation in addition to solution of the problem of fuzzy edges between bone and scaffold and between bone and soft tissue.

Chan and Vese described a model for active contours based on the energy of the object [Chan and Vese, 2001]. Unlike classical snakes and active contour models which rely on edge-function depending on the image gradient to stop the curve evolution, energy-based active contour model relies on minimization of the energy function. Such a method can overcome the shortcomings of the other models resulting from the discrete gradients being bounded and consequently the stopping function is never equal to zero at the edges in practice [Chan and Vese, 2001].

The energy-based model described by Chan and Vese was based on minimization of the following energy function to stop the curve evolution [Chan and Vese, 2001]. Assume an image u_0 is formed of two phases then the fitting term can be described by the following equation.

$$F_1(C) + F_2(C) = \int\limits_{inside} |u_0(x,y) - c_1| dxdy + \int\limits_{outside} |u_0(x,y) - c_2| dxdy \tag{2.18}$$

Where C is the variable curve and c1, c2 denotes the average energy inside and outside the curve respectively.

The boundaries of an object is a minimizer of $F_1(C) + F_2(C)$

$$inf_C\{F_1(C) + F_2(C)\} \approx 0 \approx F_1(C_0) + F_2(C_0) \tag{2.19}$$

The curve position can take one of the following positions as shown in figure 2.3;

- Completely outside the object then $F_1(C) > 0, F_2(C) \approx 0$,
- Completely inside the object then $F_1(C) \approx 0, F_2(C) > 0$,
- Both outside and inside the object then $F_1(C) > 0, F_2(C) > 0$,
- The curve fits to the object boundaries then $F_1(C) \approx 0, F_2(C) \approx 0$.

This can be easily verified that if the curve C is outside the object, then $F_1(C) \approx 0$ but $F_2(C) > 0$. If the curve C is inside the object, then $F_1(C) > 0$ but $F_2(C) \approx 0$. Finally, the fitting energy will be minimized if the curve C is on the boundary of the object. These remarks are illustrated in Fig. 1.

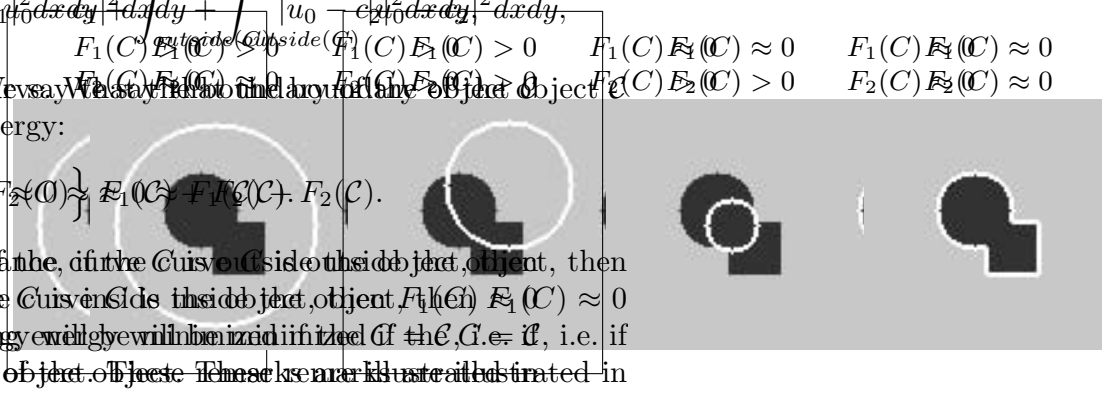

(a) (b)

Fig. 1. Consider all possible cases in the position of the curve. The "fitting energy" is minimized only for the case when the curve is on the boundary of the object.

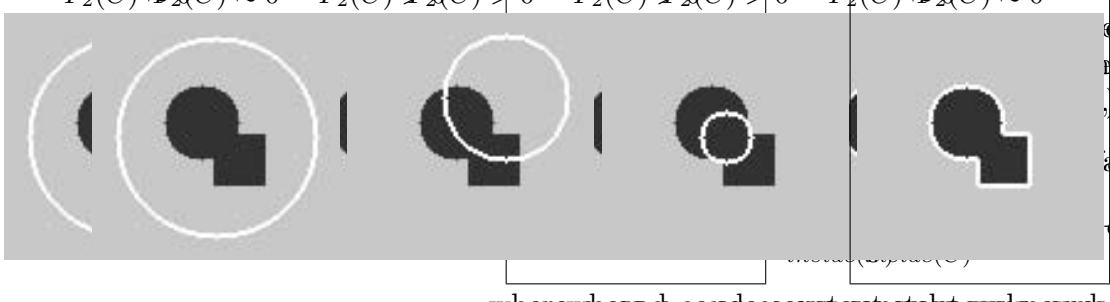

Figure 2.3 Illustration of different curve positions [Chan and Vese, 2001]

Therefore, in our active contour model we will minimize this fitting energy and we add some regularizing terms, like the length of C and/or the area inside C. We define the energy $F(c_1, c_2, C)$ by:

$$F(c_1, c_2, C) = \mu \cdot Length(C) + \nu \cdot Area(insideC) + \lambda_1 \int_{inside(C)} |u_0 - c_1|^2 dxdy + \lambda_2 \int_{outside(C)} |u_0 - c_2|^2 dxdy,$$

where c_1 and c_2 are constants unknown, and $\mu \geq 0, \nu \geq 0, \lambda_1, \lambda_2$ are fixed fix

λ_1 and λ_2. One of these th

be used for instance when we have to force the curve to move only inside

In order to calculate the constant c_1 and c_2 we assume that u_0 is a measure of size $h \times h$ of u_0

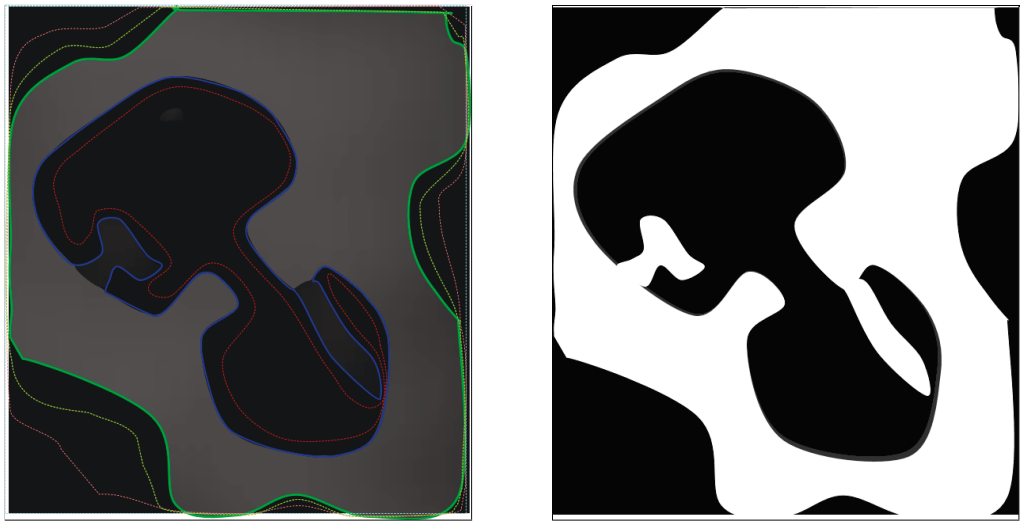

(a) (b)

Figure 2.4 An illustration of active contours convergence on a schematic of post-implantation mCT of β-TCP scaffold (a) illustration of convergence steps (b) final segmentation

By adding the regularizing terms to the fitting terms, the energy functional can be defined by

$$F(C,c_1,c_2) = \mu_0 \cdot Length(C) + \nu_0 \cdot Area(C) + \lambda_1 \int_{inside} u_0(x,y) - c_1|^2 dxdy + \lambda_2 \int_{outside} |u_0(x,y) - c_2|^2 dxdy \tag{2.20}$$

Where $\mu, \nu, \lambda_1, \lambda_2$ are fixed and $\mu, \nu \geq 0, \lambda_1, \lambda_2 > 0$. In most of the numerical implementations $\lambda_1 = \lambda_2 = 1$ and $\nu = 0$ [Chan and Vese, 2001]. Hence, the minimization problem approaches

$$inf_{(C,c_1,c_2)}\{F(C,c_1,c_2)\} \tag{2.21}$$

Lately, Mathworks included implementation of energy-based active contour model [Chan and Vese, 2001] in the Matlab image processing toolbox. A schematic illustration of the convergence of active contour to segment one phase in mCT is shown in figure 2.4. Figure 2.4(a) shows a schematic of contour convergence steps to segment the darkest phase, which represents the soft tissue in the real in vivo mCT data of bone substitutes. Following the convergence of the contour, the phases were separated as shown in figure 2.4(b), where the black represents the soft tissue and the white represents the other phases (i.e. bone and ceramic remnants combined).

2.7.4 Image registration methods

Three dimensional alignment and registration of mCT of CaP bone substitutes

The localization of resorption is used for characterizing local interactions between bone deposition and scaffold characterization and help achieving more accurate segmentation of post-implantation mCT data. Such an objective requires aligning pre- and post-implantation mCT structures of CaP scaffolds. Three dimensional image alignment and registration methods could be classified into two classes: (1) feature-based image registration, and (2) image correlation methods. Whereas feature-based image registration uses geometrical or grey level features in two datasets (i.e. original/pre-implantation and deformed/post-implantatio) to find the corresponding geometrical transform for the alignment [Bay *et al.*, 2008; Lowe, 2004], image correlation methods are based on minimizing a cost function (e.g. correlation coefficient, sum of square difference, etc) [Komlev *et al.*, 2010; Polak *et al.*, 2011]. The application of 3D-3D image alignment and registration of pre- and post-implantation mCT is not extensively applied.

Komlev et al. [Komlev *et al.*, 2010] used a volume registration method, based on 3D correlation and affine linear registration, to align the pre- and post-implantation Si-TCP scaffolds. However, their technique was computationally demanding to be applied to a complete 3D mCT dataset, hence they demonstrated its use only using parts of the scaffold not a complete one. Moreover, they applied it to Si-TCP material which exhibits low resorption, meaning that the pre-implantation scaffold geometry was not largely changed [van Lenthe *et al.*, 2007; von Doernberg *et al.*, 2006]. Polak et al. [Polak *et al.*, 2011] used the knowledge of the geometrical design of HA scaffolds (i.e. orthogonal rods geometry) to localize their boundaries in post-implantation mCT scans to refine the segmentation. Even though beneficial for accurate segmentation, aligning the pre- and post-implantation of geometrically non-uniform and resorbing β-TCP scaffolds poses a great challenge, among other for the lack of efficient and accurate techniques for the coupling of the alignment and the accurate segmentation.

Inter-modal (2D-3D) image registration

Compared to the rigid registration algorithms, where the object geometry does not change, the 2D-3D registration is less developed as it required further mathematical treatment to adjust the object geometry, slightly distorted by the used imaging modalities [Osechinskiy and Kruggel, 2011; Stalder *et al.*, 2014]. Series of 2D histological sections were registered to 3D datasets using 3D-3D registration methods in order to avoid the difficulties encountering the use of 2D-3D registration [Krauth *et al.*, 2010; Song *et al.*, 2013]. Sarve et al. [Sarve *et al.*, 2008] found that normalized mutual information Chamfer matching is more accurate and robust than simulated annealing for 2D-3D rigid registration to find the metallic implant boundaries in bone. The method is based on minimizing the Euclidean distance between edges in histology and mCT. However, their method is computationally demanding and not applicable to temporally changeable geometries such as resorbable bone substitutes. Museyko et al. [Museyko *et al.*, 2015] used

image correlation to achieve 2D-3D affine registration of histology and mCT datasets of vertebral bone. Feature-based algorithm, i.e. speed-up robust features (SURF) [Bay *et al.*, 2008] and scale invariant feature transform (SIFT) algorithms [Lowe, 2004] could be used to satisfy the scale and translation invariance requirements of 2D-3D inter-modal registration between histology and mCT [Stalder *et al.*, 2014]. Stalder et al. [Stalder *et al.*, 2014] succeeded to develop a method based on SIFT algorithm to match the features between TBH histology section of bone substitutes and post-implantation SR-mCT. However, their method applies to 2D-3D registration of histology section from the same sample of the mCT dataset at the same time point. Until now, there is no algorithm to achieve 2D-3D registration of histology to pre-implantation mCT of highly resorbable β-TCP bone substitutes.

Speed-up robust features (SURF) detection and description

SURF feature detection method was designed and implemented to be a computationally efficient local feature detector and descriptor. It was proposed as a faster alternative to SIFT [Bay *et al.*, 2008; Lowe, 2004] by replacing SIFT's Difference of Gaussian operator by Fast-Hessian detector for features detection, which is five times faster. The SURF algorithm combines Hessian-Laplace region detector and gradient orientation based feature descriptor to detect blob-like structures in images [Bay *et al.*, 2008], which makes it an efficient and proper choice to detect the features in bone scaffolds of interconnected spheres structure, as the β-TCP scaffolds of interest. Specifically, the blob response in the image at location (X,Y) is approximated by the determinant of the Hessian matrix (Eq. 2.22) [Bay *et al.*, 2008]. The image is scanned by filters of different size (each represents a different scale), where interest points (centers of blob-like features) are detected at different scales. Each feature is defined by its center (the coordinates at which the the determinant of the approximated Hessian is maximum) and described by the scale at which it was detected and the value of the determinant of the approximated Hessian (strength of the feature). Schematics of the 3D mCT stacks and slices of resorbable CaP scaffolds are shown in figure 2.5. An example of detection of SURF features in schematic or pre-implantation and post-implantation resorbable bone substitutes is shown in figure 2.6, where locations and strengths of features are represented by the circles centers and radii, respectively.

$$\det(H_{approx}) = D_{xx}D_{yy} - (wD_{xy})^2 \tag{2.22}$$

Where D_{xx}, D_{yy} and D_{xy} are approximations of Gaussian second order derivative in x-, y- and xy-direction, respectively. The weight w is used to balance the approximated values to the real ones.

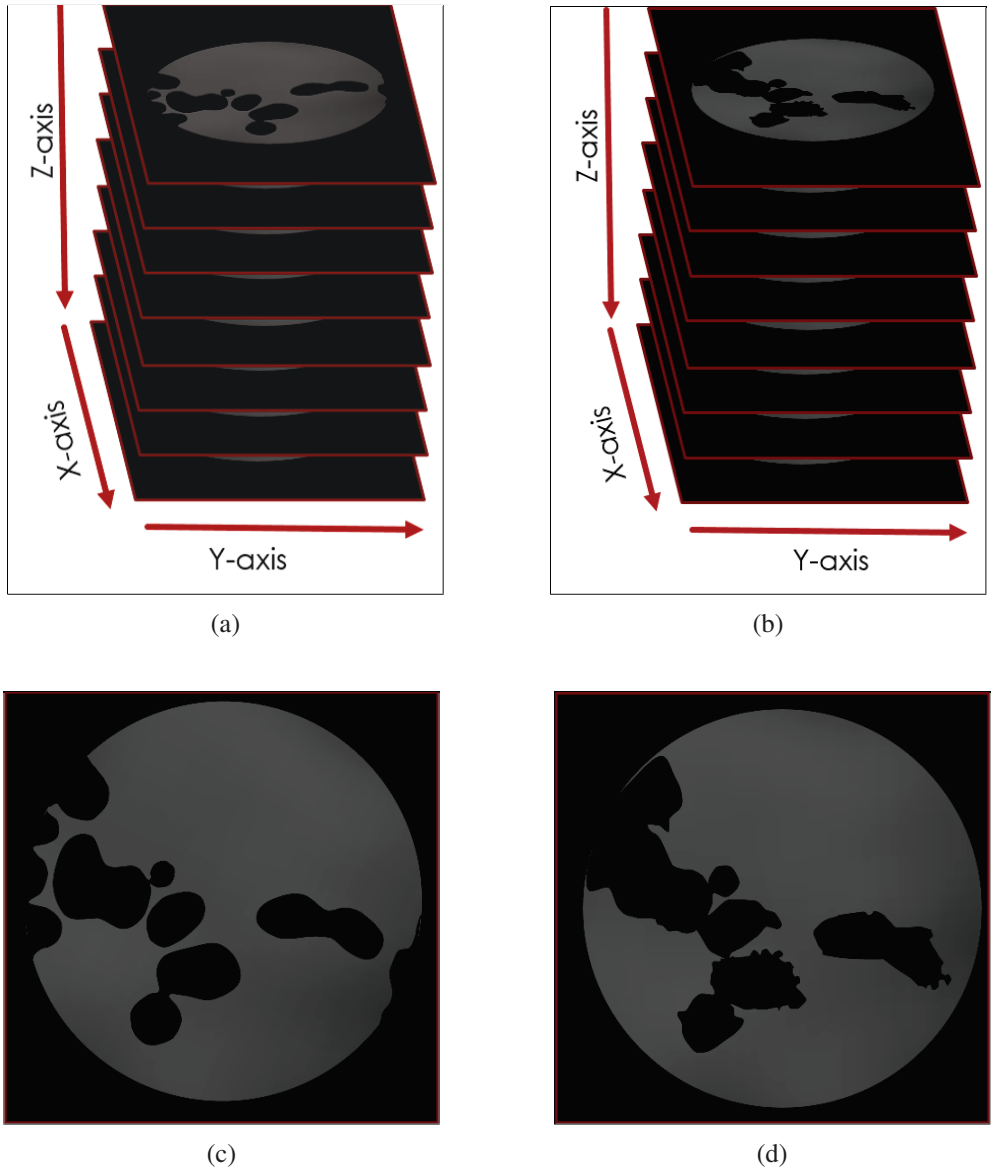

Figure 2.5 A schematic example of pre- and post-implantation mCT datasets of resorbable CaP scaffold: (a) pre-implantation 3D mCT dataset; (b) post-implantation 3D mCT dataset; (c) pre-implantation 2D mCT slice; and (d) post-implantation 2D mCT slice.

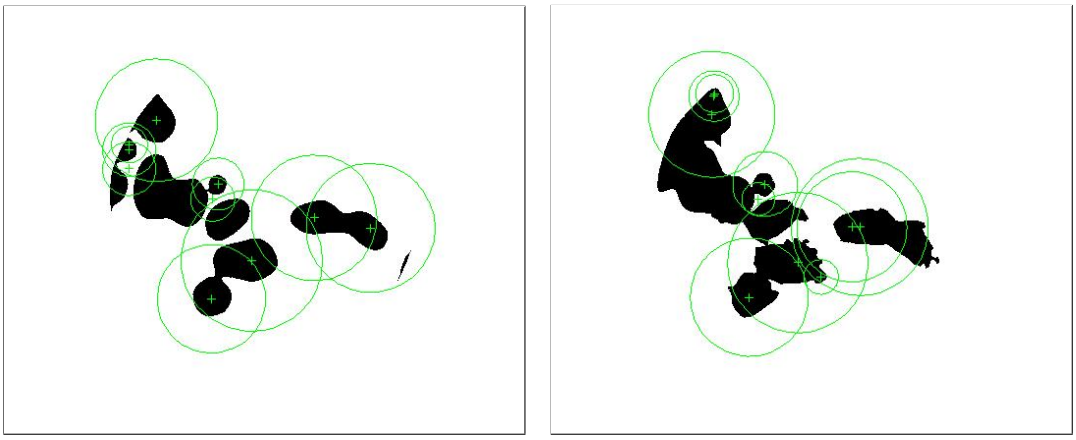

(a) (b)

Figure 2.6 An example of SURF features detection for schematic of: (a) pre-implantation; and (b) post-implantation mCT section of β-TCP bone substitutes

2.7.5 Morphometrical characterization parameters and methods

Volume fraction has been used as the characterization measure in many studies [Feng *et al.*, 2012; Gauthier *et al.*, 2005; Komlev *et al.*, 2010; Lu *et al.*, 1998; Papadimitropoulos *et al.*, 2007; Polak *et al.*, 2011; van der Pol *et al.*, 2010; von Doernberg *et al.*, 2006]. It has been used as a measure for bone deposition, scaffold remains and soft tissues in order to assess the healing process. Volume fraction and surface fraction measures were used to assess the healing time of the defect [Gaasbeek *et al.*, 2005; Podaropoulos *et al.*, 2009; Polak *et al.*, 2011; van der Pol *et al.*, 2010]. However, other measures are required to accurately assess the healing process such as bone thickness, connectivity to host bone and deposition patterns. Such measures are required to accurately insure the complete healing and integrity with host bone to avoid recurrence of fraction.

Volume and surface area fraction characterization

The measurement of volume fraction is the statistical process of calculating the ratio of voxels of a specific material within a specific volume. It has been used to evaluate bone density for diagnosing diseases such as osteoporosis as bone mineral density measurement is not sufficient for understanding bone loss; hence, it is also required to study the bone volume [Waarsing *et al.*, 2004]. Many studies utilized volume fractions (i.e. bone, scaffold and soft tissue volume fractions) for assessment of *in vivo* samples [Feng *et al.*, 2012; Gauthier *et al.*, 2005; Komlev *et al.*, 2010; Lu *et al.*, 1998; Papadimitropoulos *et al.*, 2007; Polak *et al.*, 2011; van der Pol *et al.*, 2010; von Doernberg *et al.*, 2006]. Moreover, volume fraction was used to characterize scaffold to measure porosity [Bashoor-Zadeh *et al.*, 2010]. In our lab, the effect of subvoxelization on

obtaining more accurate volume fraction calculation was investigated and calculation algorithm was developed and used to characterize ceramic scaffolds [Bashoor-Zadeh *et al.*, 2011].

Thickness characterization

Thickness is one of the important parameters to characterize the bone deposition as it can be used to compare newly deposited bone to host bone in order to assess the healing process and time. Moreover, thickness of bone could be used to evaluate the mechanical properties of the deposited bone and scaffold to test the ability of the defect repair to match the mechanical properties of the host bone [van Lenthe *et al.*, 2007]. Thickness measurement using mCT was used to characterize the scaffold resorption as well as bone deposition and relation between them [Komlev *et al.*, 2006]. An implementation of 2D and 3D Hildebrand's local thickness calculation was presented as a plugin for ImageJ software and was used for characterizing *in vivo* bone substitutes [Hildebrand and Rüegsegger, 1997; Komlev *et al.*, 2006]. In this method, the local thickness at a given point in the structure was defined as the diameter of the largest sphere that includes the point and which can be fitted completely inside the structure [Hildebrand and Rüegsegger, 1997].

CHAPTER 3

A NOVEL METHOD FOR SEGMENTING AND ALIGNING THE PRE- AND POST-IMPLANTATION SCAFFOLDS OF RESORBABLE CALCIUM-PHOSPHATE BONE SUBSTITUTES

A novel method for segmenting and aligning the pre- and post-implantation scaffolds of resorbable calcium-phosphate bone substitutes

Ahmed Sweedy[a], Marc Bohner[b], G. Harry van Lenthe[c], Gamal Baroud[d]

[a] PhD student, Laboratoire de Biomécanique, Faculté de Génie, Université de Sherbrooke, Sherbrooke, Qc Canada J1K 2R1

[b] Professor,RMS Foundation, Bischmattstrasse 12, CH-2544 Bettlach, Switzerland

[c] Professor,Biomechanics Section, KU Leuven - University of Leuven, Celestijnenlaan 300, 3001 Leuven, Belgium

[d] Professor, Faculté de Génie, Université de Sherbrooke, Sherbrooke, Qc Canada J1K 2R1

This chapter addresses the problems, mentioned in section 1.3, related to the use of mCT to analyze high resorbable CaP bone substitutes. It presents a development and implementation of a new method, which comprises new developed algorithms, to achieve the first general objective of this project (section 1.4).

3.1 Abstract

Micro-computed tomography (mCT) is commonly used to characterize the three-dimensional architecture of porous ceramic bone graft substitutes before and after implantation in order to assess changes occurring during implantation. The mCT datasets of explanted ceramic bone substitutes pose significant challenges to process because of the grey values overlap of ceramic, bone, and soft tissue and because of the post-implantation resorption of the bone substitute. This article introduces and rigorously validates a new processing technique to accurately distinguish these three phases. The mCT datasets obtained before and after implantation of macroporous β-tricalcium phosphate (β-TCP) scaffolds were aligned in 3D, and the characteristic grey value distributions of the three phases were extracted, hence allowing for an accurate differentiation between ceramic, bone, and soft tissue. Using the Dice similarity coefficient, a $94 \pm 1\%$ agreement was found between calculated and visual assessment of 556800 pixels. This new technique could lead to a more common use of mCT in analyzing the complex 3D processes and to a better understanding of biological processes occurring after the implantation of ceramic bone graft substitutes.

3.2 Introduction

Bone substitutes made of synthetic materials are a viable alternative to autografts and allografts (Marc Bohner, 2010; Jahangir, Nunley, Mehta, & Sharan, 2008). Among these, calcium phosphates (CaP) are particularly interesting due to their chemical and physical similarity to bone minerals (Barrère, van Blitterswijk, & de Groot, 2006; LeGeros, 2008). Next to their biocompatibility, CaP bone graft substitutes exhibit other desirable properties, including bioactivity and osteoconductivity (LeGeros, 2008; Podaropoulos, Veis, Papadimitriou, Alexandridis, & Kalyvas, 2009; Scaglione et al., 2012; van der Pol et al., 2010; von Doernberg et al., 2006). The CaP materials, such as hydroxyapatite (HA) or tricalcium phosphate (TCP), are routinely used for filling traumatic and pathological bone defects (Gaasbeek, Toonen, Heerwaarden, & Buma, 2005; Wang et al., 2013; Zerbo, Bronckers, Lange, & Burger, 2005). Compared to HA, the β-TCP material are gradually resorbed and replaced by neo-bone (Draenert, Draenert, & Draenert, 2013; Lu et al., 1998). However, the quest for the optimum substitute design, in terms of material and porous geometry, and for controlled interactions with the host bone continues (M Bohner, Loosli, Baroud, & Lacroix, 2011; Feng et al., 2012). Animal studies played thus far a significant role in this quest (Lan Levengood et al., 2010; Lapczyna et al., 2014; Mastrogiacomo et al., 2006; Maté-Sánchez de Val et al., 2013; van Lenthe et al., 2007; von Doernberg et al., 2006; Yuan, Li, De Bruijn, De Groot, & Zhang, 2000).

Characterizing the three-dimensional macro-porous bone substitutes before and after implantation requires the use of accurate techniques and methods. As such, the microcomputer tomography (mCT) is commonly employed (Bashoor-Zadeh, Baroud, & Bohner, 2010, 2011; Gauthier et al., 2005; Hollister et al., 2005; Polak, Candido, Levengood, & Wagoner Johnson, 2012; Ruegsegger, Koller, & Muller, 1996; van Lenthe et al., 2007). Compared to the post-implantation characterization (Gauthier et al., 2005; Hollister et al., 2005; Polak et al., 2012; van Lenthe et al., 2007; von Doernberg et al., 2006), the mCT technique for the pre-implantation characterization of β-TCP scaffolds witnessed a relative success (Bashoor-Zadeh et al., 2010, 2011). Methods to distinguish and isolate the three phases (bone, ceramic, soft tissue) of the explanted ceramic bone substitute samples are still lacking. Furthermore, the spatial and temporal evolution in the mineralization levels, in the form of the newly deposited bone, and of the partially localized resorption of the β-TCP implant further increase the difficulty to establish precise and accurate methods differentiating the grey levels of the three phases (Gauthier et al., 2005; van der Pol et al., 2010; van Lenthe et al., 2007; von Doernberg et al., 2006). In the commonly used global thresholding technique, two threshold values must be defined, one separating the grey levels of fibrous tissue, and bone, and the second one separating the grey levels of bone ceramic. Specifically, global thresholding techniques, e.g. the Otsu's method, were applied in several in-vivo studies to distinguish the bone from the ceramic (Gauthier et al., 2005; Hollister et al., 2005; Komlev et al., 2010; Papadimitropoulos et al., 2007; van der Pol et al., 2010; van Lenthe et al., 2007). These methods often led to inaccurate results. Gauthier et al. (Gauthier et al., 2005) reported a significant disagreement in the bone volume fraction measured from the mCT versus scanning electron microscopy. van Lenthe et al. (van Lenthe et al., 2007) reported some segmentation errors and, used as per example, dilation-based refinement, in particular for bone being in contact with the scaffold. For the inaccuracy resulting from the global thresholding, Komlev et al. (Komlev et al., 2010) classified the mCT data into four phases: bone, scaffold remnants, soft tissue and uncertain phase. The latter could be bone or partially resorbed scaffold.

Improvement with respect to isolating the different phases after implantation was recently achieved using new segmentation algorithms. Specifically, Jones et al. (Jones et al., 2007) was first to apply the contour-tracking segmentation (Kass, Witken, & Terzopouos, 1988) and the watershed algorithms to explanted HA implants, and specifically reported a more accurate segmentation compared to global thresholding. Still, they reported disagreement between the algorithmic results and visual assessment. Polak et al. (Polak et al., 2012) advantageously combined the atlas registration and statistical thresholding to distinguish bone from ceramic in the explanted samples (Polak et al., 2012), and reported accurate results. However, this algorithm only applies to scaffolds made of orthogonal rods and controlled geometry of slow-resorbing ceramic implant.

To our knowledge, an accurate method for segmenting the three phases of the in-vivo highly resorbable porous bone CaP scaffolds does not yet exist.

Aligning the pre- and post-implantation scaffolds using datasets was applied for finding the thresholding value to segment the three phases. Komlev et al. (Komlev et al., 2010) used a volume registration method, based on 3D correlation and affine linear registration, to align the pre- and post-implantation Si-TCP scaffolds. Their technique is computationally demanding for application on 3D data sets of complete samples. In addition, the Si-TCP material exhibits low resorption, which means that the pre-implantation scaffold geometry was not largely changed (van Lenthe et al., 2007; von Doernberg et al., 2006). Even though beneficial for accurate segmentation, aligning the pre- and post-implantation of geometrically non-uniform and resorbing β-TCP scaffolds poses a great challenge, among other for the lack of efficient and accurate techniques for the coupling of the alignment and the accurate segmentation.

The present manuscript has two relating objectives. The first objective was to develop and implement a segmentation method to accurately isolate the three phases present of the explanted ceramic bone substitute scaffolds, i.e. bone, ceramic, and soft tissue. For that purpose, a contour-based method combined with a compaction algorithm treating fuzzy transitions often found between phases were also used to yield more accurate results compared to current methods. The second objective was to improve the results even more by aligning pre- and post-implantation mCT, hence allowing the extraction of the grey value distribution of each phase. These distributions, once extracted, were subsequently applied to refine the contour-based segmentation method for even more accurate results. The expected results were post-implantation datasets, accurately segmented in three phases (bone, ceramic, soft tissue), and thus the study of the changes and the biological interaction becomes more accurate.

3.3 Materials and methods

3.3.1 Scaffold fabrication, in-vivo model, and mCT scanning

Pure β-TCP cylindrical scaffolds of constant porosity were fabricated using the calcium-phosphate emulsions method (M Bohner et al., 2005). Briefly, the calcium-phosphate cement paste (CPC) was mixed with paraffin oil and an emulsifier to obtain a metastable dispersion of oil droplets in the CPC paste. Once set, the oil-filled CPC was incubated at 60°C in a phosphate-buffered solution (0.15 M, pH = 7.4) for 48 hours, cleaned in petroleum ether, and sintered at 1250°C for 1 hour. The resulting blocks were lathed to obtain cylinders (ϕ = 8 mm, L = 13 mm). The samples contained 54% macroporosity (pore diameter greater than 50 μm) and 21% microporosity

(pore diameter smaller than 50 μm) (M Bohner et al., 2005). The macropores had a smooth spherical appearance, with an average size close to 1200 μm, as shown in Fig. 1d of Bohner et al (M Bohner et al., 2005). The β-TCP scaffolds was implanted in the metaphyseal or epiphyseal regions of the sheep for 6, 12 and 24 weeks (von Doernberg et al., 2006). Specifically, the scaffolds were implanted in 13-mm deep bone defects/cavities created using an 8-mm diameter drill (KaVo INTrASurg 500s, KaVo Dental AG Biberach, Germany). More details are presented in von Doernberg et al (von Doernberg et al., 2006). Only one randomly selected scaffold, explanted at the 6-week time point was used to demonstrate the utility of the novel processing method presented in this study. The animals were sacrificed, in accordance with the local ethics review procedures, and bone blocks containing the scaffold were cut for the retrieval of the β-TCP in-vivo scaffold. The β-TCP scaffolds were mCT-scanned before implantation and after retrieval using a commercial desktop mCT scanner (μCT 40, Scanco Medical AG, Bassersdorf, Switzerland) at 30-μm isotropic resolution (Bashoor-Zadeh et al., 2010, 2011; Lapczyna et al., 2014). The pre-implantation dataset underwent geometrical and morphometric analysis in recent studies (Bashoor-Zadeh et al., 2010, 2011). following the microCT scanning, the explanted scaffold was fixed in 40% ethanol, dehydrated in a series of graded ethanol baths (40-100%) and then defatted using xylene. The scaffold was then infiltrated with polymethylmethacrylate at 4°C, which was then left to polymerize at room temperature. Once polymerized, the scaffold was then sectioned perpendicular to its longitudinal axis using a precision saw (Leica SP 1600, Leica Microsystems, Nussloch, Germany). The sections were then stained with toluidine blue dye commonly used in histology staining.

3.3.2 Segmentation and alignment algorithm

The algorithm comprised three consecutive stages: (I) the initial segmentation of the explanted scaffold, (II) 3D alignment of the pre-implantation and explanted scaffolds, and (III) refined segmentation, Fig. 3.1. The initial segmentation, of stage I, provided a preliminary isolation of three phases found in the explanted scaffold (bone, ceramic and soft tissue). In stage II, the 3D alignment of the scaffold before and after implantation using the mCT dataset isolated the bone deposited in the macropores, and the ceramic remnants of the explanted scaffold. Accordingly, the characteristic grey-value distributions of the ceramic and bone became inherently available. In stage III, these characteristic distributions were used to refine the contour-based segmentation of stage I. Each stage further comprised multiple algorithmic steps.

Initial segmentation of the three phases (Stage I)

In stage I, the initial segmentation algorithm had four successive steps. In step 1, an energy-based active contour algorithm for image segmentation was used to segment/isolate the soft

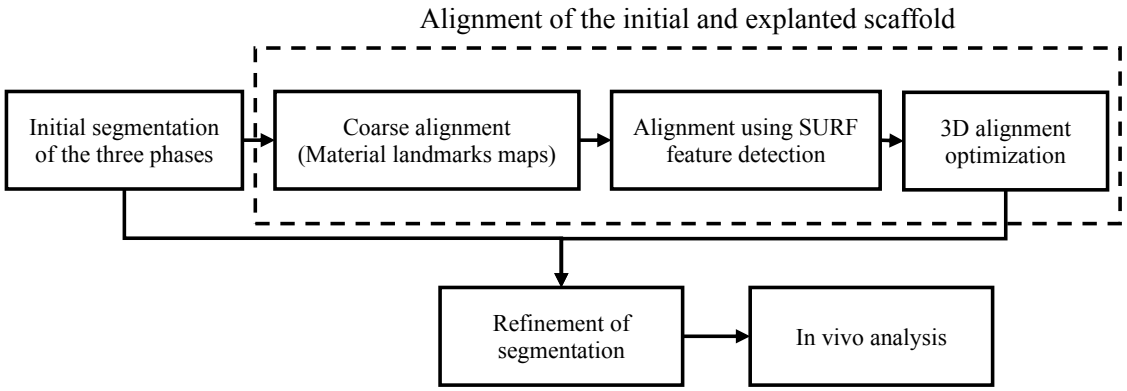

Fig. 1. Block diagram of the presented algorithm.

Figure 3.1 Block diagram of the presented algorithm

tissue of the explanted scaffold. In step 2, the fuzzy edges resulting from transitions and boundaries between phases present in the explanted scaffold were treated. Step 3 related to diffusing the bone, found in the macropores, into the background, in order to isolate the ceramic remnants. In step 4, the ceramic remnants were then segmented using active contour algorithm.

- **Segmentation of soft tissue (Step I.1)**

The mCT image stack/dataset was treated as follows to segment the soft tissue. Firstly, the Sobel edge-detection filter (Gonzalez & Woods, 2008) was used to identify strong edge pointes in the stack, which subsequently were used as seed points. Secondly, the seed points forming the mask acted as the initial contour in the step to follow. Using this initial contour, the iterative process inherent to the active contouring algorithm (Chan & Vese, 2001) identified contours gradually isolating the soft tissue by minimizing the total energy of the energy inside and outside the contour curve, $F_1(C)$ and $F_2(C)$ (Eq. 3.1), respectively. Finally, the soft tissue pixels were isolated or identified. The above-mentioned steps were repeated for each 2D image of the mCT stack.

$$F_1(C)+F_2(C)=\int\limits_{inside(C)}|I(x,y)-c_1|^2dxdy+\int\limits_{outside(C)}|I(x,y)-c_2|^2dxdy \qquad (3.1)$$

Where C is the variable curve, $I(x, y)$ is the intensity value at (x, y) and denote the average energy inside and outside the curve, respectively.

- **Treating the fuzzy transitions between phases (Step I.2)**

For refining the fuzzy transitions between phases in mCT data, two sigmoidal weight functions were used (Fig. 3.2), a distance relating (W_d) and a grey-level relating value (W_g) (Eq. 3.2). Firstly, two windows of defined number of pixels were used for identifying the transitions in

the 2D mCT images in the *x* and *y* directions. The sizes of the windows were 1*w and w*1 for x and y directions, respectively, where w was selected based on the fuzziness appearance of the transitions. In the evaluation process of transitions, a window was considered to be at the transition from one phase to another if satisfying the following conditions: (a) having at least one pixel of grey level below the threshold of a first phase (TH_1) and (b) having at least one pixel of grey level greater than threshold of second phase (TH_2). Thereafter, the pixels of the window were weighted using the distance followed by grey-level weight function. Afterwards, the windows were subjected to thresholding process.

$$W_g = A + \begin{cases} 1 & \rightarrow f(p) \geq TH_1 \\ 1 - 2(f(p) - TH_1)^2/(TH_1 - TH_2)^2 & \rightarrow TH_1 \geq f(p) \geq (TH_1 + TH_2)/2 \\ 2(f(p) - TH_2)^2/(TH_1 - TH_2)^2 & \rightarrow (TH_1 + TH_2)/2 \geq f(p) \geq TH_2 \\ 0 & \rightarrow TH_2 \geq f(p) \end{cases} \tag{3.2}$$

Where A is a weighting constant and *f(p)* is the grey value of pixel p.

- **Bone/soft tissue interface diffusion (Step I.3)**

This step began by finding the initial seeds for the purpose of diffusing the bone edges into soft tissue. The initial seeds, and more precisely the seed voxels, were identified in the interfaces of the bone and soft tissue, in addition to the ceramic/soft tissue. Using a Gaussian function (Perona & Malik, 1990), the seed voxels were then used as initial values for an iterative process to diffuse bone edges into the neighboring voxels of the soft tissue. Specifically, the bone found

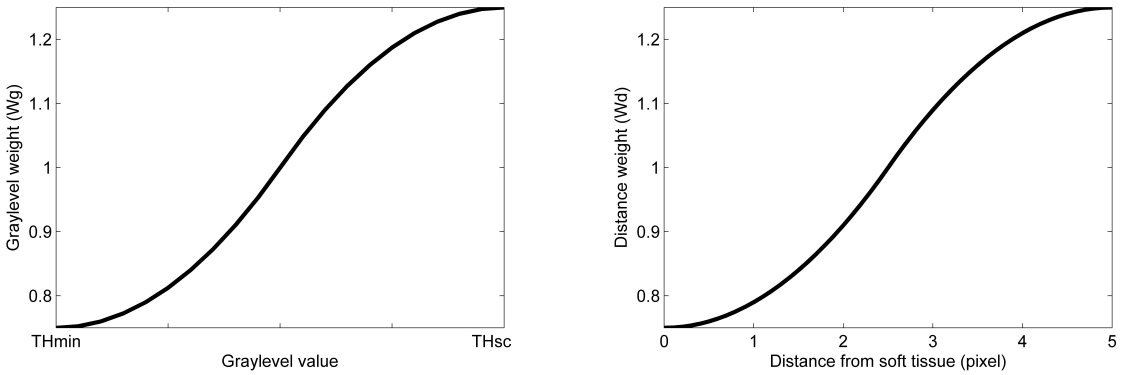

Figure 3.2 The sigmoidal weighting functions of the grey-value and distance transitions

in the macro-porous space, once diffused, within the soft, left behind the mCT having two phases (ceramic and soft tissue).

- **Segmentation of bone and scaffold remnants (Step I.4)**

Step I.4 is identical to Step I.2 used to segment the soft tissue. The initial seeds of the ceramic were found using the Sobel filter, and accordingly forming an initial contour. Using an energy-based active contour method, referred to above, the ceramic remnant pixels were iteratively isolated. Once both the ceramic phase (Step 4), following the soft tissue phase (Step 1), the remaining unidentified voxels are clearly those of the bone deposited within the macro-porous space.

3D alignment of pre- and post-implantation scaffolds (Stage II)

The 3D alignment process comprised three steps: (1) the coarse alignment, (2) machine-based alignment using feature detection, and (3) the 3D optimization for aligning the original and explanted scaffolds. The three subsequent steps aimed at finding the 3D rotation angle and displacement matrix, referred to as transform (Fig. 3.3); and aligning the scaffold before and after implantation, using the mCT datasets.

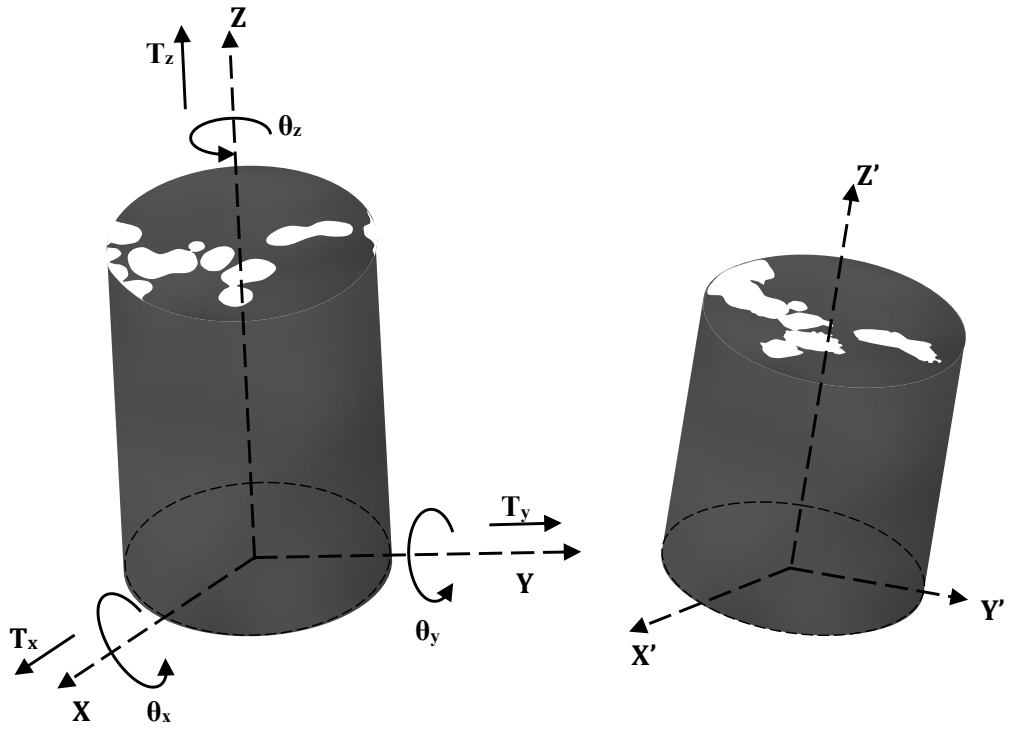

Figure 3.3 Schematic of the initial and explanted scaffold. Orthogonal coordinate systems for the 3 rotations and 3 displacements sought in the alignment process

- **Coarse alignment (Step II.1)**

In this step, the z-direction projection maps, referred to as vertical projection, of the mCT stacks of scaffold pre- and post-implantation were to used calculate the initial values the geometric transform, as follows:

I. Calculate the z-rotation angle using the volume fraction/projection maps. Once these maps or vertical projection were created as described below, common recognizable features/landmarks in the scaffold before and after implantation became visible.

1. Add the scaffold's volume fractions in the z direction of the pre-implantation mCT stack;
2. Add the scaffold's volume fractions in the z direction of the post-implantation mCT stack;
3. Find visually the common and recognizable landmarks in the volume fraction maps/projections;
4. Calculate the $\theta_z^{'}$ angle;
5. Accordingly rotate the pre-implantation mCT image stack;

II. Calculate the x and y rotation angles:

1. Make longitudinal sections at the center, perpendicular to the x axis of pre-implantation and post-implantation image stacks;
2. Find common recognizable landmarks within the longitudinal sections (human assisted);
3. Calculation of $\theta_x^{'}$ angle;
4. Repeat Steps II.1-3 for y direction and calculate $\theta_y^{'}$ angle;
5. Find the displacement $T_z^{'}$ in z-direction between pre- and post-implantation image stack.

This stage resulted in initial/coarse calculation of the values of rotation angles ($\theta_x^{'}$,$\theta_y^{'}$ and $\theta_z^{'}$) and $T_z^{'}$ and the displacement in z-direction.

- **Alignment using SURF feature- or landmark-based registration (Step II.2)**

Following the coarse alignment, the feature-based SURF algorithm (Bay, Ess, Tuytelaars, & Van Gool, 2008) was used to register or align the pre- and post-implantation scaffolds more accurately. Specifically, the SURF algorithm found the geometric unique landmarks/forms in both datasets. These features were matched and classified in accordance with the strongest match. A voting criterion for the matching strength was then applied to calculate the 2D geometric transform of the x-y plane. Step II.2 led to refined values of z rotation, x and y displacements, $\theta_z^{''}$, $T_x^{''}$

and $T_y^{''}$ respectively (Eq. 3.3).

$$\begin{bmatrix} x^{''} \\ y^{''} \\ 1 \end{bmatrix} = \begin{bmatrix} cos(\theta_z^{''}) & -sin(\theta_z^{''}) & T_x^{''} \\ sin(\theta_z^{''}) & cos(\theta_z^{''}) & T_x^{''} \\ 0 & 0 & 1 \end{bmatrix} \begin{bmatrix} x^{'} \\ y^{'} \\ 1 \end{bmatrix} \tag{3.3}$$

- **3D alignment optimization (Step II.3)**

The much-improved geometric transform of Step II.2 was then used, as the input 'initial vales' for the least-square final 3D alignment optimization in accordance with this procedure:

I. Initialize the 3D geometric transform with the results of Step II.2

II. Choose the rotation angle range from $\theta_x^{''} - \theta_d iff$ to $\theta_x^{''} + \theta_{diff}$, $\theta_y^{''} - \theta_{diff}$ to $\theta_y^{''} + \theta_{diff}$ and $\theta_z^{''} - \theta_{diff}$ to $\theta_z^{''} + \theta_{diff}$

III. Choose the displacement range from $T_x^{''} - T_{diff}$ to $T_x^{''} + T_{diff}$, $T_y^{''} - T_{diff}$ to $T_y^{''} + T_{diff}$ and $T_z^{''} - T_{diff}$ to $T_z^{''} + T_{diff}$

IV. Calculate the Sum of Square difference (SSD) as follows.

1. For θ_x all steps between $\theta_x^{''} - \theta_{diff}$ and $\theta_x^{''} + \theta_{diff}$ with step $\triangle\theta_x$
2. For θ_y all steps between $\theta_y^{''} - \theta_{diff}$ and $\theta_y^{''} + \theta_{diff}$ with step $\triangle\theta_y$
3. For θ_z all steps between $\theta_z^{''} - \theta_{diff}$ and $\theta_z^{''} + \theta_{diff}$ with step $\triangle\theta_z$
4. For T_x all steps between $T_x^{''} - T_{diff}$ to $T_x^{''} + T_{diff}$ with step $\triangle T_x$
5. For T_y all steps between $T_y^{''} - T_{diff}$ to $T_y^{''} + T_{diff}$ with step $\triangle T_y$
6. For T_x all steps between $T_z^{''} - T_{diff}$ to $T_z^{''} + T_{diff}$ with step $\triangle T_z$
7. $Scaffold_{pre_{trans}}$ = geometrical transformation of scaffold pre-implantation multiplied by $transform(\theta_x, \theta_y, \theta_z, T_x, T_y, T_z)$
8. Calculate the SSD

$$SSD = \sum | \, (Scaffold_{post} - Scaffold_{pre_{trans}}) \, |$$

9. Store SSD value
10. End of all loops
11. $SSD_{min} = \min(SSD)$
12. $Transform_{min} = Transform(SSD_{min})$

The geometric transform ($Transform_{min}$), which is the minimum sum square difference (SSD) between the pre- and post-implantation scaffold served the final refined segmentation (Stage III).

Refined segmentation (Stage III)

Once the alignment of pre- and post-implantation scaffold was completed, the three phases present in the explanted scaffold were isolated by comparing to the pre-implantation scaffolds. Specifically, a dense material found in the macro-porous space of the initial scaffold was identified as bone deposited in the macro-porous space. Dense material found in regions previously occupied by ceramics was identified as ceramic or scaffold remnants. Once the bone and ceramic remnants were found, the void phase left was identified as the soft tissue phase. Accordingly, characteristic histograms could be found of the three phases. These characteristic histograms were used, as described below, segment the dataset of the explanted scaffold, in particular the bone and ceramic remnants:

1. Using its characteristic histogram, the maximum grey value of bone was determined (THBmax);
2. Accordingly, uncertain regions of newly deposited bone (i.e. deposited at space occupied by ceramic in the initial scaffold) of grey value greater than THBmax were identified as scaffold;
3. Similarly, using its characteristic histogram, the minimum grey value of ceramic was determined (THCmin);
4. Revise uncertain region of scaffold (i.e. scaffold fragments at macro-porous space of the initial scaffold) of grey level less than THCmin to be bone;

3.3.3 Validation of the segmentation algorithm

The segmentation algorithm, stage I-III, was rigorously validated by comparing its results to those from a laborious manual segmentation process done by a trained image-processing scientist, referred to as operator. In addition, a histology section, which was cut and prepared from the explanted scaffold, was used as a reference for the results obtained from the present segmentation algorithm. Specifically, the histology section, surface-stained with toluidine blue, rendered the three phases (void, bone and ceramic) of the explanted scaffold visible. In addition, the cutting plane of the histology section was manually found within the 3D mCT dataset of the explanted scaffold. Therefore, a direct comparison of the histology staining results with the algorithmic segmentation results became possible. Five out of the 600 slices, which constituted a post-implantation mCT stack, were randomly selected for the purpose of validation. A slice consisted of 445,440 pixels. Specifically, because of the large number pixel to process, a

quarter mCT slice (111,360 pixels per each quarter and in total 556,800 pixels) was manually segmented by the operator and identified as one of the three phases (bone, ceramic or soft tissue). The similarity matrix was then used to qualitatively compare the algorithmic and operator-based segmentation results. In addition, the Dice similarity coefficient (DSC) (Dice, 1945) of the 3 phases, another comparative value (Eq. 3.4), was used:

$$D_p(P_{oper}, P_{alg}) = \frac{2 \mid P_{oper} \cap P_{alg} \mid}{P_{oper} + P_{alg}} \tag{3.4}$$

Where D_p is the DSC comparing operator Poper and algorithm-based Palg segmentation results of phase P, i.e. bone, scaffold or soft tissue.

3.4 Results

The results of the algorithmic segmentation of an exemplary mCT dataset (638x696x600 voxels) are shown in Fig. 3.4. A raw mCT image in the x-y plane is presented in Fig. 3.4a. The ceramic, present in the center of the image, is slightly brighter / radio-denser than host bone, surrounding the round scaffold, and than the bone formed with the scaffold. The ceramic morphology and the round pores can be still seen, at 6 weeks, in the center of the scaffold. Yet, the closer to the periphery of the scaffold, the more resorption, the more bone deposition, and the more the initial scaffold morphology changed. Fig. 3.4b shows an exemplary result for the initial segmentation, stage I, of the mCT dataset. The results of aligning the post- and pre-implantation scaffolds are shown in Fig. 3.4c and Fig. 3.4d for the feature-based (step II.2) and optimization alignment (step II.3) algorithms, respectively. The reference pre-implantation substitute morphology is shown blue. Ceramic remnants of the explanted scaffold are shown in red. Ceramic fragments are shown in brown. The SSD optimization refined the alignment, as seen from Fig. 3.4d versus Fig. 3.4c. The phases classified in Fig. 3.4f accordingly provided the characteristic grey-value histograms of both the bone and ceramic remnants (Fig. 3.6), which were then used to refine the initial segmentation (Fig. 3.4b). The initial segmentation overlapped with the aligned pre-implantation mCT is depicted in Fig. 3.4e (red = ceramics remnants, blue = initial scaffold morphology, gold = bone, soft tissue = white, black = new bone locally replacing the ceramics, brown = fragmented ceramic). Small ceramic fragments appeared integrated in bone. Ceramic fragments, found in the host bone, which is outside the defect side, were re-segmented to bone, Fig. 3.4f).

Figure 5 shows the averaged volume fraction/projection map in the z longitudinal direction of both pre- and post-implantation mCT datasets. Three landmarks, used in the rotation around z axis for the coarse alignment step, were depicted in both images. The three landmarks, form-

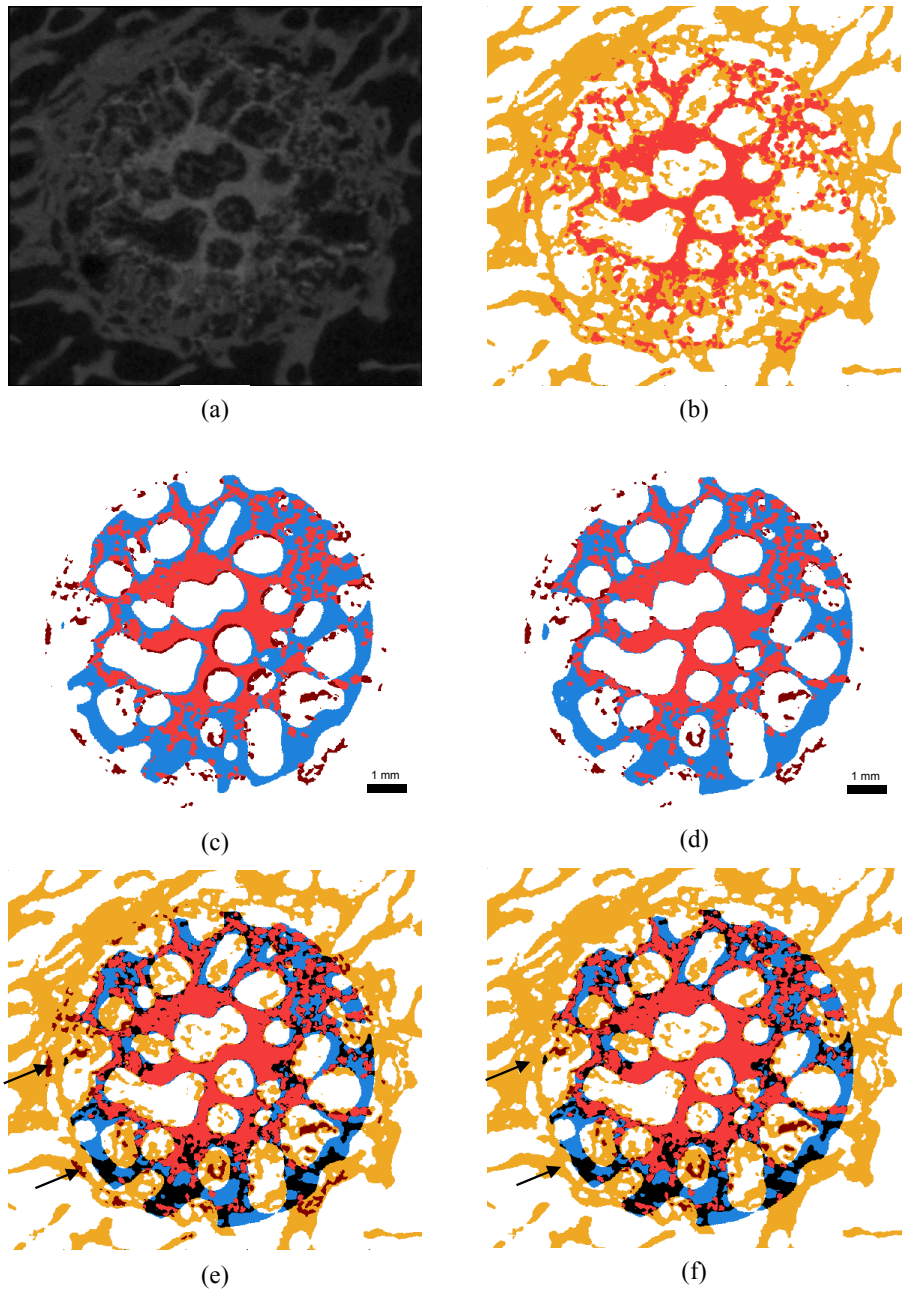

Figure 3.4 An exemplary alignment and segmentation results: (a) A mCT slice of the explanted β-TCP scaffold; (b) results of the initial segmentation; (c) alignment result from the feature-based detection (blue=initial scaffold, red=ceramic remnants). The alignment appeared out of phase; (d) the result of 3D alignment SSD-based optimization; (e) alignment-based segmentation (red=ceramic remnant, blue=initial scaffold, gold=bone, black=ceramic replaced by bone, brown=ceramic fragments apparently the host bone, as well; and (f) ceramic fragments outside the defect site were re-segmented to host bone. The arrows indicated two such ceramic fragments. The calibration bars apply to all subfigures.

ing a triangle, resulted in three rotation angles that were used for the coarse alignment. The characteristic results from the alignment process are in Fig. 3.6. The characteristic histograms of the ceramic remnants and of the neo-bone deposited in the macro-porous space are shown in Fig. 3.6a and 3.6b, respectively. The highest grey values of the ceramic remnants THCmax and of bone THBmax are 92 and 61 respectively. The post-alignment grey-value image of the defect is shown in Fig. 3.6c. In it, the bone can be distinguished from the ceramic. Using the characteristic histogram of bone and ceramic remnants, the results of the refined segmentation is shown in Fig. 3.6d.

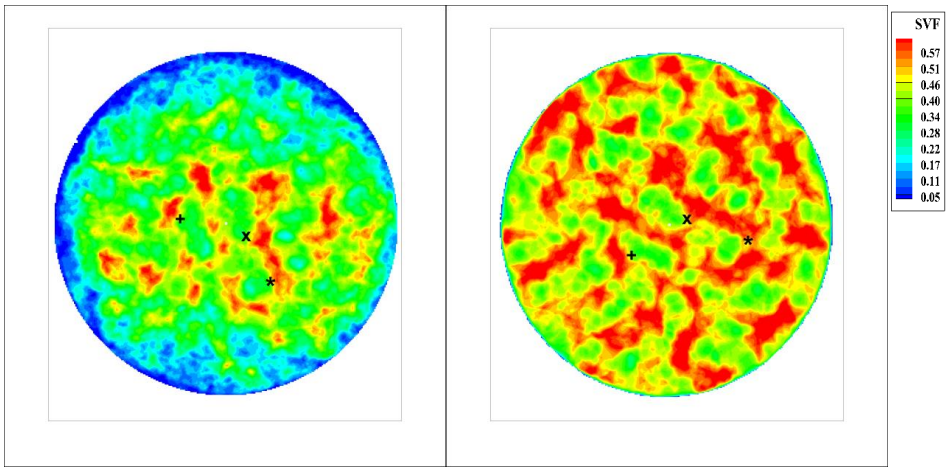

Figure 3.5 Volume fraction / z-direction projection maps of ceramic remnants of the explanted (left) and initial (right) scaffold, respectively. Thee representative landmarks common in both maps used for the course alignment.

The histology section, cut perpendicular to the longitudinal axis of the explanted scaffold and then stained, is in Fig 7a. The optical resolution of the histology section was 1.08 micron. The mCT grey-value section, corresponding with the histology section was manually found in the post-implantation dataset (Fig. 3.7b). A comparison of the segmentation results of the present new method to those in accordance to the Otsu's method are shown in Fig. 3.7c and Fig. 3.7d, respectively. The Otsu's thresholding method globally overestimated both the ceramic and bone over the soft tissue, and it overestimated the bone over the ceramic remnants. The qualitative visual comparison of the histology section and of the present segmentation rendered a relatively good agreement. For the quantitative validation, 5 mCT slices of the explanted scaffolds were randomly selected. The validation results are shown in Fig. 3.8 for an exemplary quarter of a randomly selected grey-value mCT image. The operator- versus the algorithmic-based segmentations of three phases found is in Fig. 3.8b and 3.8c, respectively. Fig. 3.8d depicted the transitions/interfaces among the three phases as detected by the operator. Both the manual seg-

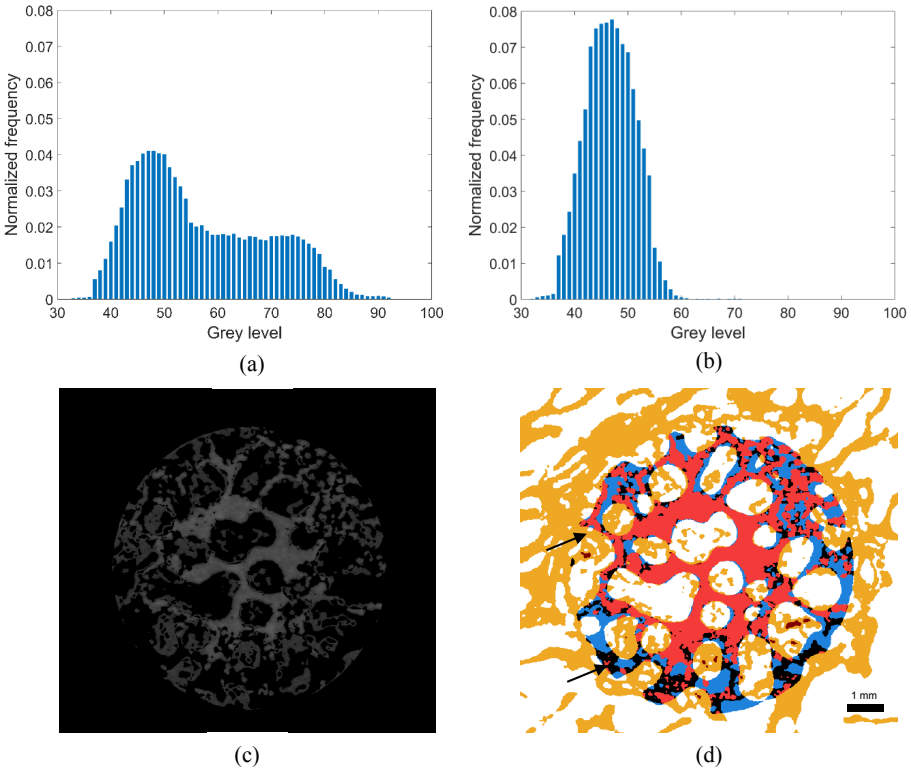

Figure 3.6 Characteristic histograms of the ceramic remnant (a) and the neo-bone found within the defect site (b), respectively. Characteristic grey-value image of the defect site (c). Refined segmentation using the characteristic histograms (d) and using the same color scheme of Fig. 3.4f. The two arrows indicated locations that were over Fig. 3.4f re-segmented to bone or ceramic fragments, respectively. The calibration bar applies to subfigures (c) and (d).

mentation and the one using the present algorithm rendered similar results. The similarity matrix of the segmentation results, of five randomly selected quarters, where the total of 556,800 pixels over five months is summarized in Table 3.1. The total similar surface fraction, which is the sum of the matrix diagonal, among the manual and algorithmic segmentation, was 94.02±0.79%. Also, Dice similarity coefficients, of the five randomly selected quarters, were 92.54±1.08%, 89.3±2.98% and 96.31±0.75% for bone, ceramic remnants and soft tissue, respectively.

3.5 Discussion

In this study, we developed, verified and validated a novel multistage algorithm for the segmentation and alignment of scaffold, of highly resorbable bone implants, before and after explanation. The algorithm comprised three stages: I) initial segmentation of post-implantation mCT data, II) alignment and registration of pre- and post-implantation scaffolds, and III) refinement of the

Table 1. Similarity matrix where BSF = bone surface/total surface, SSF=scaffold remains surface/total surface and STSF = soft tissue surface/total surface.

Table 3.1 Similarity matrix where BSF = bone surface/total surface, SSF=scaffold remnants surface/total surface and STSF = soft tissue surface/total surface.

		Algorithm-based			
		BSF (%)	SSF (%)	STSF (%)	Total
Operator-based	BSF (%)	35.49±2.80	0.97±0.27	1.88±0.35	38.33±2.38
	SSF (%)	1.43±0.25	11.77±2.79	0.14±0.09	13.34±2.89
	STSF (%)	1.42±0.91	0.15±0.18	46.76±4.16	48.33±4.30
	Total	38.34±3.08	12.89±2.53	48.78±4.31	

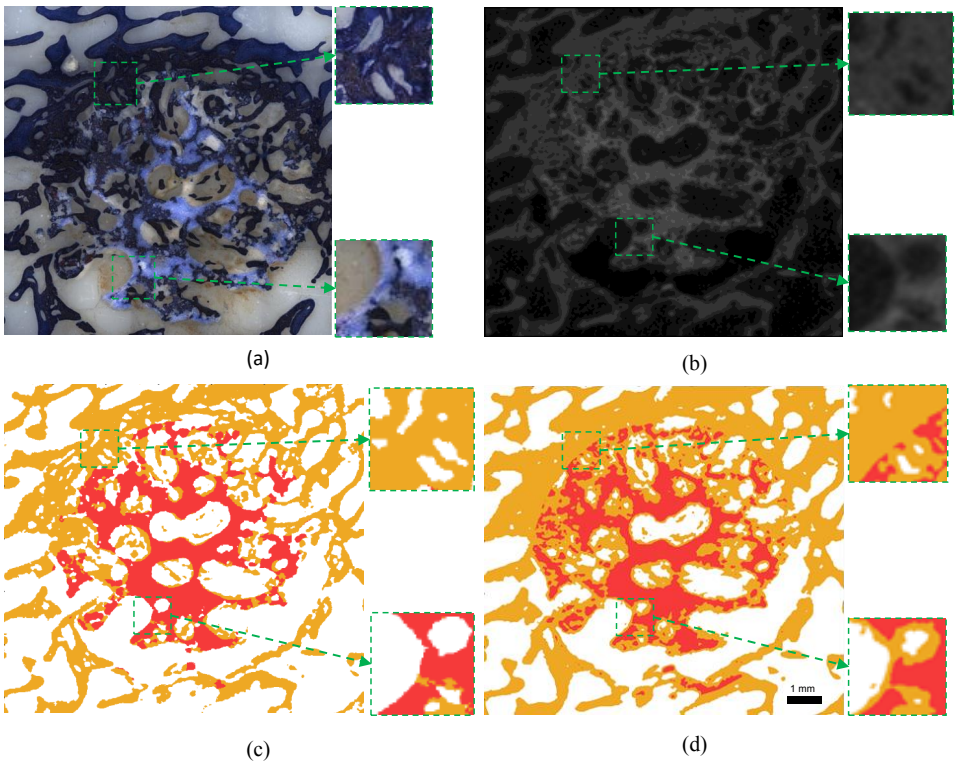

Figure 3.7 Comparing the results of the present and Otsu's method to the histology section and to the corresponding same mCT slice: (a) the histology section; (b) the mCT slice of the same histology section (c) segmentation of the present algorithm; and (d) segmentation of the Otsu's method (red=ceramic remnant, gold=bone). The calibration bar applies to subfigures (c) and (d).

segmentation using the characteristic histograms resulting from stage II. The novel algorithm was rigorously validated by comparing the algorithmic to operator-based segmentation using the Dice similarity coefficient theory (Dice, 1945). The DSC is a spatial overlap index. Specifically, the algorithmic segmentation results rendered results closely matching the histology section and manual segmentation if compared to the results of Otsu's segmentation, which is commonly

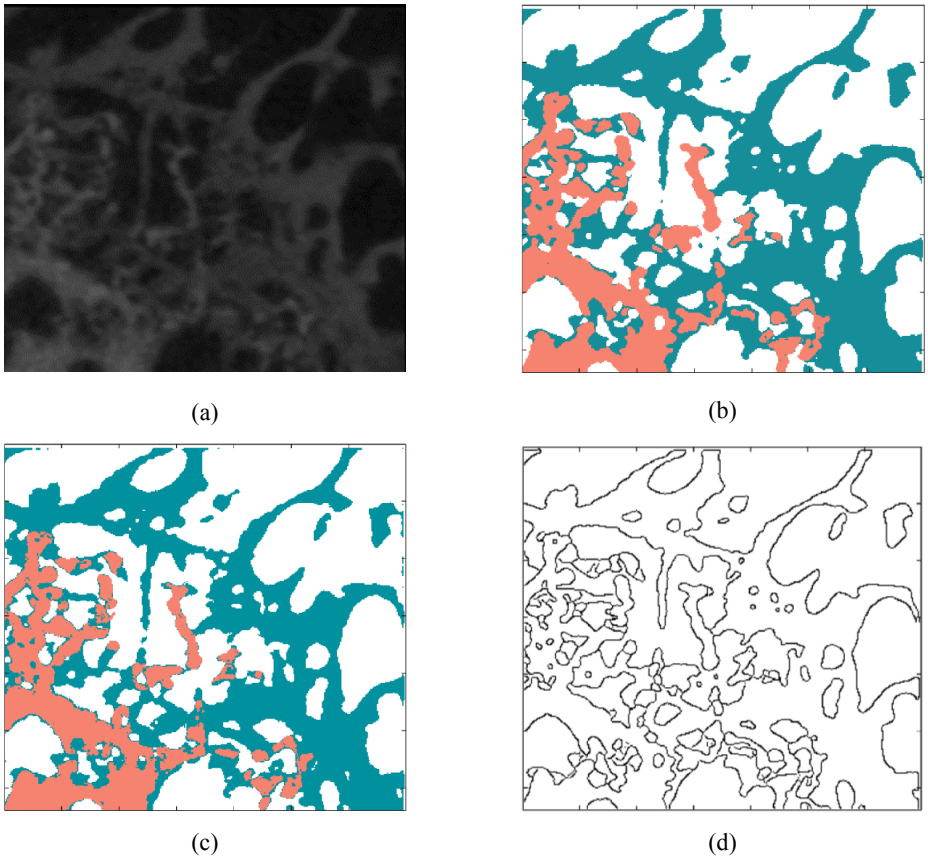

Figure 3.8 Validation results of one randomly selected quarter. (a) The gray level mCT slice; (b) the operator-based segmentation; (c) the algorithm-based segmentation; and (d) the inspected interface pixels required judgement by the operator.

used (Hollister et al., 2005; Komlev et al., 2010; Papadimitropoulos et al., 2007; Parkinson, Badiei, & Fazzalari, 2008). Unlike the presented algorithm (Fig. 3.7c), Otsu's method globally under-segmented the bone phase, in addition to the loss or merge of structural features as shown in the upper box of Fig. 3.7d. Except for the transitions/interfaces between two phases such as in the yet unremodeled center of the scaffold, Otsu's method resulted in erroneous segmentation of the interface between ceramic remnants and soft tissue (Fig. 3.7d). This was partially because of the fuzzy unclear transitions between phases in mCT data (Bashoor-Zadeh et al., 2010), and of the statistical global approach of Otsu's method (Hollister et al., 2005; Komlev et al., 2010; Otsu, 1975; Papadimitropoulos et al., 2007; Parkinson et al., 2008). Accordingly, a sigmoidal edge segmentation function and the contour-based method markedly enhanced the segmentation results (Chan & Vese, 2001; Sweedy, Bohner, van Lenthe, & Baroud, 2015; Sweedy, Jerban, Bohner, van Lenthe, & Baroud, 2015b).

A similarity matrix of 94.02±0.79% clearly indicated the agreement of the novel algorithmic and of the operator-based segmentation (Table 3.1). The DSC also showed high agreement. Although the validation had been very laborious and time consuming, it is essential for establishing confidence in the segmentation results, which will be used for evaluating the complex structures related to bone deposition and scaffold resorption.

Prior to segmentation, the mCT dataset was subject to a routine image enhancement, which included denoising (Perona & Malik, 1990) and image sharpening using unsharp mask (Gonzalez & Woods, 2008; Jones et al., 2007). For added accuracy, anisotropic denoising was preferred over the isotropic Gaussian denoising process (Sweedy, Jerban, Bohner, van Lenthe, & Baroud, 2015a; van Lenthe et al., 2007). In addition, the iterative active contouring algorithm combined with the alignment of pre- and post-implantation datasets was crucial in the accurate segmentation algorithm. Specifically, the alignment provided characteristic histogram of bone and ceramic remnants, which were otherwise not accessible. The coarse alignment, which was manually done (Fig. 3.5), resulted in calculating the initial value of the 3D geometric transform. The 2D SURF feature-based detection led to more precise geometric transform for the x-y plan, yet not sufficient because of the large resorption in explanted scaffold. The 3D SDD minimization alignment, even though computationally demanding, resulted in the accurate alignment, and consequently segmentation.

The novel algorithm is structured and systematic. As per example, the initial segmentation (stage I) was essential for the feature detection and accordingly the alignment process (stage II), which otherwise will not converge because of the vague features and different scanning parameters of the original and explanted scaffolds. The alignment further allowed isolating the scaffold remnants and the new bone in the pore space. The characteristic histograms of the new bone and scaffold remnants became inherently available, thereby the new bone deposited into regions wherein the scaffold material was resorbed was consequently distinguished, and the segmentation was further enhanced. Another advantage of the alignment, next to the higher accuracy of segmentation, is the study the newly deposited bone and the scaffold resorption, in addition to relating those to the initial architectural properties of the pre-implantation scaffold. A priori, the 3D neo-bone and regional resorption geometries became available, and this is a relevant tool, to understand the biological repair process, and its interaction with the scaffold design. The novel segmentation and alignment processes were laborious and required significant image-processing skills. Yet, they were, in our experience, applicable to other scaffold of smaller macro pores as long as sufficient features remain unchanged in the explanted scaffold. The knowledge gained of the regional resorption and bone deposition can be significant. Some blue staining was observed in the histology section within the ceramic remnant, expectedly indicating

the presence of bone tissue phase within the ceramic walls (Polak et al., 2012). Further analysis of the phases present in the ceramic walls requires details investigations and potentially new image-processing technique. This will be the focus of future research.

3.6 Conclusion

A novel technique for studying the in-vivo behavior of resorbable CaP bone substitutes using mCT data was developed. Using Dice similarity coefficients, it was validated and demonstrated high accuracy when compared to the operator-based evaluation. Even though the resorption notably altered the geometry of the explanted scaffold, the multi-stage alignment method, using the SSD, converged efficiently. The present novel approach extends the use of the commonly used mCT technique for the studying the interactions of the in-vivo biological processes. The new technique also enhances the accuracy of the morphological and morphometric analyses for the explanted scaffold. Consequently, it could be a step toward a more accurate understanding of the biological processes inside bone implants, and therefore of interest to the biomaterial scientist.

Acknowledgment

The Natural Sciences and Engineering Research Council of Canada (NSERC), the Canada Research Chair Program (CRC) and Robert Mathys Foundation (RMS) supported this research project.

3.7 References

Barrère, F., van Blitterswijk, C. A. et de Groot, K. (2006) Bone regeneration: molecular and cellular interactions with calcium phosphate ceramics. *International journal of nanomedicine*, volume 1, number 3, pp. 317-32.

Bashoor-Zadeh, M., Baroud, G. and Bohner, M. (2010) Geometric analysis of porous bone substitutes using micro-computed tomography and fuzzy distance transform. *Acta Biomaterialia*, volume 6, number 3, pp. 864-875.

Bashoor-Zadeh, M., Baroud, G. and Bohner, M. (2011) Effect of subvoxel processes on non-destructive characterization of -tricalcium phosphate bone graft substitutes. *Acta Biomaterialia*, volume 7, number 11, pp. 4045-4056.

Bay, H., Ess, A., Tuytelaars, T. and Van Gool, L. (2008) Speeded-Up Robust Features (SURF). Computer Vision and Image Understanding, volume 110, number 3, pp. 346-359. Bohner, M.

(2010) Resorbable biomaterials as bone graft substitutes. *Materials Today*, volume 13, number 1-2, pp. 24-30.

Bohner, M., Loosli, Y., Baroud, G. and Lacroix, D. (2011) Commentary: Deciphering the link between architecture and biological response of a bone graft substitute. *Acta Biomaterialia*, volume 7, number 2, pp. 478-484.

Bohner, M., van Lenthe, G. H., Grünenfelder, S., Hirsiger, W., Evison, R. and Müller, R. (2005) Synthesis and characterization of porous -tricalcium phosphate blocks. *Biomaterials*, volume 26, number 31, pp. 6099-6105.

Chan, T. F. and Vese, L. A. (2001) Active contours without edges. *IEEE Transactions on Image Processing*, volume 10, number 2, pp. 266-277.

Dice, L. R. (1945) Measures of the Amount of Ecologic Association Between Species. *Ecology*, volume 26, number 3, pp. 297.

Draenert, M., Draenert, A. and Draenert, K. (2013) Osseointegration of hydroxyapatite and remodeling-resorption of tricalciumphosphate ceramics. *Microscopy Research and Technique*, volume 76, number 4, pp. 370-380.

Feng, Y.-F., Wang, L., Li, X., Ma, Z.-S., Zhang, Y., Zhang, Z.-Y. and Lei, W. (2012) Influence of architecture of -tricalcium phosphate scaffolds on biological performance in repairing segmental bone defects. (A. Pandit, Dir.)*PloS one*, volume 7, number 11, pp. e49955.

Gaasbeek, R. D. A., Toonen, H. G., van Heerwaarden, R. J. and Buma, P. (2005) Mechanism of bone incorporation of -TCP bone substitute in open wedge tibial osteotomy in patients. *Biomaterials*, volume 26, number 33, pp. 6713-6719.

Gauthier, O., Müller, R., von Stechow, D., Lamy, B., Weiss, P., Bouler, J.-M., Aguado, E., et al. (2005) In vivo bone regeneration with injectable calcium phosphate biomaterial: a three-dimensional micro-computed tomographic, biomechanical and SEM study. *Biomaterials*, volume 26, number 27, pp. 5444-53.

Gonzalez, R. C. and Woods, R. E. (2008) Digital Image Processing (3rd Edition). 3nd edition (3e éd.). Pearson Prentice Hall.

Hollister, S., Lin, C., Saito, E., Lin, C., Schek, R., Taboas, J., Williams, J., et al. (2005) Engineering craniofacial scaffolds. *Orthodontics and Craniofacial Research*, volume 8, number 3, pp. 162-173.

Jahangir, A. A., Nunley, R. M., Mehta, S. and Sharan, A. (2008) Bone-graft substitutes in orthopaedic surgery. *AAOS Now*, number January, pp. 5-9.

Jones, A. C., Arns, C. H., Sheppard, A. P., Hutmacher, D. W., Milthorpe, B. K. and Knackstedt, M. A. (2007) Assessment of bone ingrowth into porous biomaterials using MICRO-CT. *Biomaterials*, volume 28, number 15, pp. 2491-504.

Kass, M., Witkin, A. and Terzopoulos, D. (1988) Snakes: Active contour models. *International Journal of Computer Vision*, volume 1, number 4, pp. 321-331.

Komlev, V. S., Mastrogiacomo, M., Pereira, R. C., Peyrin, F., Rustichelli, F. and Cancedda, R. (2010) Biodegradation of porous calcium phosphate scaffolds in an ectopic bone formation model studied by X-ray computed microtomograph. *European cells & materials*, volume 19, number 2004, pp. 136-146.

Lan Levengood, S. K., Polak, S. J., Poellmann, M. J., Hoelzle, D. J., Maki, A. J., Clark, S. G., Wheeler, M. B., et al. (2010) The effect of BMP-2 on micro- and macroscale osteointegration of biphasic calcium phosphate scaffolds with multiscale porosity. *Acta Biomaterialia*, volume 6, number 8, pp. 3283-3291.

Lapczyna, H., Galea, L., Wüst, S., Bohner, M., Jerban, S., Sweedy, A., Doebelin, N., et al. (2014) Effect of grain size and microporosity on the in vivo behaviour of -tricalcium phosphate scaffolds. *European cells & materials*, volume 28, pp. 299-319.

LeGeros, R. Z. (2008) Calcium Phosphate-Based Osteoinductive Materials. *Chemical Reviews*, volume 108, number 11, pp. 4742-4753.

Lu, J. X., Gallur, A., Flautre, B., Anselme, K., Descamps, M., Thierry, B. and Hardouin, P. (1998) Comparative study of tissue reactions to calcium phosphate ceramics among cancellous, cortical, and medullar bone sites in rabbits. *Journal of Biomedical Materials Research*, volume 42, number 3, pp. 357-367.

Mastrogiacomo, M., Scaglione, S., Martinetti, R., Dolcini, L., Beltrame, F., Cancedda, R. and Quarto, R. (2006) Role of scaffold internal structure on in vivo bone formation in macroporous calcium phosphate bioceramics. *Biomaterials*, volume 27, number 17, pp. 3230-3237.

Maté-Sánchez de Val, J. E., Mazón, P., Guirado, J. L. C., Ruiz, R. A. D., Ramírez Fernández, M. P., Negri, B., Abboud, M., et al. (2014) Comparison of three hydroxyapatite/-tricalcium phosphate/collagen ceramic scaffolds: An in vivo study. *Journal of Biomedical Materials Research Part A*, volume 102, number 4, pp. 1037-1046.

Otsu, N. (1979) A threshold selection method from gray-level histograms. *IEEE TRANSACTIONS ON SYSTREMS, MAN, AND CYBERNETICS*, volume SMC-9, number 1, pp. 62-66.

Papadimitropoulos, A., Mastrogiacomo, M., Peyrin, F., Molinari, E., Komlev, V. S., Rustichelli, F. and Cancedda, R. (2007) Kinetics of in vivo bone deposition by bone marrow stromal cells within a resorbable porous calcium phosphate scaffold: An X-ray computed microtomography study. *Biotechnology and Bioengineering*, volume 98, number 1, pp. 271-281.

Parkinson, I. H., Badiei, A. and Fazzalari, N. L. (2008) Variation in segmentation of bone from micro-CT imaging: implications for quantitative morphometric analysis. *Australasian Physics & Engineering Sciences in Medicine*, volume 31, number 2, pp. 160-4.

Perona, P. and Malik, J. (1990) Scale-space and edge detection using anisotropic diffusion. *IEEE Transactions on Pattern Analysis and Machine Intelligence*, volume 12, number 7, pp. 629-639.

Podaropoulos, L., Veis, A. A., Papadimitriou, S., Alexandridis, C. and Kalyvas, D. (2009) Bone Regeneration Using B-Tricalcium Phosphate in a Calcium Sulfate Matrix. *Journal of Oral Implantology*, volume 35, number 1, pp. 28-36.

Polak, S. J., Candido, S., Levengood, S. K. L. and Wagoner Johnson, A. J. (2012) Automated segmentation of micro-CT images of bone formation in calcium phosphate scaffolds. *Computerized Medical Imaging and Graphics*, volume 36, number 1, pp. 54-65.

Ruegsegger, P., Koller, B. and Muller, R. (1996) A Microtomographic System for the Nondestructive Evaluation of Bone Architecture. *Calcified Tissue International*, volume 58, number 1, pp. 24-29.

Scaglione, S., Giannoni, P., Bianchini, P., Sandri, M., Marotta, R., Firpo, G., Valbusa, U., et al. (2012) Order versus Disorder: in vivo bone formation within osteoconductive scaffolds. *Scientific Reports*, volume 2, pp. 274.

Sweedy, A., Bohner, M., van Lenthe, G. H. and Baroud, G. (2015) Segmenting CT data of in vivo -TCP scaffolds using active contours algorithm. The 25th *Interdisciplinary Research Conference on Injectable Osteoarticular Biomaterials and Bone Augmentatiocedures (GRIBOI)*, pp. 3. Toronto, Canada.

Sweedy, A., Jerban, S., Bohner, M., van Lenthe, G. H. and Baroud, G. (2015a) Refining algorithm to better segment edges in low-resolutions scans of resorbable substitutes. *The 25th Interdisciplinary Research Conference on Injectable Osteoarticular Biomaterials and Bone Augmentatiocedures (GRIBOI)*, pp. 6.

Sweedy, A., Jerban, S., Bohner, M., van Lenthe, G. H. and Baroud, G. (2015b) Edge-preserving anisotropic diffusion versus Gaussian filtering for noise reduction in medical images. *The 25th Interdisciplinary Research Conference on Injectable Osteoarticular Biomaterials and Bone Augmentatiocedures (GRIBOI)*, pp. 7. Toronto, Canada.

van der Pol, U., Mathieu, L., Zeiter, S., Bourban, P.-E., Zambelli, P.-Y., Pearce, S. G., Bouré, L. P., et al. (2010) Augmentation of bone defect healing using a new biocomposite scaffold: An in vivo study in sheep. *Acta Biomaterialia*, volume 6, number 9, pp. 3755-3762.

van Lenthe, G. H., Hagenmüller, H., Bohner, M., Hollister, S. J., Meinel, L. and Müller, R. (2007) Nondestructive micro-computed tomography for biological imaging and quantification of scaffold-bone interaction in vivo. *Biomaterials*, volume 28, number 15, pp. 2479-90.

von Doernberg, M.-C., von Rechenberg, B., Bohner, M., Grünenfelder, S., van Lenthe, G. H., Müller, R., Gasser, B., et al. (2006) In vivo behavior of calcium phosphate scaffolds with four different pore sizes. *Biomaterials*, volume 27, number 30, pp. 5186-5198.

Wang, Z., Guo, Z., Bai, H., Li, J., Li, X., Chen, G. and Lu, J. (2013) Clinical evaluation of -TCP in the treatment of lacunar bone defects: A prospective, randomized controlled study. *Materials Science and Engineering: C*, volume 33, number 4, pp. 1894-1899.

Yuan, H., Li, Y., De Bruijn, J., De Groot, K. and Zhang, X. (2000) Tissue responses of calcium phosphate cement: A study in dogs. *Biomaterials*, volume 21, number 12, pp. 1283-1290.

Zerbo, I. R., Bronckers, A. L. J. J., Lange, G. de and Burger, E. H. (2005) Localisation of osteogenic and osteoclastic cells in porous -tricalcium phosphate particles used for human maxillary sinus floor elevation. *Biomaterials*, volume 26, number 12, pp. 1445-1451.

CHAPTER 4

MULTIMODAL ANALYSIS OF *IN VIVO* RESORBABLE CaP BONE SUBSTITUTES BY COMBINING HISTOLOGY, SEM AND MICROCOMPUTED TOMOGRAPHY DATA

Multimodal analysis of in vivo resorbable CaP bone substitute by combining histology, SEM and microcomputed tomography data

Ahmed Sweedy[a], Marc Bohner[b], Gamal Baroud[c]

[a] PhD student, Laboratoire de Biomécanique, Faculté de Génie, Université de Sherbrooke, Sherbrooke, Qc Canada J1K 2R1

[b] Professor,RMS Foundation, Bischmattstrasse 12, CH-2544 Bettlach, Switzerland

[c] Professor, Faculté de Génie, Université de Sherbrooke, Sherbrooke, Qc Canada J1K 2R1

This chapter addresses the problems, mentioned in section 1.3, related to the use of 2D data including histology and SEM images to characterize phases on two scales, macro- and micro-scales. This article achieves the second general objective of this study (section 1.4). This article introduces a new developed and implemented method to integrate multimodal data from histology, SEM and mCT, achieving accurate segmentation of histology and aligning it to the pre-implantation mCT. In addition, it addresses the effect of pore size on the integration of the bone substitutes *in vivo*, in terms of bone deposition and scaffold resorption and the interactions between them. Moreover, it provides accessibility to biological processes at sub-micron level and enables addressing the role of microporosity in osteointgration and osteoconductivity of resorbable bone substitutes.

4.1 Abstract

The present study introduced and demonstrated a new method to investigate the repair process of bone defects using micro- and macroporous beta-tricalcium phosphate (β-TCP) substitutes. Specifically, the new method combined and aligned histology, SEM and pre-implantation microcomputed tomography (mCT) data to accurately characterize tissue phases found in biopsies, and thus better understand the repair process. The results included (a) the exact fraction of ceramic remnants (CR); (b) the fraction of ceramic resorbed and substituted by bone (CSB); and (c) the fraction of ceramic resorbed and not being substituted by bone (CNSB). The new method allowed in particular the detection and quantification of mineralized tissues within the 1-10 um micropores of the ceramic ("micro-bone"). The utility of the new method was demonstrated by applying it on biopsies of two β-tricalcium phosphate bone substitute groups with two differing macropore sizes implanted in an ovine model for six weeks. The total bone deposition and ceramic resorption of the two substitute groups, having macropore sizes of 510 and 1220 micron, were 25.1$\pm$8.1% and 67.5$\pm$3.2%, and 24.4$\pm$4.1% and 61.4$\pm$6.5% for the group having the larger pore size.

4.2 Introduction

Synthetic calcium phosphate (CaP) bone substitutes are increasingly being used in bone repair for their desirable biocompatibility and bioactivity properties (Barrère et al., 2006; Bohner, 2010; Gaasbeek et al., 2005; Jahangir et al., 2008; LeGeros, 2008; Podaropoulos et al., 2009; Scaglione et al., 2012; van der Pol et al., 2010; von Doernberg et al., 2006; Wang et al., 2013; Zerbo et al., 2005). There have been many studies (Bohner et al., 2011; Feng et al., 2012; Gaasbeek et al., 2005; Lan Levengood, Polak, Poellmann, et al., 2010; Lapczyna et al., 2014; Mastrogiacomo et al., 2006; Maté-Sánchez de Val et al., 2014; van Lenthe et al., 2007; von Doernberg et al., 2006; Wang et al., 2013; Yuan et al., 2000; Zerbo et al., 2005) carried out over the last three decades whose purpose was to improve the effectiveness of the CaP bone substitutes, in terms of material composition and structure. For example, a significant number of studies were conducted to determine the optimum geometric structure of the substitute in terms of macropores (pores with a diameter greater than 50 μm) (Bobyn et al., 1979; Cook et al., 1987; Hollister et al., 2005; Jones et al., 2007; Mastrogiacomo et al., 2006; O'Brien et al., 2005; van Lenthe et al., 2007; von Doernberg et al., 2006), macroporosity percentage (Jones et al., 2007; Mastrogiacomo et al., 2006), pore interconnection size (Mastrogiacomo et al., 2006), and pore shape (Jones et al., 2007; Mastrogiacomo et al., 2006). Agreement exists concerning the need to introduce macroporosity with sufficiently large interconnection size to enable cells'

migration into the macroporous substitute's structure and an effective repair process. The studies cited included many in vitro and in vivo animal investigations (Bohner et al., 2011; Feng et al., 2012; Gauthier et al., 2005; Hollister et al., 2005; Lan Levengood, Polak, Poellmann, et al., 2010; Lapczyna et al., 2014; Mastrogiacomo et al., 2006; Maté-Sánchez de Val et al., 2014; Polak et al., 2012; van Lenthe et al., 2007; von Doernberg et al., 2006; Yuan et al., 2000) as well as analyses of biopsies extracted from human patients (Gaasbeek et al., 2005; Wang et al., 2013; Zerbo et al., 2005).

In addition to the macroporosity results, recent findings interestingly showed the relevance of microporosity in the bone repair process (Draenert et al., 2013; Gaasbeek et al., 2005; Lan Levengood, Polak, Wheeler, et al., 2010; Lapczyna et al., 2014; Polak et al., 2011; Scaglione et al., 2012; Zerbo et al., 2005). Polak et al. (Polak et al., 2011) demonstrated that introducing microporosity or bone morphogenetic protein (BMP) in the structured non-resorbable biphasic calcium phosphate (BCP) substitute promoted bone growth and reduced the healing time by half. Biopsies from patients showed bone deposition in macroporous space, surprisingly accompanied with osteoblasts (Gaasbeek et al., 2005) and osteogenic cells (Zerbo et al., 2005) within the microstructure of the β-TCP scaffold. In addition to the cells, histology and TEM evaluations confirmed the existence of collagen fibers within the microporous space of hydroxyapatite (HA) (Scaglione et al., 2012); the type of collagen fibers, however, was not confirmed. Attempts were made to analyze the bony tissue found in the micropores [19, 30]. More recently, Draenert et al. (Draenert et al., 2013) reported bony ingrowth in micropores less than 5 μm in diameter. Lan Levengood et al. (Lan Levengood, Polak, Wheeler, et al., 2010) observed bone deposition within the microporous space using histology and BSE-SEM analyses of both in vitro and of in vivo samples of the biphasic calcium-phosphate substitute. Notably, these studies (Draenert et al., 2013; Lan Levengood, Polak, Wheeler, et al., 2010; Polak et al., 2011; Scaglione et al., 2012) investigated weakly- or non-resorbable bone substitutes (e.g. hydroxyapatite and biphasic calcium phosphate), and measured the effectiveness of the repair process by the percentage of newly deposited bone. This measurement is only appropriate when there is no migration and breaking of the substitute. Furthermore, the abovementioned studies (Draenert et al., 2013; Gaasbeek et al., 2005; Lapczyna et al., 2014; Polak et al., 2011; Scaglione et al., 2012; Zerbo et al., 2005) highlighted a potentially important role of the microporous substitute's structure in the bone repair process; however, very little is known about this role.

High-resolution optical histology images, specifically toluidine-blue-stained histology (TBH) photographs, are considered appropriate for characterizing bone tissue inside explanted bone substitutes (Lapczyna et al., 2014; Stalder et al., 2014; van der Pol et al., 2010; von Doernberg et al., 2006). Using TBH photographs of explanted porous scaffolds, von Doernberg et al [8]

had difficulties to differentiate the bone tissue from the ceramic for some ceramic remnants appearing blue. Further, the algorithmic systematic processing of TBH images is difficult because of the similarity in appearance of the ceramic remnants and the soft tissue. Specifically, both appear blurred and have similar color responses, in particular at the boundaries. Manual imaging and stereometric analysis were therefore commonly used to separate the three material phases (bone, ceramic remnants and soft tissue) in TBH images (Lapczyna et al., 2014; von Doernberg et al., 2006). To overcome these difficulties relating to differentiating between different material phases found in the biopsies, Stalder et al (Stalder et al., 2014) combined TBH with synchrotron mCT images for accurate characterization of the three material phases in TBH images of explanted bone substitutes. Specifically, the authors used the process of 2D-3D alignment of the TBH images and post-implantation mCT datasets to separate the ceramic materials from the soft tissue and bone. The approach by Stalder et al (Stalder et al., 2014) is both labour and computationally intensive because it uses the large 3D mCT data set to separate the ceramic remnants from the soft tissue. In the present study instead, the 2D SEM images were used to separate the ceramic remnants from the soft tissue in the TBH images. The 2D images being much easier to align, this process is much more efficient. Adding to the novelty of the methods described in this manuscript, the pre-implantation mCT dataset, which contained the original or reference ceramic structure before implantation - thus before resorption takes place - aligned with the ceramic remnants in the TBH image, created a structural reference for the ceramic phase; as such it allowed the study of the resorption process of the substitute in greater detail and with greater accuracy. A particular dimension of the methods herein was set on the quantification of mineralized tissues within the micropores of the ceramic. For ease of understanding, the terms micro- and macro-bone refer to the amount of mineralized tissues/bone detected in micro- and macropores, respectively.

The first objective of the present study was to introduce a new method to characterize the material phases found in the TBH images of explanted biopsies of resorbable bone substitutes. Specifically, the high-resolution TBH and SEM images were combined to efficiently produce a microscopic and macroscopic characterization of material phases in TBH images. Continuing with this methodological objective, the TBH images and the pre-implantation mCT datasets were used to geometrically align the initial reference substitute's structure with the substitute's remnant structure; this allowed studying the ceramic resorption process in the highly resorbable β-TCP substitute. The second objective of this study was to demonstrate the utility of the method used by analyzing two β-TCP substitute groups of two different macropore sizes, explanted from an ovine model after implantation for six weeks.

4.3 Materials and methods

4.3.1 Scaffolds, animals and surgical procedures

The scaffolds were manufactured using pure β-TCP in the form of cylinders (diameter = 8 mm; height = 13 mm) using the calcium-phosphate emulsions method, as detailed in (Bohner et al., 2005). Briefly, a mix of α-TCP/TCP (Merck, Darmstadt, Germany), viscous paraffin oil (Merck, Dietikon, Switzerland) and a Na2HPO4 solution was stirred for 45 minutes, resulting in a thick paste containing oil droplets whose size depends on the concentration of the emulsifier (BECO). After incubation in a mold for 24 hours, the hardened paste was cleaned using petroleum ether, then dried and sintered at 1250C to obtain pure β-TCP. Two pore-size groups (I-II) were produced, with incrementally increasing pore size of I=510 and II=1220 μm, respectively. The connected macro- and microporosity of the resulting β-TCP cylinders were on average 54% and 21%, respectively (Bohner et al., 2005).

The scaffold implantation location, anesthesia, medication, and surgical procedures were detailed in earlier studies (Theiss et al., 2005; von Doernberg et al., 2006). Briefly, adult Swiss Alpine sheep (3–4 years of age with a body weight ranging from 64 to 75 kg) were chosen for implantation of β-TCP scaffolds (von Doernberg et al., 2006). The animal study was approved by the local Ethical Committee and Veterinary Authorities (application number 176/2003). The scaffolds were randomly distributed to eight metaphyseal or epiphyseal defects: left and right proximal humerus, proximal femur, proximal tibia, and distal femur. The animals were sacrificed at 6 weeks for the retrieval of the β-TCP in vivo samples. Using the positions of the original markers, the samples were explanted by cutting the bone blocks containing the original implant size plus a minimum 0.4 mm margin of safety at each side. A total of six samples (2 pore sizes x 3 repeats) are used to demonstrate the new method presented in this article.

4.3.2 Micro-computed tomography, TBH and SEM imaging

The pre-implantation mCT scans of the dry substitutes were acquired using a commercial desktop mCT scanner (μCT 40, Scanco Medical AG, Bassersdorf, Switzerland) (Bashoor-Zadeh et al., 2010; Bohner et al., 2005). Histology evaluation sections, 30-40 μm thick, were cut from the post-implantation biopsies perpendicular to the biopsy longitudinal axis. As detailed in Theiss et al (Theiss et al., 2005), the histology sections were surface-stained using toluidine-blue stain and imaged at approximately 0.92-μm resolution (Theiss et al., 2005; von Doernberg et al., 2006). For SEM imaging, the histological sections were coated twice with carbon (carbon: Plano GmbH, Germany; coater: SCD 050, BAL-TEC, Balzers, FL), and connected to the metal-

lic sample holder with a conductive carbon paste (LEIT-C-PLAST, Plano GmbH, Germany). The samples were imaged in back-scattered electron mode (BSE; EVO MA 25, Carl-Zeiss SMT AG, Oberkochen, Germany).

4.3.3 The segmentation and alignment algorithms

The algorithms consisted of two sequential stages: (1) segmentation (i.e. separation of material phases) of the TBH images, and (2) 2D-3D alignment of the TBH images and the pre-implantation mCT datasets. In Stage 1, 2D SEM images were aligned with the TBH images, thus strengthening the segmentation of TBH images as the SEM image allowed separating the ceramic remnants from the soft tissue. Accordingly, Stage 1 led to the segmentation of the TBH images into bone, soft tissue, and ceramics. In Stage 2, the geometric structure of the ceramic remnants found on the TBH image was aligned with the reference ceramic structure in the pre-implantation mCT scans. Accordingly, the exact location of the substitute's free boundaries became evident, and the global and local resorption of the β-TCP substitute could thus be studied. Thus, the resorption process of the ceramic can be further divided into: (a) the exact fraction of ceramic remnants (CR); (b) the fraction of ceramic resorbed and substituted by bone (CSB); and (c) the fraction of ceramic resorbed and not being substituted by bone (CNSB). The new method also helps distinguish the micro- and macro-bone, in addition to soft tissue, as detailed below.

Segmentation of TBH images (Stage I)

The unique blue of the bone tissue in TBH images (Fig. 1(a)) combined with the unique grey intensity of ceramic content in SEM images (Fig. 1(b)) were used to analyse the material phases in the TBH more accurately. Soft tissue had low intensity in both the TBH and SEM images. Ceramic content had low and high intensity in TBH and SEM images, respectively. The micro-bone had high intensity in TBH and SEM images. Except for the micro-bone, bone had high intensity in the TBH and low intensity in the SEM images. Stage 1 comprised the following three steps.

First of all, the SEM image was aligned to the TBH image by (a) visually determining the corresponding geometric features and the matching points in both images, (b) using the matching points to calculate the 2D affine transformation (i.e. the transformation between two images of the same object captured by different equipment at different resolutions), and (c) applying this affine transformation to the SEM image.

Secondly, the Trainable Weka Segmentation (TWS) software (Fiji distribution, ImageJ (Schindelin et al., 2012)) was trained and applied to separate the bone tissue (i.e. bone and micro-bone)

from other phases in the TBH images. Briefly, the user marked sample regions of the bone. The TWS software used the marked regions to train an automatic classifier for the entire TBH image. The marked regions were accordingly analyzed by a series of training features (e.g. Gaussian blur, Hessian, etc.) to produce filtered image copies. The unique features such as the gray-value distribution and gradients in these copies were then analyzed using a random forest algorithm to segment bone in the entire TBH image. Thirdly, the same procedure was then applied to the ceramic remnants, and accordingly, the TWS software led to characterizing bone, ceramic and soft tissue in the TBH image. Also, Stage 1 enabled distinguishing between macro-bone, which was found in the macroporous space, and micro-bone, which was found in the ceramic wall.

2D-3D alignment of the TBH images and the mCT datasets (Stage II)

In this stage, segmented mCT and TBH are used in the alignment process as follows.

I. Manually find unique and matching features in both the TBH image and pre-implantation mCT scans of the same substitute:

1. Determine the unique geometric features of each phase in both TBH images and mCT image stack. Often multiple matches can be found;
2. Match the features of the TBH image to the mCT images using the strength of a unique feature such as the ceramic macropores radii;
3. Classify the matched features of the TBH and mCT data with respect to the feature strength;
4. Inspect visually to verify the best match.

II. Align the TBH image to pre-implantation mCT dataset:

1. Select a set of 100 mCT slices adjacent to the best match of the TBH images within the mCT data set;
2. Determine the 3D geometric transform parameters that minimized the number of non-overlapping pixels between the two the datasets by solving the following equation;

$$T_{opt} = argmin \sum | \, (I_{hist} - ImCT) \, | \tag{4.1}$$

Where T_{opt} is the optimized 3D geometric transform that results in best match between one mCT slice I_{mCT} of the selected 100 slices and the histology section between the histology section I_{hist};

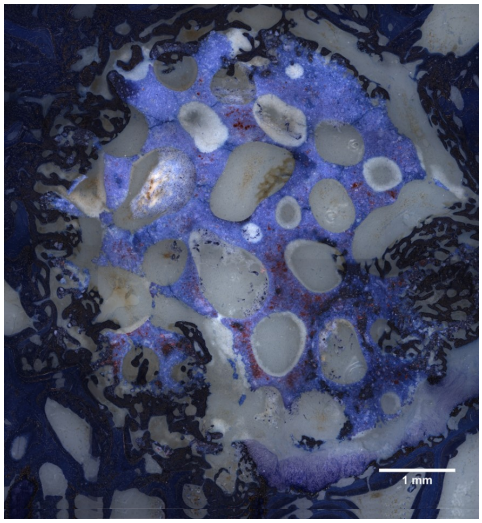

(a)

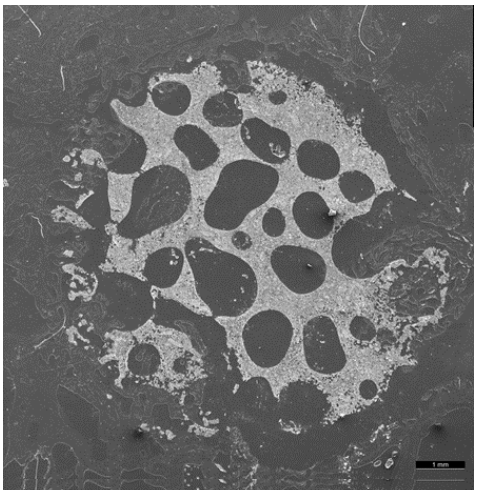

(b)

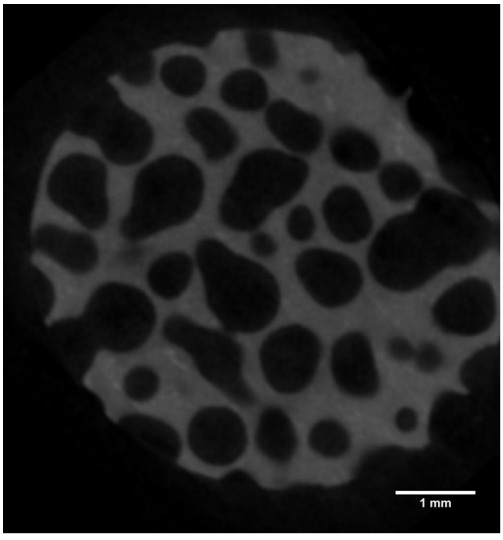

(c)

Fig. 1. (a) Histology section with toluidine blue staining; (b) SEM of the same section in (a); (c) Two dimensional pre-implantation mCT section, registered to the histology section in (a). The yellow (d) bone tissue (Tissue (c) identified with the thresholding) and blue (e) BSE-SEM voids are depicted in Fig. 9. All scale bars are 1 mm.

Figure 4.1: (a) Histology section with toluidine blue staining; (b) SEM of the same section in (a); (c) Two dimensional pre-implantation mCT section, registered to the histology section in (a). All scale bars are 1 mm.

4.3.4 TBH histomorphometry

An ellipse fitting was developed using Matlab Software (The Mathworks Inc., Massachusetts, USA) to determine the outer boundaries of the reference substitute's structure in the TBH image. This elliptical area exactly rendered the original defect site and separated it from the host bone, allowing accurate regional characterization. Next, the defect site (also referred to as the region of interest (ROI)) was divided into 8 elliptical rings/zones (with radii increasing in equal increments) for studying the evolution of the biological processes from the center to the outer boundaries of the defect site (Fig.3). Further, the surface area fraction (SAF) of each phase in each ring was determined, according to Equation 2:

$$SAF_P = N_P/N_R \tag{4.2}$$

Where SAF_P is the surface area fraction of a phase P in a specific ring R, N_P is the number of pixels occupied by the phase P and N_R is the total number of pixel in the ring R.

The thickness of the bone phases was evaluated using the method of Hildebrand (Hildebrand et Ruegsegger, 1997). Briefly, the area-based local thickness of a phase was equal to the maximal diameter of a circle inscribed in the phase. Afterwards, the statistical area mean and standard deviation of the thickness were calculated .

4.3.5 Statistics

Mean values were compared using student-t test.

4.4 Results

A typical TBH image of size II is shown in Fig. 1(a), where the image spatial resolution is 0.92 μm. The SEM image is shown in Fig. 1(b), where the spatial resolution is 3.15 μm. The alignment result is depicted in Fig. 1(c), where the presented mCT image is the result of the 3D search and alignment algorithm and is at the same spatial resolution as the TBH image. Typical results of the segmentation of the TBH image of Fig. 1(a), overlapped with its corresponding pre-implantation mCT image of Fig. 1(c), is shown in Fig. 2. In it, six phases are depicted. Soft tissue is shown in white, ceramic remnants in dark blue, macro-bone in coral, micro-bone in light blue and resorbed ceramic without and with bone substitution in yellow-brown and dark pink, respectively.

Fig. 3 shows the initial boundaries of the substitute at the time of implantation and of the defect site, identified by the aligned pre-implantation mCT image. The defect site was linearly subdivided into eight elliptical rings, R1 to R8, denoted based on the distance from the center, as shown in Fig. 3. The regional characterization of the surface area fraction of each of the six phases, existing in the segmented TBH images, as well as the reference/pre-implantation ceramic surface area fraction are given in Table 1. In it, the mean and standard deviation (SD) of the surface area fraction of each phase, in each of the eight rings (R1 to R8) and for the total implantation site, for the corresponding sample pore sizes are shown. In addition, the mean and standard error (SE) of the surface area fraction of each phase in the total implantation site were plotted in Fig. 4. The significant differences ($p < 0.05$) between groups of different pore sizes, based on the Student t-test, are shown on the plot (Fig. 4).

The Student t-test revealed some small differences between the two groups, as shown in Fig. 4, 5, and 6. No significant difference was found between samples of the two pore sizes in terms of the absolute SAF (Fig. 4) values in the total implantation/defect site of ceramics (pre-implantation), CR (post- implantation), CNSB (post-implantation), and the bone (total, macro- and micro-bone). However, a significant difference ($p < 0.05$), even though the effect was small, was found for the CSB (post-implantation) between the two groups.

Regional surface area fractions of each phase are shown in Table 1 and Fig. 5. The SAF of pre-implantation ceramic in Size II was significantly lower than in Size I in R2 and higher in R1 at $p < 0.05$ (Table 1, Fig. 5(a)). Ceramic remnants' SAF of Size II SAF was higher than Size I in R1 at $p < 0.043$ (Table 1, Fig. 5(b)). The regional SAF of ceramic substituted by bone (CSB) is shown in Fig. 5(c) where Size I was higher than Size II in R6 at $p < 0.014$. The regional SAF of resorbed ceramic without bone substitution (CNSB) is shown in Fig. 5(d). Otherwise, no significant differences in the regional SAF were found. Fig. 6 detailed the SAF of the defect site ceramic phases (normalized with reference to the pre-implantation ceramic SAF). No significance was detected between the two groups.

The mean and standard deviation of the thickness distribution of each of the six phases in the total implantation site is shown in Fig. 7 and Table 2. The wall thickness of pre-implantation ceramic of Size II samples was significantly higher than Sizes I at $p < 0.05$ (Table 1, Fig. 7). There are some trends seen in Fig. 7 that are of no significance. Fig. 8 shows the mean and standard errors in the thickness distribution of each phase in each of the eight rings (R1 to R8). The samples from the two groups exhibited uniform distribution from the peripheries toward the implant center in terms of the pre-implantation ceramic thickness (Fig. 8a). No significant difference between mean thicknesses was found with respect to the effect of pore sizes. For all pore sizes, the thickness of CR (post-implantation) increased toward the center of the implant (Fig. 8b),

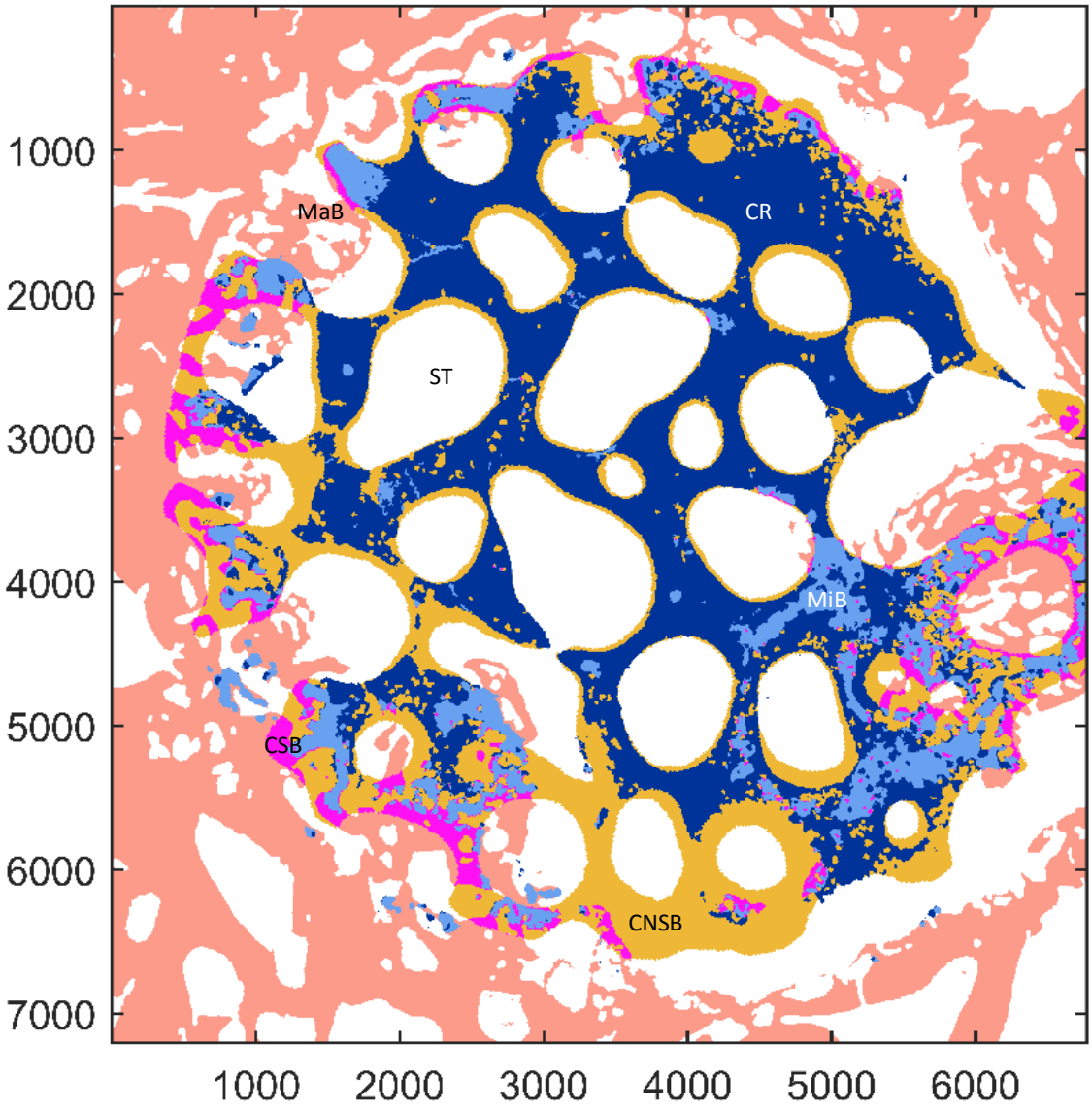

Figure 4.2 Segmentation result of the histology section in Fig. 1(a) overlapped to its corresponding segmented pre-implantation mCT section. Each color represents a different phase: white for soft tissue (ST), dark blue for ceramic remnants (CR), coral for macro-bone (MaB), light blue for micro-bone (MiB), yellow-brown and dark pink for resorbed ceramic without bone substitution (CNSB) and with bone substitution (CSB), respectively.

Fig. 2. Segmentation result of the histology section in Fig. 1(a) overlapped to its corresponding segmented pre-implantation mCT section. Each color represents a different phase: white for soft tissue (ST), dark blue for ceramic remnants (CR), coral for macro-bone (MaB), light blue for micro-bone (MiB), yellow-brown and dark pink for resorbed ceramic without bone substitution (CNSB) and with bone substitution (CSB), respectively.

whereas the thickness of CSB (post- implantation), CNSB (post-implantation) and macro-bone decreased toward the center of implant (Figs. 8(c), 8(d) and 8(e), respectively). Micro-bone showed an increase trend from the peripheries toward the center to R4, then decreased toward the center to R1 (Fig. 8(f)).

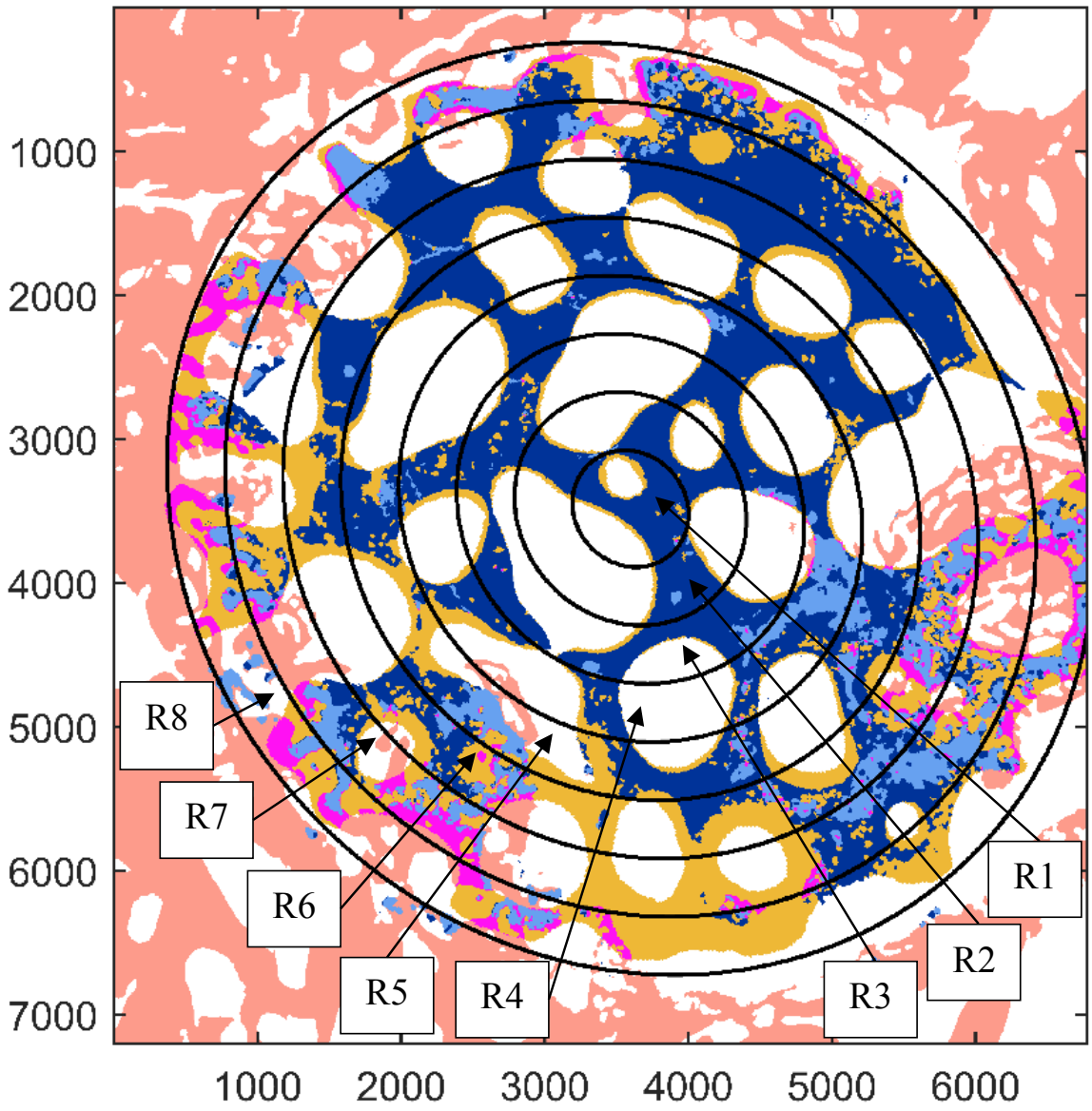

Figure 4.3 Implantation area subdivided into eight elliptical rings from center toward peripheries (R1:R8).

Fig. 3. Implantation area subdivided into eight elliptical rings from center toward peripheri
(R1:R8).

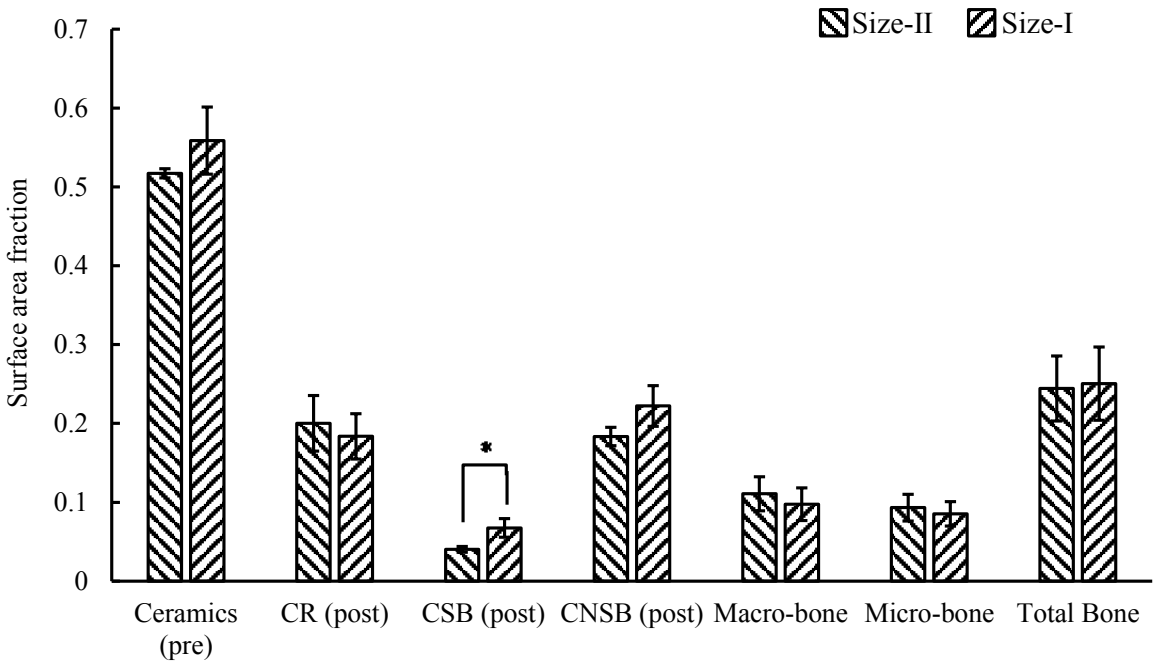

Figure 4.4 Mean and standard error of surface area fractions of different phases and different pore sizes in the different implantation sites. The asterisk (*) means that the difference is significant at $p < 0.05$.

Figure 4.4 Mean and standard error of surface area fractions of different phases and different pore sizes in the different implantation sites. The asterisk (*) means that the difference is significant at $p < 0.05$.

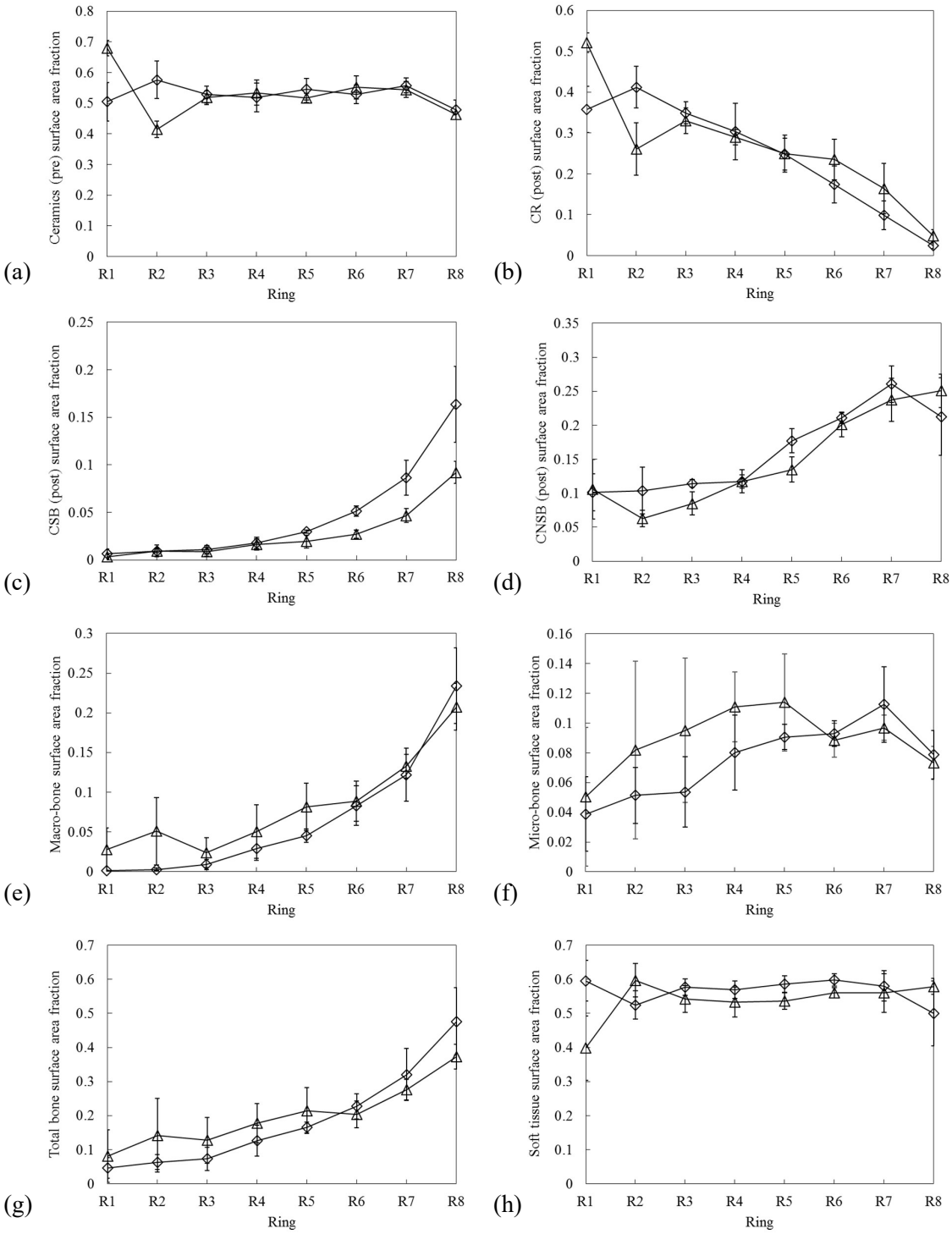

Figure 4.5 Regional surface area fraction of different phases and different pore sizes in rings R1:R8, from the center toward the peripheries of the implantation site. Pore size: (⋄) 0.51mm; (△) 1.22mm. The error bars represent the standard error.

Table 4.1 Mean and standard deviation (SD) of surface area fractions of phases in the total defect and regionally subdivided into rings.

Table 1. Mean and standard deviation (SD) of surface area fractions of phases in the total defect and regionally subdivided into rings

Group	Ring	Ceramics (SAF)								Bone (SAF)						Soft tissue(SAF)	
		Ceramic (pre)		CR (post)		CSB (post)		CNSB (post)		Macro-bone		Micro-bone		Total bone			
		Mean	SD	Mean	SD	Mean	SD	Mean	SD	Mean	SD	Mean	SD	Mean	SD	Mean	SD
Size-I	R1	0.505	0.11	0.358	0.098	0.006	0.009	0.102	0.047	0.001	0.001	0.039	0.044	0.046	0.052	0.596	0.104
	R2	0.577	0.105	0.412	0.088	0.009	0.003	0.104	0.059	0.003	0.002	0.051	0.033	0.064	0.037	0.524	0.072
	R3	0.528	0.049	0.349	0.047	0.011	0.008	0.115	0.01	0.009	0.011	0.054	0.041	0.073	0.059	0.577	0.041
	R4	0.519	0.08	0.304	0.12	0.018	0.01	0.117	0.017	0.029	0.026	0.08	0.043	0.127	0.079	0.569	0.044
	R5	0.546	0.061	0.248	0.067	0.03	0.003	0.177	0.031	0.045	0.015	0.091	0.014	0.166	0.027	0.586	0.042
	R6	0.529	0.053	0.174	0.079	0.051	0.01	0.211	0.014	0.083	0.043	0.093	0.015	0.227	0.065	0.599	0.031
	R7	0.558	0.043	0.099	0.06	0.086	0.032	0.261	0.046	0.122	0.058	0.112	0.044	0.321	0.132	0.581	0.077
	R8	0.479	0.056	0.024	0.013	0.164	0.069	0.213	0.099	0.234	0.083	0.079	0.028	0.476	0.171	0.5	0.165
	Total	0.559	0.074	0.184	0.050	0.068	0.020	0.222	0.045	0.098	0.036	0.085	0.027	0.251	0.080	0.566	0.059
Size-II	R1	0.68	0.043	0.521	0.042	0.003	0.004	0.106	0.076	0.028	0.048	0.05	0.081	0.081	0.133	0.398	0.164
	R2	0.415	0.046	0.261	0.112	0.009	0.011	0.063	0.021	0.051	0.073	0.082	0.104	0.142	0.188	0.597	0.085
	R3	0.518	0.039	0.33	0.055	0.008	0.008	0.085	0.029	0.024	0.032	0.095	0.084	0.127	0.116	0.543	0.068
	R4	0.534	0.071	0.29	0.033	0.016	0.011	0.117	0.03	0.05	0.058	0.111	0.041	0.178	0.1	0.533	0.076
	R5	0.517	0.026	0.249	0.078	0.019	0.012	0.135	0.032	0.082	0.052	0.114	0.057	0.215	0.116	0.536	0.042
	R6	0.552	0.065	0.235	0.086	0.027	0.007	0.201	0.031	0.089	0.044	0.088	0.02	0.204	0.068	0.56	0.027
	R7	0.545	0.046	0.164	0.106	0.047	0.013	0.238	0.055	0.133	0.026	0.097	0.015	0.276	0.053	0.56	0.097
	R8	0.464	0.003	0.048	0.026	0.092	0.02	0.251	0.042	0.207	0.051	0.073	0.019	0.373	0.063	0.579	0.041
	Total	0.517	0.010	0.200	0.061	0.040	0.006	0.183	0.020	0.111	0.037	0.093	0.029	0.244	0.071	0.555	0.015

Table 2-Mean and standard deviation (SD) of thickness of phases in the total implantation site.

Table 4.2 Mean and standard deviation (SD) of thickness of phases in the total implantation site.

Group	Ceramics thickness (μm)								Bone thickness (μm)			
	Ceramic (pre)		CR (post)		CSB (post)		CNSB (post)		Macro-bone		Micro-bone	
	Mean	SD	Mean	SD	Mean	SD	Mean	SD	Mean	SD	Mean	SD
Size-I	238.23	95.24	107.17	70.78	54.47	42.01	91.56	75.58	86.71	54.65	51.75	32.00
Size-II	485.30	198.00	151.69	130.27	42.99	39.46	104.70	117.58	113.23	63.22	63.27	45.54

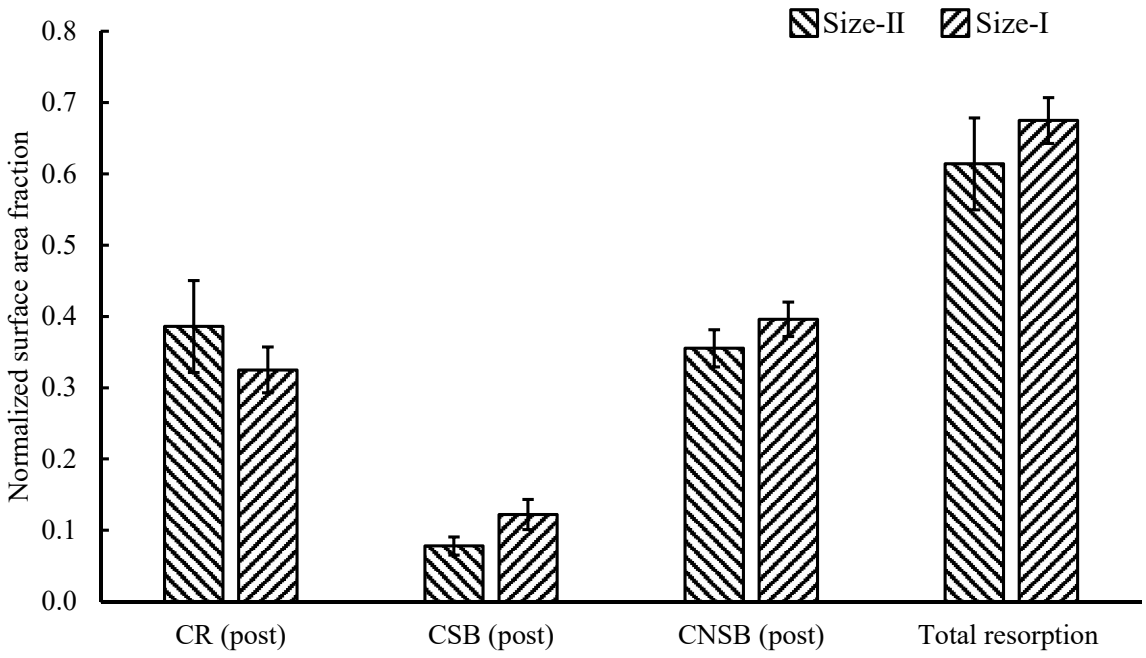

Figure 4.6 Mean and standard error of normalized surface area fractions of ceramic related phases to the surface area fraction of ceramics (pre-implantation) for different pore sizes in the total implantation site. The asterisk (*) means that the difference is significant at $p < 0.05$.

4.5 Discussion

Comprising techniques that are often used separately by scientists to study the process of bone defect repair, a multimodal analysis, integrating three classes of images, was developed. Specifically, scientists study bone repair using: (a) light microscopy, (b) scanning electron microscopy of histological sections, and (c) mCT images of 3D samples. The present multimodal analysis integrated these techniques to examine the effectiveness of two substitute groups in the repair of critical size bone defects in an ovine model. The two substitute groups (I-II) had approximately constant micro- and macroporosity, but different pore sizes and consequently variable wall thicknesses (Tables 1 and 2). The biopsies were sectioned for SEM and TBH imaging. Additionally, the two groups were mCT-scanned before implantation. Once the three classes of images were aligned, the new methods, in accordance with the study's first objective, resulted in an accurate segmentation of the TBH images. For segmentation accuracy purposes, each segmented TBH image was visually inspected by two separate image-processing researchers. The Trainable Weka segmentation algorithm (Schindelin et al., 2012) was selected because of the variability of toluidine-blue staining intensity, which could be the effect of a human factor

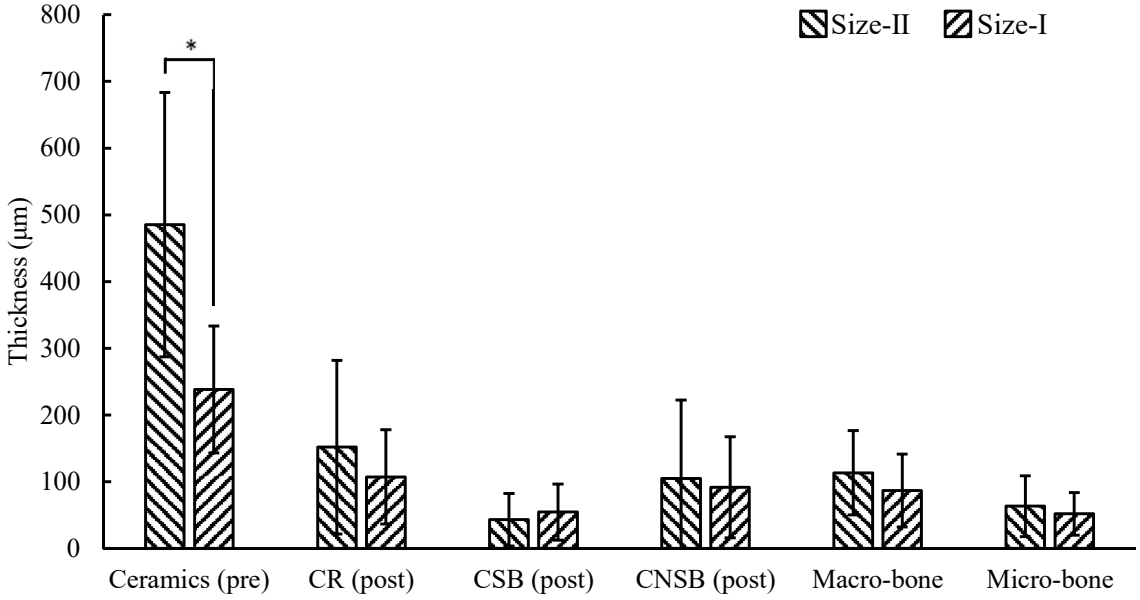

Figure 4.7: Mean and standard deviation of thickness of each phase for different pore sizes in the total implantation site. The asterisk (*) means that the difference is significant at $p < 0.05$.

Fig. 7. Mean and standard deviation of the thickness of each phase for different pore sizes in the total implantation site. The asterisk (*) means that the difference is significant at $p < 0.05$.

or bone maturity. Therefore, training a separate classifier per image or sample combined the accuracy of human segmentation with the advantage of algorithmic segmentation.

The alignment of pre-implantation mCT datasets enabled accurate determination of the boundaries of the defect site. This step was very laborious and computationally intensive, but necessary in order to accurately identify the transition from host bone to the implantation site. This step is unprecedented in terms of localizing the defect site, identifying the global and local resorption of substitutes, and classifying the resorption into zones substituted by bone and others not substituted by bone. As many studies rely on TBH images (Draenert et al., 2013; Gaasbeek et al., 2005; Lapczyna et al., 2014; Mastrogiacomo et al., 2006; van der Pol et al., 2010; von Doernberg et al., 2006; Wang et al., 2013), the present method helped the scientist achieve more accurate histomorphometric analysis and conclusions.

There were two challenges to aligning the pre-implantation mCT datasets to the TBH images: (1) the number of features in the TBH image may be limited due to the high resorption of β-TCP material; and (2) the histology sections/cuts were not always perpendicular to the longitudinal axis of the defect site, resulting in elliptical cuts of the defect sites. In some extreme cases, the ratio of the ellipse radii was close to 2. Without identifying the defect site and its elliptical form, an accurate analysis cannot be performed. Because of the limited existing features in the TBH images, human assistance was required to guide the alignment process, following the process

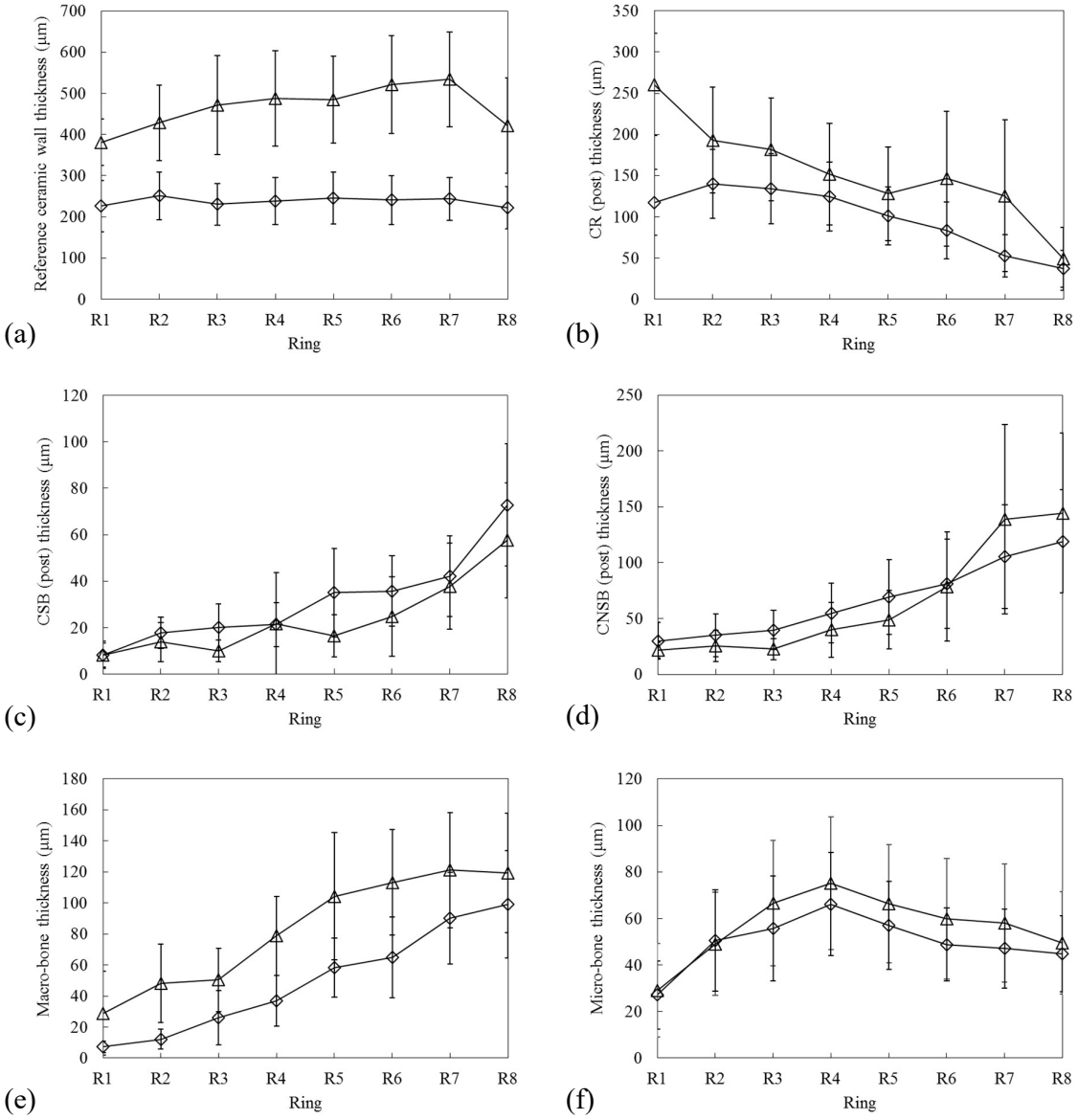

Figure 4.8 Mean and standard error of the thickness of different phases and different pore sizes in rings R1:R8, from the center toward the peripheries of the implantation site. Pore size (◇) 0.51mm; (△) 1.22mm. The error bars represent the standard error.

Fig. 8. Mean and standard error of the thickness of different phases and different pore sizes in rings R1:R8, from the center toward the peripheries of the implantation site. Pore size: (◇) 0.51mm; (△) 1.22mm. The error bars represent the standard error.

described in the Methods section. Because no reference exists for validating such an alignment method, the overlap of mCT datasets and TBH images was maximized, despite the computational cost, in accordance with Equation 1. Prior to the alignment step, the mCT datasets were resampled using bicubic interpolation at a spatial resolution of 0.92 μm, which was essential for the high-resolution TBH reference image (Bashoor-Zadeh et al., 2011).

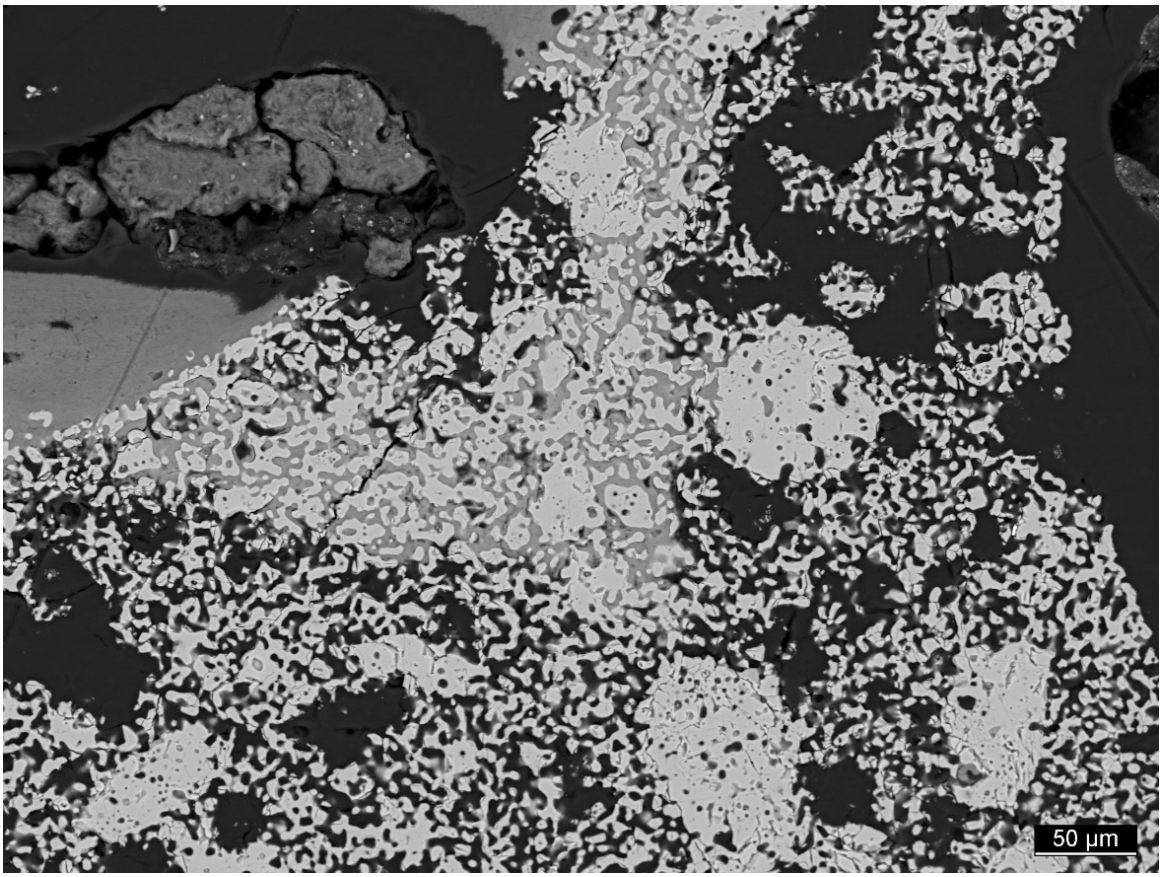

Figure 4.9 High resolution BSE-SEM image of a histology section. The scale bar is 50 μm.

There appeared a trend towards higher resorption, in terms of SAF, for the smaller pore sizes and smaller wall thickness, and accordingly for the higher specific surface area substitute. Specifically, the ratio of resorption of ceramic substituted by bone to that without bone substitution (CSB/CNSB), this ratio was 22.13.3% for Size II and 31.66.8% for Size I. This effect was however statistically not significant for the large standard error ($p < 0.05$). Still, a positive effect relating to the increased specific surface area of the macroporous substitute and the integration of the thin ceramic walls into the newly formed trabeculae can not be excluded for the limited number of sizes and of samples examined in this study. Radially, the resorption was as expected higher at the rings closer to the peripheries and decreased toward the center of the implant (Table1, Figs. 5(c) and 5(d)). The macro bone formation was 9.83.6% for Size I and 11.13.7% for Size II. The range of bone formation and, Size II being slightly higher in terms of bone deposition, appears consistent with our previous studies (von Doernberg et al., 2006). The novelty over the previous study is that we identified the micro-bone, which was found 8.52.7% for Size I and 9.32.9% for Size II. The SAF of the micro-bone appeared in the same order of magnitude as the macro-bone. Needless to say, this study provided, not the ceramic remnants, but also the

ceramic resorption. More samples and further investigation are required to study the pore effects and further interaction between the micro-, macro-bone, and ceramic resportion.

An evolutional behaviour was observed from the periphery rings to the center of the defect (Fig. 5). Specifically, the total bone, i.e. the SAF of both CSB and macro-bone decreased constantly toward the center of the bone defect, whereas the micro-bone increased from the periphery toward the middle rings and then decreased toward the center. In other words, the micro-bone was centripetally still seeding toward the center of the substitute and progressed faster than the macro-bone. It accordingly appeared that the micro-bone formation is of great relevance for the bone healing process, particularly at early implantation stages and the onset of it. The resorption was consistent (Fig. 5(d)), being in the range of 10 percent in the central area of the defect. The surface effect, i.e. CSB, was close to zero in the center of the defect, gradually increasing toward to the outer rings. Behavior similar to the CBS was observed for the macro-bone (Fig. 5(f)), whereas the micro-bone (Fig. 5(f)) already developed in the center of the defect. Furthermore, the thickness evolution appears similar to the SAF evolution of the bone phases. For example, if we consider the micro-bone thickness mean (Fig. 8(f)) and the micro-bone SAF (Fig 5(f)), the characteristic evolution from the center to periphery appears similar.

In earlier studies (Draenert et al., 2013; Gaasbeek et al., 2005; Lan Levengood, Polak, Wheeler, et al., 2010; Lapczyna et al., 2014; Scaglione et al., 2012; Zerbo et al., 2005), cells and bony tissues were identified in the microporous space of bone substitutes. To further understand the role of structured porosities in the healing process of bone defects, the present study used high-resolution TBH images and accurately characterized the material phases, including the micro-bone found the micro-porous space of the bone substitute. As such, the micro-bone and the micro-porous space may play an important role in the repair of bone defects and potentially the stability of orthopaedic implants. Whereas Polak et al. (Polak et al., 2011) found that slowly resorbable BCP implants with microporosity promoted the bone ingrowth, we specifically found that microporosity together with high resorbability in β-TCP induced bone deposition at the microscale, and this played a significant role in forming the new trabeculae while the ceramic was being resorbed. The results of the present study included (a) the exact fraction of ceramic remnants (CR); (b) the fraction of ceramic resorbed and substituted by bone (CSB); and (c) the fraction of ceramic resorbed and not being substituted by bone (CNSB).

Over previous studies, the novelty of the present article is the identification of the local and global resorption boundaries by aligning the initial reference substitute's structure with the substitute's remnant structure. The high resorbability in the β-TCP substitute appeared complex and likely extends over several geometric scales and mechanisms. BSE-SEM imaging of diamond-paste polished histological sections (Fig.9), showed the micro-cavities on the ceramic's wall sur-

face, likely forming as a result of the cell-mediated resorption. These cavities partially extended deep into the ceramic walls, indicating again the cell's action on the ceramic wall. The ceramic itself could also be resorbing in response to the acidic environment in the pore space [11], which would explain some crescent-like resorption fronts in the pore space. In contrast to Zerbo et al [11] who reported chemical dissolution as the predominant cause of β-TCP degradation, the absence of microstructural change in the core of the samples after 6 weeks of implantation suggest that in the present study, β-TCP resorption was mainly cell-mediated.

4.6 Conclusion

This study's method and related algorithms provided novel and original means to evaluate microscopic and macroscopic effects of the bone healing process. Next to identifying the resorption fronts, aligning the initial reference substitute's structure with the substitute's remnant structure allowed for more accurate evaluation of the phases found in the biopsies. As such, we extended the use of the mCT data to the study of post-implantation effects of relevance to understand complex interactions of the healing process. Specifically, the global and local resorption fronts can be identified and as such the boundaries of the defect site for more accurate evaluation of the resorption process. Like other methods, the newly developed one does have limitations. The method required that a sufficient number of geometric features be present in the explanted substitute so as to align these features with those of the pre-implantation structure.

Acknowledgment

The Natural Sciences and Engineering Research Council of Canada (NSERC), the Canada Research Chair Program (CRC) and Robert Mathys Foundation (RMS) supported this research project.

4.7 References

Barrère, F., van Blitterswijk, C. A. and de Groot, K. (2006) Bone regeneration: molecular and cellular interactions with calcium phosphate ceramics. *International journal of nanomedicine*, vol. 1, number 3, pp. 317-32.

Bashoor-Zadeh, M., Baroud, G. and Bohner, M. (2010) Geometric analysis of porous bone substitutes using micro-computed tomography and fuzzy distance transform. *Acta Biomaterialia*, volume 6, number 3, pp. 864-875.

Bashoor-Zadeh, M., Baroud, G. and Bohner, M. (2011) Effect of subvoxel processes on non-destructive characterization of -tricalcium phosphate bone graft substitutes. *Acta Biomaterialia*, volume 7, number 11, pp. 4045-4056.

Bobyn, J. D., Pilliar, R. M., Cameron, H. U. and Weatherly, G. C. (1979) The optimum pore size for the fixation of porous-surfaced metal implants by the ingrowth of bone. *Clinical orthopaedics and related research*, number 150, pp. 263-70.

Bohner, M. (2010) Resorbable biomaterials as bone graft substitutes. *Materials Today*, volume 13, number 1-2, pp. 24-30.

Bohner, M., Loosli, Y., Baroud, G. and Lacroix, D. (2011) Commentary: Deciphering the link between architecture and biological response of a bone graft substitute. *Acta Biomaterialia*, volume 7, number 2, pp. 478-484.

Bohner, M., van Lenthe, G. H., Grünenfelder, S., Hirsiger, W., Evison, R. and Müller, R. (2005) Synthesis and characterization of porous -tricalcium phosphate blocks. *Biomaterials*, volume 26, number 31, pp. 6099-6105.

Cook, S. D., Thongpreda, N., Anderson, R. C., Thomas, K. a, Haddad, R. J. and Griffin, C. D. (1987) Optimum pore size for bone cement fixation. *Clinical orthopaedics and related research*, number 223, pp. 296-302.

Draenert, M., Draenert, A. and Draenert, K. (2013) Osseointegration of hydroxyapatite and remodeling-resorption of tricalciumphosphate ceramics. *Microscopy Research and Technique*, volume 76, number 4, pp. 370-380.

Feng, Y.-F., Wang, L., Li, X., Ma, Z.-S., Zhang, Y., Zhang, Z.-Y. and Lei, W. (2012) Influence of architecture of -tricalcium phosphate scaffolds on biological performance in repairing segmental bone defects. (A. Pandit, Dir.)*PloS one*, volume 7, number 11, pp. e49955.

Gaasbeek, R. D. A., Toonen, H. G., van Heerwaarden, R. J. and Buma, P. (2005) Mechanism of bone incorporation of -TCP bone substitute in open wedge tibial osteotomy in patients. *Biomaterials*, volume 26, number 33, pp. 6713-6719.

Gauthier, O., Müller, R., von Stechow, D., Lamy, B., Weiss, P., Bouler, J.-M., Aguado, E., et al. (2005) In vivo bone regeneration with injectable calcium phosphate biomaterial: a three-dimensional micro-computed tomographic, biomechanical and SEM study. *Biomaterials*, volume 26, number 27, pp. 5444-53.

Hildebrand, T. and Ruegsegger, P. (1997) A new method for the model-independent assessment of thickness in three-dimensional images. *Journal of Microscopy*, volume 185, number 1, pp. 67-75.

Hollister, S., Lin, C., Saito, E., Lin, C., Schek, R., Taboas, J., Williams, J., et al. (2005) Engineering craniofacial scaffolds. *Orthodontics and Craniofacial Research*, volume 8, number 3, pp. 162-173.

Jahangir, A. A., Nunley, R. M., Mehta, S. and Sharan, A. (2008) Bone-graft substitutes in orthopaedic surgery. *AAOS Now*, number January, pp. 5-9.

Jones, A. C., Arns, C. H., Sheppard, A. P., Hutmacher, D. W., Milthorpe, B. K. and Knackstedt, M. A. (2007) Assessment of bone ingrowth into porous biomaterials using MICRO-CT. *Biomaterials*, volume 28, number 15, pp. 2491-504.

Lan Levengood, S. K., Polak, S. J., Poellmann, M. J., Hoelzle, D. J., Maki, A. J., Clark, S. G., Wheeler, M. B., et al. (2010) The effect of BMP-2 on micro- and macroscale osteointegration of biphasic calcium phosphate scaffolds with multiscale porosity. *Acta Biomaterialia*, volume 6, number 8, pp. 3283-3291.

Lan Levengood, S. K., Polak, S. J., Wheeler, M. B., Maki, A. J., Clark, S. G., Jamison, R. D. and Wagoner Johnson, A. J. (2010) Multiscale osteointegration as a new paradigm for the design of calcium phosphate scaffolds for bone regeneration. *Biomaterials*, volume 31, number 13, pp. 3552-3563.

Lapczyna, H., Galea, L., Wüst, S., Bohner, M., Jerban, S., Sweedy, A., Doebelin, N., et al. (2014) Effect of grain size and microporosity on the in vivo behaviour of -tricalcium phosphate scaffolds. *European cells & materials*, volume 28, pp. 299-319.

LeGeros, R. Z. (2008) Calcium Phosphate-Based Osteoinductive Materials. *Chemical Reviews*, volume 108, number 11, pp. 4742-4753.

Mastrogiacomo, M., Scaglione, S., Martinetti, R., Dolcini, L., Beltrame, F., Cancedda, R. and Quarto, R. (2006) Role of scaffold internal structure on in vivo bone formation in macroporous calcium phosphate bioceramics. *Biomaterials*, volume 27, number 17, pp. 3230-3237.

Maté-Sánchez de Val, J. E., Mazón, P., Guirado, J. L. C., Ruiz, R. A. D., Ramírez Fernández, M. P., Negri, B., Abboud, M., et al. (2014) Comparison of three hydroxyapatite/-tricalcium phosphate/collagen ceramic scaffolds: An in vivo study. *Journal of Biomedical Materials Research Part A*, volume 102, number 4, pp. 1037-1046.

O'Brien, F. J., Harley, B. A., Yannas, I. V. and Gibson, L. J. (2005) The effect of pore size on cell adhesion in collagen-GAG scaffolds. *Biomaterials*, volume 26, number 4, pp. 433-441.

Podaropoulos, L., Veis, A. A., Papadimitriou, S., Alexandridis, C. and Kalyvas, D. (2009) Bone Regeneration Using B -Tricalcium Phosphate in a Calcium Sulfate Matrix. *Journal of Oral Implantology*, volume 35, number 1, pp. 28-36.

Polak, S. J., Candido, S., Levengood, S. K. L. and Wagoner Johnson, A. J. (2012) Automated segmentation of micro-CT images of bone formation in calcium phosphate scaffolds. *Computerized Medical Imaging and Graphics*, volume 36, number 1, pp. 54-65.

Polak, S. J., Levengood, S. K. L., Wheeler, M. B., Maki, A. J., Clark, S. G. and Johnson, A. J. W. (2011) Analysis of the roles of microporosity and BMP-2 on multiple measures of bone regeneration and healing in calcium phosphate scaffolds. *Acta Biomaterialia*, volume 7, number 4, pp. 1760-1771.

Scaglione, S., Giannoni, P., Bianchini, P., Sandri, M., Marotta, R., Firpo, G., Valbusa, U., et al. (2012) Order versus Disorder: in vivo bone formation within osteoconductive scaffolds. *Scientific Reports*, volume 2, pp. 274.

Schindelin, J., Arganda-Carreras, I., Frise, E., Kaynig, V., Longair, M., Pietzsch, T., Preibisch, S., et al. (2012) Fiji: an open-source platform for biological-image analysis. *Nature Methods*, volume 9, number 7, pp. 676-682.

Stalder, A. K., Ilgenstein, B., Chicherova, N., Deyhle, H., Beckmann, F., Müller, B. and Hieber, S. E. (2014) Combined use of micro computed tomography and histology to evaluate the regenerative capacity of bone grafting materials. *International Journal of Materials Research*, volume 105, number 7, pp. 679-691.

Theiss, F., Apelt, D., Brand, B., Kutter, A., Zlinszky, K., Bohner, M., Matter, S., et al. (2005) Biocompatibility and resorption of a brushite calcium phosphate cement. *Biomaterials*, volume 26, number 21, pp. 4383-4394.

van der Pol, U., Mathieu, L., Zeiter, S., Bourban, P.-E., Zambelli, P.-Y., Pearce, S. G., Bouré, L. P., et al. (2010) Augmentation of bone defect healing using a new biocomposite scaffold: An in vivo study in sheep. *Acta Biomaterialia*, volume 6, number 9, pp. 3755-3762.

van Lenthe, G. H., Hagenmüller, H., Bohner, M., Hollister, S. J., Meinel, L. and Müller, R. (2007) Nondestructive micro-computed tomography for biological imaging and quantification of scaffold-bone interaction in vivo. *Biomaterials*, volume 28, number 15, pp. 2479-90.

von Doernberg, M.-C., von Rechenberg, B., Bohner, M., Grünenfelder, S., van Lenthe, G. H., Müller, R., Gasser, B., et al. (2006) In vivo behavior of calcium phosphate scaffolds with four different pore sizes. *Biomaterials*, volume 27, number 30, pp. 5186-5198.

Wang, Z., Guo, Z., Bai, H., Li, J., Li, X., Chen, G. and Lu, J. (2013) Clinical evaluation of -TCP in the treatment of lacunar bone defects: A prospective, randomized controlled study. *Materials Science and Engineering: C*, volume 33, number 4, pp. 1894-1899.

Yuan, H., Li, Y., De Bruijn, J., De Groot, K. and Zhang, X. (2000) Tissue responses of calcium phosphate cement: A study in dogs. *Biomaterials*, volume 21, number 12, pp. 1283-1290.

Zerbo, I. R., Bronckers, A. L. J. J., Lange, G. de and Burger, E. H. (2005) Localisation of osteogenic and osteoclastic cells in porous -tricalcium phosphate particles used for human maxillary sinus floor elevation. *Biomaterials*, 26, number 12, pp. 1445-1451.

CHAPTER 5

CONCLUSION

The two overall objectives of the present thesis concerned providing new methods to investigate the bone healing process using resorbable bone substitutes. The first objective was to develop, implement and validate new image-processing methods, which permitted the accurate analysis of the post-implantation mCT datasets of bone substitutes explanted from an ovine model. Previously, the mCT imaging technique was largely used to examine the pre-implantation ceramic structures of the β-TCP substitutes. The novel methods of the first objective entailed extending the use of the mCT technique to study the phases that are also present in the explanted substitutes. Besides the ceramic remnant phase, tissue phases found in the explanted substitute included soft tissue and bone deposited in the micro and macro pores of the bone substitute. The analysis of the tissues in the post-implantation mCT datasets remains difficult because of the similar mineralization level and hence the grey-value data of the bone and the ceramic remnants. The methods related to the second objective resulted in extracting the micro-bone found the ceramic microporous space.

The novel methods and related algorithms, presented in this work related to the first objective, combined the pre- and post-implantation mCT datasets to identify and analyze the characteristic properties of the ceramic found in the biopsies, thereby providing data on characteristics of the ceramic remnants for more accurate analyses. Specifically, using pre- and post-implantation mCT datasets, the 3D ceramic structures of the same substitute before and after implantation were geometrically aligned, thus providing access to data on grey-scale-value characteristics of the phases present in the post-implantation mCT datasets, and thereby rendering the analyses of these phases more accurate. Moreover, combining the data on grey-value characteristics with advanced image processing methods such as contour-based treatment further strengthened the macro-scale analyses of the post-implantation mCT datasets and accurately segmented macro-bone, ceramic remnants and soft-tissue phases. Using the similarity matrix theory, the new methods and related algorithms were validated by comparing the algorithmic results to those obtained by an image-processing expert, and resulted in 94% agreement. This approach was further validated by visual comparison with the histology evaluation results. Accurate 3D analyses of the phases found in the macro structure of the explanted scaffolds thus became possible. Unfortunately, the analysis of the micro-bone within the ceramic phase was not sufficiently accurate for the low 30-micron spatial resolution of the mCT datasets. The analysis of the micro-bone was therefore the subject of the second objective of the thesis.

For the purposes of the second objective, a new method and related algorithm combined multi-modal imaging, such as high-resolution histology and SEM techniques, with the pre-implantation mCT dataset of the same sample, thereby allowing for distinguishing macro- from micro-bone. The 2D high-resolution histology and SEM images had pixel sizes of 0.92 and 3.15 microns

respectively. Accordingly, 3D mCT and 2D SEM data were sub-voxelized to match the resolution of histology images and allow precise alignment. Once aligned, distinguishing macro from micro-bone became possible. Additionally, the multimodal alignment helped to accurately locate the local and global boundaries of the initial substitute, thus making possible the study of the local and global resorption of the ceramic. Further in line with the second broad objective, the new 2D-3D method was used to study the bone healing process as a function of the ceramic bone substitute's macroscopic pore structure. Specifically, β-TCP scaffolds of two different pore-size groups were implanted in an ovine model for six weeks. Once explanted, the histology, SEM, and mCT data became available. Our preliminary results from three selected samples of each group indicated significantly higher bone deposition and ceramic resorption rate for the group of smaller pore size and wall thickness.

The thesis employed and validated novel methods, and also demonstrated the usefulness of the mCT technique for studying the bone healing process using the post-implantation mCT dataset. The 3D alignment process provided access to data on the grey-value characteristics of the macrophases present in the biopsies, thus allowing the analysis of macro-bone, ceramic remnants and soft tissue. The 2D-3D alignment process provided access to the micro and macro processes, thereby allowing a more accurate analysis of the bone deposition and ceramic resorption. Furthermore, histology images of random cuts were found in the 3D mCT datasets, which allowed for accurate controls, validation, and evaluation. The reader should be aware, however, that finding the histology images in 3D mCT datasets was a manual and therefore labor-intensive process. The reader must also be aware of the high computational cost of the algorithms, which allowed extending the use of the mCT technique for studying the explanted substitutes and, therefore, the bone healing process and how to relate it to the design of the bone substitute.

Conclusion (Français)

Les deux objectifs généraux de la présente thèse concernaient la conception de nouvelles méthodes pour l'étude du processus de guérison des os au moyen de substituts osseux résorbables. Le premier objectif visait à élaborer, à appliquer et à valider de nouvelles méthodes de traitement de l'image permettant de procéder à une analyse précise après implantation des ensembles de données de microtomographie par rayons x de substituts osseux explantés d'un modèle ovin. Antérieurement, la technique de microtomographie par rayons x était largement utilisée pour l'examen des structures céramiques de substituts β-TCP avant implantation. Les méthodes liées au second objectif ont permis d'extraire le micro-os trouvé dans l'espace microporeux de la céramique.

Les méthodes novatrices du premier objectif nécessitaient d'étendre l'application de la technique de microtomographie par rayons X à l'étude des phases également présentes dans les substituts explantés. Outre la phase résidus céramiques, les phases tissus observées dans le substitut explanté incluaient la néoformation de tissus mous et osseux dans les micro et macropores du substitut osseux. L'analyse des tissus après implantation au moyen des ensembles de données de microtomographie par rayons X demeure ardue en raison d'un niveau de minéralisation similaire et, partant, de la valeur de gris des résidus osseux et céramiques. Les méthodes novatrices et les algorithmes s'y rapportant combinaient les ensembles de données de microtomographie par rayons X avant et après implantation afin de déterminer et d'analyser les propriétés caractéristiques de la céramique retrouvée dans les biopsies, générant ainsi des données sur les caractéristiques des résidus céramiques pour la production d'analyses plus précises. Spécifiquement, utilisant les ensembles de données de microtomographie par rayons X avant et après implantation, les structures céramiques en 3D du même substitut avant et après implantation ont été alignées géométriquement, générant ainsi des données sur les caractéristiques des valeurs de couleur sur une échelle de gris des phases présentes dans les ensembles de données de microtomographie par rayons X après implantation, pour une analyse plus précise de ces phases. De plus, le fait de combiner les données sur les caractéristiques des valeurs de gris avec des méthodes avancées de traitement de l'image comme la méthode du contour actif, a encore davantage renforcé les analyses à grande échelle des ensembles de données de microtomographie par rayons X après implantation et représenté de manière précise les phases du matériel macro-osseux, les résidus céramiques et les tissus mous. À l'aide de la théorie de la matrice de similarité, les nouvelles méthodes et les algorithmes s'y rapportant ont été validés en comparant les résultats algorithmiques à ceux obtenus par un expert en traitement de l'image, et une concordance à 94 % a été obtenue. Cette approche a été validée en la comparant visuellement aux résultats d'évaluation histologique. Des analyses précises des phases en 3D relevées dans la macrostructure des matri-

ces explantées ont ainsi été rendues possibles. Malheureusement, l'analyse micro-osseuse de la phase céramique n'était pas suffisamment précise pour la basse résolution spatiale à 30 microns des ensembles de données de microtomographie par rayons x. L'analyse micro-osseuse est par conséquent devenue l'enjeu du second objectif de la thèse.

Pour les besoins de ce second objectif, une nouvelle méthode et l'algorithme s'y rapportant, combinant l'imagerie multimodale, telles les techniques histologiques et MEB à haute résolution, aux ensembles de données de microtomographie par rayons X avant implantation du même échantillon, ont permis de différencier le matériel macro-osseux du matériel micro-osseux. La taille des pixels des images histologiques à haute résolution en 2D et des images MEB étaient de 0,92 et 3,15 microns respectivement. De la même façon, les données de microtomographie par rayons X en 3D et les données de MEB en 2D ont été sous-voxelisées pour correspondre à la résolution des images histologiques et permettre un alignement précis. Une fois l'alignement obtenu, il a été possible de distinguer le matériel macro-osseux du matériel micro-osseux. L'alignement multimodal a également permis de localiser avec précision, localement et globalement, les limites du substitut initial, rendant possible l'étude de la résorption locale et globale de la céramique, laquelle autrement n'est pas possible. Conformément au second objectif général, la nouvelle méthode 2D-3D a servi à l'étude du processus de guérison des os en tant que fonction de la structure poreuse microscopique du substitut osseux de céramique. Spécifiquement, des matrices β-TCP provenant de groupes dont la taille des pores divergeait ont été implantées dans un modèle ovin pendant six semaines. Une fois explantés, les données histologiques, MEB et de microtomographie par rayons X sont devenues accessibles. Nos résultats préliminaires à partir des trois échantillons sélectionnés dans chaque groupe indiquaient un taux de néoformation osseuse et de résorption céramique beaucoup plus élevé chez le groupe dont la taille des pores et l'épaisseur des parois étaient plus petites.

La thèse a appliqué et validé des méthodes novatrices; elle a aussi démontré l'utilité de la technique de microtomographie par rayons X pour l'étude du processus de guérison des os à l'aide d'un ensemble de données de microtomographie par rayons X après implantation. Le processus d'alignement en 3D a généré des données accessibles relatives aux caractéristiques des macrophases présentes dans les biopsies, permettant ainsi l'analyse du matériel macro-osseux, des résidus céramiques et des tissus mous. L'alignement en 2D-3D a permis d'observer les micro et macro processus, permettant ainsi d'effectuer une analyse encore plus précise de la néoformation osseuse et de la résorption céramique. En outre, des images histologiques de coupes aléatoires ont été répertoriées dans les ensembles de données de microtomographie par rayons X en 3D, permettant par conséquent d'effectuer des contrôles, validations et évaluations plus précis. Il convient de souligner pour le lecteur que les images histologiques des ensembles de

données de microtomographie par rayons X en 3D ont été répertoriées manuellement et que l'exercice s'est révélé très fastidieux. Le lecteur doit également être informé du coût élevé des calculs algorithmiques dû à la prolongation d'utilisation de la technique de microtomographie par rayons X pour les besoins de l'étude des substituts explantés et, conséquemment, du processus de guérison des os et de la façon dont celui-ci peut être lié à la conception du substitut osseux.

LIST OF REFERENCES

Aykac, D., Price, J. and Wall, J. (2005). 3D Segmentation of the Mouse Spleen in microCT via Active Contours. In *IEEE Nuclear Science Symposium Conference Record, 2005*. volume 3. IEEE, pp. 1542–1545.

Barrère, F., van Blitterswijk, C. A. and de Groot, K. (2006). Bone regeneration: molecular and cellular interactions with calcium phosphate ceramics. *International journal of nanomedicine*, volume 1, number 3, pp. 317–32.

Bashoor-Zadeh, M., Baroud, G. and Bohner, M. (2010). Geometric analysis of porous bone substitutes using micro-computed tomography and fuzzy distance transform. *Acta Biomaterialia*, volume 6, number 3, pp. 864–875.

Bashoor-Zadeh, M., Baroud, G. and Bohner, M. (2011). Effect of subvoxel processes on non-destructive characterization of β-tricalcium phosphate bone graft substitutes. *Acta Biomaterialia*, volume 7, number 11, pp. 4045–4056.

Bay, H., Ess, A., Tuytelaars, T. and Van Gool, L. (2008). Speeded-Up Robust Features (SURF). *Computer Vision and Image Understanding*, volume 110, number 3, pp. 346–359.

Becker, S., Maissen, O., Ponomarev, I., Igor, P., Stoll, T., Thierry, S., Rahn, B., Wilke, I. and Ingo, W. (2006). Osteopromotion by a beta-tricalcium phosphate/bone marrow hybrid implant for use in spine surgery. *Spine*, volume 31, number 1, pp. 11–7.

Becker, S., Maissen, O., Ponomarev, I., Stoll, T., Meury, T., Sprecher, C., Alini, M. and Wilke, I. (2008). Osteopromotion with a plasmatransglutaminase on a beta-TCP ceramic. *Journal of materials science. Materials in medicine*, volume 19, number 2, pp. 659–65.

Bohner, M. (2010). Resorbable biomaterials as bone graft substitutes. *Materials Today*, volume 13, number 1-2, pp. 24–30.

Bohner, M., Loosli, Y., Baroud, G. and Lacroix, D. (2011). Commentary: Deciphering the link between architecture and biological response of a bone graft substitute. *Acta Biomaterialia*, volume 7, number 2, pp. 478–484.

Buie, H. R., Campbell, G. M., Klinck, R. J., MacNeil, J. a. and Boyd, S. K. (2007). Automatic segmentation of cortical and trabecular compartments based on a dual threshold technique for in vivo micro-CT bone analysis. *Bone*, volume 41, number 4, pp. 505–15.

Carlier, a., Chai, Y. C., Moesen, M., Theys, T., Schrooten, J., Van Oosterwyck, H. and Geris, L. (2011). Designing optimal calcium phosphate scaffold-cell combinations using an integrative model-based approach. *Acta biomaterialia*, volume 7, number 10, pp. 3573–85.

Cartmell, S., Huynh, K., Lin, A., Nagaraja, S. and Guldberg, R. (2004). Quantitative microcomputed tomography analysis of mineralization within three-dimensional scaffoldsin vitro. *Journal of Biomedical Materials Research*, volume 69A, number 1, pp. 97–104.

Caselles, V., Kimmel, R. and Sapiro, G. (2001). Geodesic active contours. In *Proceedings of IEEE International Conference on Computer Vision*. volume 10. IEEE Comput. Soc. Press, pp. 694–699.

Catté, F., Lions, P., Morel, J. and Coll, T. (1992). Image selective smoothing and edge detection by nonlinear diffusion. *SIAM Journal on Numerical analysis*, volume 29, number 1, pp. 182–193.

Chan, T. and Vese, L. (2001). Active contours without edges. *IEEE Transactions on Image Processing*, volume 10, number 2, pp. 266–277.

Darabi, A., Chandelier, F. and Baroud, G. (2007). Morphometric analysis of trabecular bone thickness using different algorithms. *Canadian Journal of Electrical and Computer Engineering*, volume 32, number 3, pp. 157–163.

Darabi, A., Chandelier, F. and Baroud, G. (2009). Thickness analysis and reconstruction of trabecular bone and bone substitute microstructure based on fuzzy distance map using both ridge and thinning skeletonization. *Canadian Journal of Electrical and Computer Engineering*, volume 34, number 1, pp. 57–62.

Demenegas, F., Tassani, S. and Matsopoulos, G. K. (2011). Active segmentation of micro-CT trabecular bone images. In *2011 10th International Workshop on Biomedical Engineering*. IEEE, pp. 1–4.

Detsch, R., Mayr, H. and Ziegler, G. (2008). Formation of osteoclast-like cells on HA and TCP ceramics. *Acta biomaterialia*, volume 4, number 1, pp. 139–48.

Dong, J., Uemura, T., Shirasaki, Y. and Tateishi, T. (2002). Promotion of bone formation using highly pure porous beta-TCP combined with bone marrow-derived osteoprogenitor cells. *Biomaterials*, volume 23, number 23, pp. 4493–502.

Draenert, M., Draenert, A. and Draenert, K. (2013). Osseointegration of hydroxyapatite and remodeling-resorption of tricalciumphosphate ceramics. *Microscopy Research and Technique*, volume 76, number 4, pp. 370–380.

Elmoutaouakkil, A., Peyrin, F., Elkafi, J. and Laval-Jeantet, A.-M. (2002). Segmentation of cancellous bone from high-resolution computed tomography images: influence on trabecular bone measurements. *IEEE transactions on medical imaging*, volume 21, number 4, pp. 354–62.

Feng, Y.-F., Wang, L., Li, X., Ma, Z.-S., Zhang, Y., Zhang, Z.-Y. and Lei, W. (2012). Influence of Architecture of β-Tricalcium Phosphate Scaffolds on Biological Performance in Repairing Segmental Bone Defects. *PLoS ONE*, volume 7, number 11, p. e49955.

Frangakis, a. S. and Hegerl, R. (2001). Noise reduction in electron tomographic reconstructions using nonlinear anisotropic diffusion. *Journal of structural biology*, volume 135, number 3, pp. 239–50.

Gaasbeek, R. D. A., Toonen, H. G., Heerwaarden, R. J. V. and Buma, P. (2005). Mechanism of bone incorporation of b-TCP bone substitute in open wedge tibial osteotomy in patients. volume 26, pp. 6713–6719.

Gauthier, O., Bouler, J. M., Weiss, P., Bosco, J., Daculsi, G. and Aguado, E. (1999). Kinetic study of bone ingrowth and ceramic resorption associated with the implantation of different injectable calcium-phosphate bone substitutes. *Journal of biomedical materials research*, volume 47, number 1, pp. 28–35.

Gauthier, O., Müller, R., von Stechow, D., Lamy, B., Weiss, P., Bouler, J.-M., Aguado, E. and Daculsi, G. (2005). In vivo bone regeneration with injectable calcium phosphate biomaterial: a three-dimensional micro-computed tomographic, biomechanical and SEM study. *Biomaterials*, volume 26, number 27, pp. 5444–53.

Gonzalez, R. C. and Woods, R. E. (2008). *Digital Image Processing (3rd Edition)*, 3rd edition. Pearson Prentice Hall, 976 pp.

Habraken, W., Habibovic, P., Epple, M. and Bohner, M. (2016). Calcium phosphates in biomedical applications: materials for the future? *Materials Today*, volume 19, number 2, pp. 69–87.

Hench, L. L. (2006). The story of Bioglass. *Journal of materials science. Materials in medicine*, volume 17, number 11, pp. 967–78.

Hench, L. L. and Polak, J. M. (2002). Third-generation biomedical materials. *Science (New York, N.Y.)*, volume 295, number 5557, pp. 1014–7.

Hildebrand, T. and Rüegsegger, P. (1997). A new method for the modelindependent assessment of thickness in threedimensional images. *Journal of microscopy*, volume 185, number November 1995, pp. 67–75.

Hilldore, A. J., Morgan, A. W., Woodard, J. R. and Wagoner Johnson, A. J. (2009). The curve integration method is comparable to manual segmentation for the analysis of bone/scaffold composites using micro-CT. *Journal of biomedical materials research. Part B, Applied biomaterials*, volume 88, number 1, pp. 271–9.

Hing, K. a., Annaz, B., Saeed, S., Revell, P. a. and Buckland, T. (2005). Microporosity enhances bioactivity of synthetic bone graft substitutes. *Journal of materials science. Materials in medicine*, volume 16, number 5, pp. 467–75.

Hollister, S., Lin, C., Saito, E., Lin, C., Schek, R., Taboas, J., Williams, J., Partee, B., Flanagan, C., Diggs, A., Wilke, E., Van Lenthe, G., Muller, R., Wirtz, T., Das, S., Feinberg, S. and Krebsbach, P. (2005). Engineering craniofacial scaffolds. *Orthodontics and Craniofacial Research*, volume 8, number 3, pp. 162–173.

Jones, A. C., Arns, C. H., Hutmacher, D. W., Milthorpe, B. K., Sheppard, A. P. and Knackstedt, M. A. (2009). The correlation of pore morphology, interconnectivity and physical properties of 3D ceramic scaffolds with bone ingrowth. *Biomaterials*, volume 30, number 7, pp. 1440–51.

Jones, A. C., Arns, C. H., Sheppard, A. P., Hutmacher, D. W., Milthorpe, B. K. and Knackstedt, M. A. (2007). Assessment of bone ingrowth into porous biomaterials using MICRO-CT. *Biomaterials*, volume 28, number 15, pp. 2491–504.

Jones, A. C., Milthorpe, B., Averdunk, H., Limaye, A., Senden, T. J., Sakellariou, A., Sheppard, A. P., Sok, R. M., Knackstedt, M. A., Brandwood, A., Rohner, D. and Hutmacher, D. W.

(2004). Analysis of 3D bone ingrowth into polymer scaffolds via micro-computed tomography imaging. *Biomaterials*, volume 25, number 20, pp. 4947–54.

Kass, M., Witkin, A. and Terzopoulos, D. (1988). Snakes: Active contour models. *International Journal of Computer Vision*, volume 1, number 4, pp. 321–331.

Keller, C. (2008). Methods, compositions and systems for analyzing imaging data.

Komlev, V. S., Mastrogiacomo, M., Pereira, R. C., Peyrin, F., Rustichelli, F. and Cancedda, R. (2010). Biodegradation of porous calcium phosphate scaffolds in an ectopic bone formation model studied by X-ray computed microtomograph. *European cells & materials*, volume 19, number 2004, pp. 136–146.

Komlev, V. S., Peyrin, F., Mastrogiacomo, M., Cedola, A., Papadimitropoulos, A., Rustichelli, F. and Cancedda, R. (2006). Kinetics of in vivo bone deposition by bone marrow stromal cells into porous calcium phosphate scaffolds: an X-ray computed microtomography study. *Tissue engineering*, volume 12, number 12, pp. 3449–58.

Krauth, A., Blanc, R., Poveda, A., Jeanmonod, D., Morel, A. and Székely, G. (2010). A mean three-dimensional atlas of the human thalamus: Generation from multiple histological data. *NeuroImage*, volume 49, number 3, pp. 2053–2062.

Laine, C., Guallar, E., Mulrow, C., Taichman, D. B., Cornell, J. E., Cotton, D., Griswold, M. E., Localio, A. R., Meibohm, A. R., Stack, C. B., Williams, S. V. and Goodman, S. N. (2013). Closing in on the truth about recombinant human bone morphogenetic protein-2: evidence synthesis, data sharing, peer review, and reproducible research. *Annals of internal medicine*, volume 158, number 12, pp. 916–8.

Landrigan, M. (2009). Evaluation of methods for measuring microdamage accumulation in cortical bone. , number April.

Lapczyna, H., Galea, L., Wüst, S., Bohner, M., Jerban, S., Sweedy, A., Doebelin, N., van Garderen, N., Hofmann, S., Baroud, G., Müller, R. and von Rechenberg, B. (2014). Effect of grain size and microporosity on the in vivo behaviour of β-tricalcium phosphate scaffolds. *European cells & materials*, volume 28, pp. 299–319.

LeGeros, R. Z. (2008). Calcium Phosphate-Based Osteoinductive Materials. *Chemical Reviews*, volume 108, number 11, pp. 4742–4753.

Lemons, J. E., Bajpai, P. K., Patka, P., Bonel, G., Starling, L. B., Rosenstiel, T., Muschler, G., Kampner, S. and Timmermans, J. (1988). Significance of the porosity and physical chemistry of calcium phosphate ceramics. Orthopedic uses. *Annals of the New York Academy of Sciences*, volume 523, pp. 278–82.

Lowe, D. G. (2004). Distinctive Image Features from Scale-Invariant Keypoints. *International Journal of Computer Vision*, volume 60, number 2, pp. 91–110.

Lu, J., Descamps, M., Dejou, J., Koubi, G., Hardouin, P., Lemaitre, J. and Proust, J.-P. (2002). The biodegradation mechanism of calcium phosphate biomaterials in bone. *Journal of biomedical materials research*, volume 63, number 4, pp. 408–12.

Lu, J. X., Gallur, A., Flautre, B., Anselme, K., Descamps, M., Thierry, B. and Hardouin, P. (1998). Comparative study of tissue reactions to calcium phosphate ceramics among cancellous, cortical, and medullar bone sites in rabbits. *Journal of Biomedical Materials Research*, volume 42, number 3, pp. 357–367.

Mallat, S. (1989). A theory for multiresolution signal decomposition: the wavelet representation. *IEEE Transactions on Pattern Analysis and Machine Intelligence*, volume 11, number 7, pp. 674–693.

Mastrogiacomo, M., Scaglione, S., Martinetti, R., Dolcini, L., Beltrame, F., Cancedda, R. and Quarto, R. (2006). Role of scaffold internal structure on in vivo bone formation in macroporous calcium phosphate bioceramics. *Biomaterials*, volume 27, number 17, pp. 3230–3237.

Müller, R. and Rüegsegger, P. (1997). Micro-tomographic imaging for the nondestructive evaluation of trabecular bone architecture. *Studies In Health Technology And Informatics*, volume 40, pp. 61–79.

Museyko, O., Marshall, R. P., Lu, J., Hess, A., Schett, G., Amling, M., Kalender, W. a. and Engelke, K. (2015). Registration of 2D histological sections with 3D micro-CT datasets from small animal vertebrae and tibiae. *Computer Methods in Biomechanics and Biomedical Engineering*, volume 18, number 15, pp. 1658–1673.

Nather, A. (2005). *Bone grafts and bone substitutes: basic science and clinical applications*. World Scientific Publishing Co. Pte. Ltd.

Osechinskiy, S. and Kruggel, F. (2011). Slice-to-Volume Nonrigid Registration of Histological Sections to MR Images of the Human Brain. *Anatomy Research International*, volume 2011, pp. 1–17.

Papadimitropoulos, A., Mastrogiacomo, M., Peyrin, F., Molinari, E., Komlev, V. S., Rustichelli, F. and Cancedda, R. (2007). Kinetics of in vivo bone deposition by bone marrow stromal cells within a resorbable porous calcium phosphate scaffold: an X-ray computed microtomography study. *Biotechnology and bioengineering*, volume 98, number 1, pp. 271–81.

Parikh, S. (2002). Bone graft substitutes: past, present, future. *Journal of postgraduate medicine*, volume 48, number 2.

Parkinson, I. H., Badiei, a. and Fazzalari, N. L. (2008). Variation in segmentation of bone from micro-CT imaging: implications for quantitative morphometric analysis. *Australasian physical & engineering sciences in medicine / supported by the Australasian College of Physical Scientists in Medicine and the Australasian Association of Physical Sciences in Medicine*, volume 31, number 2, pp. 160–4.

Pavlovic, V. and Metaxas, D. (2004). A graphical model framework for coupling MRFs and deformable models. *Proceedings of the 2004 IEEE Computer Society Conference on Computer Vision and Pattern Recognition, 2004. CVPR 2004.*, volume 2, pp. 739–746.

Perona, P. and Malik, J. (1990). Scale-space and edge detection using anisotropic diffusion. *IEEE Transactions on Pattern Analysis and Machine Intelligence*, volume 12, number 7, pp. 629–639.

Podaropoulos, L., Veis, A. A., Papadimitriou, S., Alexandridis, C. and Kalyvas, D. (2009). Bone Regeneration Using B -Tricalcium Phosphate in a Calcium Sulfate Matrix. *Journal of Oral Implantology*, volume 35, number 1, pp. 28–36.

Polak, S. J., Candido, S., Levengood, S. K. L. and Wagoner Johnson, A. J. (2012). Automated segmentation of micro-CT images of bone formation in calcium phosphate scaffolds. *Computerized Medical Imaging and Graphics*, volume 36, number 1, pp. 54–65.

Polak, S. J., Levengood, S. K. L., Wheeler, M. B., Maki, A. J., Clark, S. G. and Johnson, A. J. W. (2011). Analysis of the roles of microporosity and BMP-2 on multiple measures of bone regeneration and healing in calcium phosphate scaffolds. *Acta biomaterialia*, volume 7, number 4, pp. 1760–71.

Rücker, M., Laschke, M. W., Junker, D., Carvalho, C., Schramm, A., Mülhaupt, R., Gellrich, N.-C. and Menger, M. D. (2006). Angiogenic and inflammatory response to biodegradable scaffolds in dorsal skinfold chambers of mice. *Biomaterials*, volume 27, number 29, pp. 5027–38.

Sarve, H., Lindblad, J. and Johansson, C. B. (2008). Registration of 2D histological images of bone implants with 3D SR(x)CT volumes. In *Lecture Notes in Computer Science (including subseries Lecture Notes in Artificial Intelligence and Lecture Notes in Bioinformatics)*. volume 5358 LNCS. pp. 1071–1080.

Scaglione, S., Giannoni, P., Bianchini, P., Sandri, M., Marotta, R., Firpo, G., Valbusa, U., Tampieri, A., Diaspro, A., Bianco, P. and Quarto, R. (2012). Order versus Disorder: in vivo bone formation within osteoconductive scaffolds. *Scientific Reports*, volume 2, p. 274.

Schwartz, C. E., Martha, J. F., Kowalski, P., Wang, D. a., Bode, R., Li, L. and Kim, D. H. (2009). Prospective evaluation of chronic pain associated with posterior autologous iliac crest bone graft harvest and its effect on postoperative outcome. *Health and quality of life outcomes*, volume 7, p. 49.

Sebastian, T. B., Tek, H., Crisco, J. J. and Kimia, B. B. (2003). Segmentation of carpal bones from CT images using skeletally coupled deformable models. *Medical image analysis*, volume 7, number 1, pp. 21–45.

Sheppard, A. P., Sok, R. M. and Averdunk, H. (2004). Techniques for image enhancement and segmentation of tomographic images of porous materials. *Physica A: Statistical Mechanics and its Applications*, volume 339, number 1-2, pp. 145–151.

Silber, J. S., Anderson, D. G., Daffner, S. D., Brislin, B. T., Leland, J. M., Hilibrand, A. S., Vaccaro, A. R. and Albert, T. J. (2003). Donor site morbidity after anterior iliac crest bone harvest for single-level anterior cervical discectomy and fusion. *Spine*, volume 28, number 2, pp. 134–9.

Song, Y., Treanor, D., Bulpitt, A. and Magee, D. (2013). 3D reconstruction of multiple stained histology images. *Journal of Pathology Informatics*, volume 4, number 2, p. 7.

Spicer, P. P., Kretlow, J. D., Young, S., Jansen, J. a., Kasper, F. K. and Mikos, A. G. (2012). Evaluation of bone regeneration using the rat critical size calvarial defect. *Nature protocols*, volume 7, number 10, pp. 1918–29.

Stalder, A. K., Ilgenstein, B., Chicherova, N., Deyhle, H., Beckmann, F., Müller, B. and Hieber, S. E. (2014). Combined use of micro computed tomography and histology to evaluate the regenerative capacity of bone grafting materials. *International Journal of Materials Research*, volume 105, number 7, pp. 679–691.

Stańczyk, M. and van Rietbergen, B. (2004). Thermal analysis of bone cement polymerisation at the cement-bone interface. *Journal of biomechanics*, volume 37, number 12, pp. 1803–10.

Sung, H.-J., Meredith, C., Johnson, C. and Galis, Z. S. (2004). The effect of scaffold degradation rate on three-dimensional cell growth and angiogenesis. *Biomaterials*, volume 25, number 26, pp. 5735–42.

Theiss, F., Apelt, D., Brand, B., Kutter, A., Zlinszky, K., Bohner, M., Matter, S., Frei, C., Auer, J. a. and von Rechenberg, B. (2005). Biocompatibility and resorption of a brushite calcium phosphate cement. *Biomaterials*, volume 26, number 21, pp. 4383–4394.

van der Pol, U., Mathieu, L., Zeiter, S., Bourban, P.-E., Zambelli, P.-Y., Pearce, S., Bouré, L. and Pioletti, D. (2010). Augmentation of bone defect healing using a new biocomposite scaffold: An in vivo study in sheep. *Acta Biomaterialia*, volume 6, number 9, pp. 3755–3762.

van Lenthe, G. H., Hagenmüller, H., Bohner, M., Hollister, S. J., Meinel, L. and Müller, R. (2007). Nondestructive micro-computed tomography for biological imaging and quantification of scaffold-bone interaction in vivo. *Biomaterials*, volume 28, number 15, pp. 2479–90.

Vandeweghe, S. and De Bruyn, H. (2011). The effect of smoking on early bone remodeling on surface modified Southern Implants®. *Clinical implant dentistry and related research*, volume 13, number 3, pp. 206–14.

von Doernberg, M.-C., von Rechenberg, B., Bohner, M., Grünenfelder, S., van Lenthe, G. H., Müller, R., Gasser, B., Mathys, R., Baroud, G. and Auer, J. (2006). In vivo behavior of calcium phosphate scaffolds with four different pore sizes. *Biomaterials*, volume 27, number 30, pp. 5186–5198.

Waarsing, J. H., Day, J. S. and Weinans, H. (2004). An improved segmentation method for in vivo microCT imaging. *Journal of bone and mineral research : the official journal of the American Society for Bone and Mineral Research*, volume 19, number 10, pp. 1640–50.

Wang, Z., Guo, Z., Bai, H., Li, J., Li, X., Chen, G. and Lu, J. (2013). Clinical evaluation of β-TCP in the treatment of lacunar bone defects: A prospective, randomized controlled study. *Materials Science and Engineering: C*, volume 33, number 4, pp. 1894–1899.

Warren, S. M., Nacamuli, R. K., Song, H. M. and Longaker, M. T. (2004). Tissue-engineered bone using mesenchymal stem cells and a biodegradable scaffold. *The Journal of craniofacial surgery*, volume 15, number 1, pp. 34–7.

Weickert, J. (1998). *Anisotropic diffusion in image processing*. B. G. Teubner, Stuttgart.

Weiner, S. and Wagner, H. D. (1998). THE MATERIAL BONE: Structure-Mechanical Function Relations. *Annual Review of Materials Science*, volume 28, number 1, pp. 271–298.

Will, J., Gerhardt, L.-c. and Boccaccini, A. R. (2011). Bioactive Glass-Based Scaffolds for Bone Tissue Engineering. In *Advances in biochemical engineering/biotechnology*, *volume 126*. pp. 195–226.

Wirjadi, O. (2007). *Survey of 3d image segmentation methods* (Technical Report 123). Fraunhofer ITWM, Kaiserslautern.

Yaszemski, M. J., Payne, R. G., Hayes, W. C., Langer, R. and Mikos, a. G. (1996). Evolution of bone transplantation: molecular, cellular and tissue strategies to engineer human bone. *Biomaterials*, volume 17, number 2, pp. 175–85.

Zerbo, I. R., Bronckers, A. L., de Lange, G. and Burger, E. H. (2005). Localisation of osteogenic and osteoclastic cells in porous β-tricalcium phosphate particles used for human maxillary sinus floor elevation. *Biomaterials*, volume 26, number 12, pp. 1445–1451.

Zhao, E., Xu, H., Wang, L., Kryczek, I., Wu, K., Hu, Y., Wang, G. and Zou, W. (2012). Bone marrow and the control of immunity. *Cellular and Molecular Immunology*, volume 9, number 1, pp. 11–19.

Zorzi, A. (2012). *Bone Grafting*. InTech.